
Doctoral Dissertations

Student Theses and Dissertations

Fall 2019

Paleoenvironment and paleoclimate of NE Pangea in early Permian-linking chemo- and cyclo-stratigraphy, Bogda Mountains, NW China

Xin Zhan

Follow this and additional works at: https://scholarsmine.mst.edu/doctoral_dissertations

 Part of the [Geology Commons](#), and the [Sedimentology Commons](#)

Department: Geosciences and Geological and Petroleum Engineering

Recommended Citation

Zhan, Xin, "Paleoenvironment and paleoclimate of NE Pangea in early Permian-linking chemo- and cyclo-stratigraphy, Bogda Mountains, NW China" (2019). *Doctoral Dissertations*. 2856.
https://scholarsmine.mst.edu/doctoral_dissertations/2856

This thesis is brought to you by Scholars' Mine, a service of the Missouri S&T Library and Learning Resources. This work is protected by U. S. Copyright Law. Unauthorized use including reproduction for redistribution requires the permission of the copyright holder. For more information, please contact scholarsmine@mst.edu.

PALEOENVIRONMENT AND PALEOCLIMATE OF NE PANGEA IN EARLY
PERMIAN– LINKING CHEMO- AND CYCLO-STRATIGRAPHY, BOGDA
MOUNTAINS, NW CHINA

by

XIN ZHAN

A DISSERTATION

Presented to the Faculty of the Graduate School of the
MISSOURI UNIVERSITY OF SCIENCE AND TECHNOLOGY

In Partial Fulfillment of the Requirements for the Degree

DOCTOR OF PHILOSOPHY

in

GEOLOGY AND GEOPHYSICS

2019

Approved by:

Wan Yang, Advisor
Stephen Gao
David Wronkiewicz
Jonathan Obrist-Farner
Mingli Wan
Neil Tabor

© 2019

XIN ZHAN

All Rights Reserved

PUBLICATION DISSERTATION OPTION

This dissertation consists of the following four articles, formatted in the style used by the Missouri University of Science and Technology:

Paper I: Pages 4–54 have been in review by Journal of Asian Earth Sciences

Paper II: Pages 55– 122 have been in review by Geological Society of America

Bulletin

ABSTRACT

The overall objective of this study is to understand physical and chemical responses of Earth Systems to environmental and climatic perturbations of diverse magnitudes and time scales in Bogda Mountains, NE Pangea. Field investigations, petrographic observations, and geochemical analyses have been used to interpret paleoenvironment and paleoclimate in cm-m-scale high-order cycles (HCs: 0.1–100 kyrs), low-order cycles (LCs: 1–10 Myr), and critical events of late Paleozoic ice age (LPIA: 320–260 Myr ago). Four organo-facies are one-to-one correlated with the four lithofacies in the meter-scale HCs, suggesting litho- and organo-facies are genetically linked and fundamentally controlled by environmental changes associated with lake contraction and extension. The coincidence of climatic changes in mid-latitude northeast Pangea and Gondwanan glacial–interglacial in mid Sakmarian–early Kungurian provides clues that glaciation may have exerted a substantial control on climatic changes in mid-latitude Northern Hemisphere.

ACKNOWLEDGMENTS

I would like to express my deepest appreciation to my advisor Dr. Wan Yang for everything. I would like to thank my dissertation committee Drs. Stephen Gao, David Wronkiewicz, Jonathan Obrist Farner, Mingli Wan, and Neil J. Tabor for guidance. I am grateful to Drs. Zewen Liao, Guoying Sheng, Zhao-Wen Zhan, and Yujiao Zhang of State Key Laboratory of Organic Geochemistry (SKLOG), Guangzhou Institute of Geochemistry, Chinese Academy of Sciences, Drs. Francisca Oboh-Ikuenobe, David, Borrok, and Marek Locmelis of Missouri S&T, and Dr. Changqun Cao of Nanjing Institute of Geology and Palaeontology for advices. I appreciate Drs. Hong Lu, Qingtao Wang, Taoli Wang, Yankuan Tian, Jing Liao, Zhongfeng Zhao, and Sutao Gao of SKLOG, Dr. Qiao Feng and Bingkai Wang of Shandong University of Science & Technology, and Drs. Neil J. Tabor and John A. Robbins of Southern Methodist University for GC-MS and GC-IRMS facilities. Thanks to Dr. Jun Wang, Dr. Mingli Wan, Dr. Shengwu Mei, Jianjun Li, Yiran Lv, Ziyue Ju, Jing Duan, Xiaokaiti Nilufar, and Qiming Wang for field help and Dr. Walaa Award, Dr. Robert Haselwander, Dr. Zhixin Li, Dr. Yaoping Wang, Dr. Weisen Liao, Xiaowei Peng, Marissa Spencer, Muneer Abdalla, Wentao Zhang, William Chandonia, Chao Liu, and Congjie Wei for help. This research was partially supported by four student research grants from Geological Society of America, American Association of Petroleum Geologists, and Chinese Academy of Sciences (grant no. SKLOG-201603), and NSF GEOSCI grant (1714749) and NSF China grant (41428201). I am grateful to GGPE department of Missouri S&T for financial support. Sincere gratitude and special thanks go to my parents and my fiancée who provide me with financial support, endless love, and unconditional encouragement.

TABLE OF CONTENTS

	Page
PUBLICATION DISSERTATION OPTION.....	iii
ABSTRACT.....	iv
ACKNOWLEDGMENTS	v
LIST OF ILLUSTRATIONS.....	x
LIST OF TABLES.....	xi
 SECTION	
1. INTRODUCTION	1
 PAPER	
I. ONE-TO-ONE RELATIONSHIP BETWEEN LITHO- AND ORGANO-FACIES IN CYCLIC LACUSTRINE DEPOSITS OF LOWER-PERMIAN LUCAOGOU LOW-ORDER CYCLE, BOGDA MOUNTAINS, NW CHINA	4
ABSTRACT.....	5
1. INTRODUCTION	6
2. GEOLOGICAL SETTINGS.....	7
3. MATERIALS AND METHODS.....	10
4. RESULTS AND ANALYSES.....	14
4.1. LITHOFACIES, DEPOSITIONAL SYSTEMS, AND SEDIMENTARY CYCLES.....	14
4.1.1. Lithofacies 1 - Interlaminated Coarse Siltstone and Very Fine Sandstone.	14
4.1.2. Lithofacies 2 – Siliciclastic Shale.	16

4.1.3. Lithofacies 3 – Wackestone and Dolostone.....	19
4.1.4. Lithofacies 4 – Dolomitic and Calcareous Shales.....	20
4.2. FACIES STACKING AND HIGH-ORDER CYCLES.....	22
4.3. ORGANO-FACIES AND CHARACTERISTICS	23
4.3.1. Organo-Facies 1.	25
4.3.2. Organo-Facies 2.	27
4.3.3. Organo-Facies 3.	28
4.3.4. Organo-Facies 4.	29
4.4. DEPOSITIONAL CONDITIONS AND ORGANIC MATTER MATURITY	30
4.4.1. Proxies Related to Redox Conditions.	30
4.4.2. Proxies Related to Lake Water Salinity.	36
4.4.3. Maturity-Related Biomarkers.	41
5. DISCUSSION	41
5.1. PROXIES DEFINITIVE OF ORGANO-FACIES	41
5.2. CORRELATION BETWEEN LITHO- AND ORGANO-FACIES	44
6. CONCLUSIONS.....	46
ACKNOWLEDGMENTS	47
REFERENCES	47
II. ENHANCED ARIDITY AND SEASONALITY OF MID-LATITUDE NORTHEAST PANGAEA INDUCED BY LATE PALEOZOIC DEGLACIATION	55

ABSTRACT.....	56
1. INTRODUCTION	57
2. GEOLOGICAL SETTINGS	58
3. METHODOLOGY AND DATA.....	62
4. RESULTS	64
4.1. SEDIMENTARY CHARACTERISTICS OF LUCAOGOU AND HONGYANCHI MUDSTONES	64
4.2. ORGANIC GEOCHEMICAL CHARACTERISTICS OF LUCAOGOU AND HONGYANCHI MUDSTONES.....	70
5. DISCUSSION	74
5.1. PRECURSOR ORGANISMS INDICATED BY ORGANIC GEOCHEMICAL EVIDENCES	77
5.2. ORGANIC CARBON ISOTOPE STRATIGRAPHY	77
5.3. CLIMATIC CONDITONS INDICATED BY SEDIMENTARY EVIDENCE.....	80
5.3.1. Redox Condition Indicated by Lamination and Bioturbation.	80
5.3.2. Seasonality Indicated by Couplets and Dropstones.	81
5.4. CLIMATIC CONDITIONS INDICATED BY ORGANIC GEOCHEMICAL EVIDENCES	83
5.4.1. Precipitation Indicated by Biomarkers.....	83
5.4.2. Redox Condition Indicated by Biomarkers.....	85
5.4.3. Thermal Maturity and Use of Biomarkers.	86
5.5. CAUSES OF CLIMATIC CHANGES	87

6. CONCLUSIONS.....	92
ACKNOWLEDGMENTS	94
APPENDIX A. SUPPLEMENTARY MATERIAL	95
REFERENCES	114
SECTION	
2. CONCLUSIONS.....	123
BIBLIOGRAPHY	125
VITA.....	127

LIST OF ILLUSTRATIONS

PAPER I	Page
Figure 1. Geological maps of the study area.....	9
Figure 2. Chrono-, litho, and cyclostratigraphy of Upper Carboniferous-Middle Permian strata in the Tarlong-Taodonggou area.....	10
Figure 3. Outcrop and thin section photographs.....	13
Figure 4. Photomicroscopic photos of four lithofacies.....	17
Figure 5. Correlation between geochemical proxies and lithofacies.	27
Figure 6. Correlation between biomarker proxies and lithofacies with interpreted depositional environments using sedimentary evidence.....	31
Figure 7. Four types of organofacies.	33
Figure 8. Four types of organofacies..	34
Figure 9. Representative mass chromatograms of n-alkanes (TIC), hopanes (m/z=191), and steranes (m/z =217) from four organo-facies.....	37
 PAPER II	
Figure 1. Geological map of the study area..	60
Figure 2. Lithological columns.	61
Figure 3. Correlation of Asselian–Kungurian climate in north hemisphere, equator, and south hemisphere.....	66
Figure 4. Photomicrographs of Lucaogou shale thin-sections in plain light, showing heterogeneous laminae.....	68
Figure 5. Photomicrographs of Hongyanchi siltstone thin-sections in plain light, showing homogeneous sedimentation.....	70
Figure 6. Geochemical proxies diagnostic for types and maturity of organic matter, redox condition, and lakewater salinity in terms of lithology..	76
Figure 7. Conceptual model.....	91

LIST OF TABLES

PAPER I	Page
Table 1. Mineral compositions of four lithofacies and bulk geochemical proxies of four organofacies.....	24
Table 2. Selected geochemical proxies used in this study..	26
Table 3. Values of selected biomarker attributes of four organofacies..	32
Table 4. Major characteristics and interpreted depositional environments and conditions of litho- and organo-facies in this study..	38
PAPER II	
Table 1. Geochemical proxies diagnostic for content, type, and maturity of organic matter in 103 LCG and 47 HYC samples.....	73
Table 2. Geochemical proxies diagnostic for pCO ₂ , redox condition, lake-water salinity in 103 LCG and 47 HYC samples	73

SECTION

1. INTRODUCTION

In this study, field investigations, petrographic observations, and geochemical analyses have been used to interpret paleoenvironment and paleoclimate in cm-m-scale high-order cycles (HCs: 0.1–100 kyrs), low-order cycles (LCs: 1–10 Myr), and critical events of late Paleozoic ice age (LPIA: 320–260 Myr ago), in order to understand physical and chemical responses of Earth Systems to environmental and climatic perturbations of diverse magnitudes and time scales in Bogda Mountains, NE Pangea.

Relationships between litho- and organo-facies within a time-stratigraphic framework at a m-km scale have been well investigated (Curiale et al. 1992; Horsfield et al., 1993; Tyson, 1995; Carroll, 1998; Carroll and Bohacs, 1999; Bohacs et al., 2000; Slatt and Rodriguez, 2012). However, understanding of linkage between litho- and organo-facies at a cm-m scale is limited. In the first part of this study, four meter-scale high-order sedimentary cycles (HCs) in Lucaogou formation in north Tarlong section have been used to investigate litho- and organo-facies. The HCs are composed of interlaminated coarse siltstone and very fine sandstone, siliciclastic shale, wackestone and dolostone, and calcareous and dolomitic shales deposited during lake expansion and contraction. Four organo-facies are defined using bulk geochemical parameters including total organic carbon content (TOC), ratio of hydrogen over carbon (H/C), ratio of carbon over nitrogen (C/N), and organic carbon isotopic composition ($\delta^{13}\text{C}_{\text{org}}$), as well as biomarker proxies including *n*-alkanes, terrestrial over aquatic ratio (TAR), and ratio of 17 α -hopanes over regular C₂₇₋₂₉ steranes. Four organo-facies are one-to-one correlated

with the four lithofacies in the meter-scale HCs, suggesting litho- and organo-facies are linked and fundamentally controlled by sedimentary processes. The organofacies were likely controlled by changes of contribution from higher plants and algae to OM in the deposits as depositional environments change during lake shoreline transgression and regression. The results demonstrate that a holistic approach using lithologic and organic geochemical data is useful in delineating cyclic changes of depositional environments at a cm-m scale, and therefore can be used to understand short-term sedimentary processes in other lacustrine systems.

Paleoclimate of low- and mid-latitude Pangea changed dramatically from humid to arid during the late Paleozoic ice age and has been attributed to the late Paleozoic Gondwanan deglaciations (Cecil, 1990; Parrish, 1993; Miller et al., 1996; Isbell et al., 2003; Montañez et al., 2007, 2016; Poulsen et al., 2007; Fielding et al., 2008; Tabor and Poulsen, 2008; Allen et al., 2011; Montañez and Poulsen, 2013). Relationship between climate of paleo-tropics and glacial cyclicity in Southern Hemisphere has been suggested, however, linkage between climate of mid-latitude North Hemisphere and Gondwanan glacial cyclicity has been largely unresolved. In the second part of this study, we investigate climate of southeastern Kazakhstan mid-latitude northeast Pangea and its linkage with Gondwanan glaciation in early Permian. A humid and seasonal climate is suggested by a mixture of laminated shales and massive mudstones, varves with dropstones, and low gammacerane index, corresponding to late Paleozoic deglaciation over most of Gondwana in early Sakmarian. Enhanced aridity and seasonality are evidenced by dominance of laminated shales, varved deposits, and high gammacerane index, coinciding with interglacial during mid-late Sakmarian. Increased humidity and

seasonal stability are indicated by massive and bioturbated siltstones, absence of varves, and low gammacerane index, accompanying with regional glaciation in eastern Australia during Artinskian–early Kungurian. The coincidence of climatic changes in mid-latitude northeast Pangea and Gondwanan glacial–interglacial in mid Sakmarian–early Kungurian provides clues that glaciation may have exerted a substantial control on climatic changes in mid-latitude Northern Hemisphere.

PAPER

I. ONE-TO-ONE RELATIONSHIP BETWEEN LITHO- AND ORGANO-FACIES IN CYCLIC LACUSTRINE DEPOSITS OF LOWER-PERMIAN LUCAOGOU LOW-ORDER CYCLE, BOGDA MOUNTAINS, NW CHINA

Contributing Authors: Xin Zhan^{a,*}, Wan Yang^{a,*}, Qiao Feng^b

Author Affiliations:

^a Geology and Geophysics Program, Missouri University of Science and Technology,
1400 N. Bishop, Rolla, MO 65409, U.S.A.

^b Shandong Provincial Key Laboratory of Depositional Mineralization and Sedimentary
Minerals, Shandong University of Science and Technology, 579 Qianwangang Road,
Qingdao 266000, China

* Correspondence and requests for materials should be addressed to xz793@mst.edu and
yangwa@mst.edu

ABSTRACT

Relationships between litho- and organo-facies within a time-stratigraphic framework at a m-km scale have been well investigated. However, understanding of linkage between litho- and organo-facies at a cm-m scale is limited. Four meter-scale high-order sedimentary cycles (HCs) in lower-Permian, southern Bogda Mountains, NW China, have been used to investigate litho- and organo-facies. The HCs are composed of interlaminated coarse siltstone and very fine sandstone, siliciclastic shale, wackestone and dolostone, and calcareous and dolomitic shales deposited during lake expansion and contraction. Four organo-facies are defined using bulk geochemical parameters including total organic carbon content (TOC), ratio of hydrogen over carbon (H/C), ratio of carbon over nitrogen (C/N), and organic carbon isotopic composition ($\delta^{13}\text{C}_{\text{org}}$), as well as biomarker proxies including *n*-alkanes, terrestrial over aquatic ratio (TAR), and ratio of 17 α -hopanes over regular C₂₇₋₂₉ steranes. However, redox-, salinity-, and maturity-related proxies cannot define organo-facies in the HCs. Nevertheless, geochemical proxies can provide unique information, in terms of abundance and types of organic matter and lake water chemistry, to improve interpretation of depositional environments of lacustrine deposits interpreted from lithofacies alone at a cm-m scale. Four organo-facies are one-to-one correlated with the four lithofacies in the meter-scale HCs, suggesting litho- and organo-facies are linked. The organofacies were likely controlled by changes of contribution from higher plants and algae to OM in the deposits as depositional environments change during lake shoreline transgression and regression. The results demonstrate that a holistic approach using lithologic and organic geochemical data is useful in delineating cyclic changes of depositional environments at a cm-m scale.

1. INTRODUCTION

Understanding of complex modern and ancient lacustrine sedimentation requires a holistic approach using all available outcrop and laboratory data (e.g., Bradley, 1925; Carroll et al., 1992; Meyer, 1997, 2003). Ancient lacustrine lithofacies may have unique geochemical imprints. This provides the foundation for integrating lithological and organic geochemical data to improve depositional environmental interpretation. Curiale and Lin (1991), for example, identified two distinctive organic facies in Paleogene-Neogene deltaic and lacustrine deposits, west-central North America, on the basis of types of organic matter. Mello et al. (1988) used biomarkers sensitive to lakewater salinity to define organo-facies of Lower Cretaceous source rocks in Brazil in order to differentiate shales deposited in freshwater from saline lakes. Furthermore, the application of organic geochemical proxies in environmental interpretations is effective within a time-stratigraphic framework at a m-km scale (Curiale et al. 1992; Horsfield et al., 1993; Tyson, 1995; Carroll, 1998; Carroll and Bohacs, 1999; Bohacs et al., 2000; Slatt and Rodriguez, 2012). The classification scheme of lake basins in a sequence-stratigraphic-geochemical framework by Carroll and Bohacs (1999, 2001; see also Bohacs et al., 2000) link lithofacies with organic facies during relatively long period of time. However, relationships between litho- and organo-facies during relatively short period of time are not clear because of limited investigations on litho- and organo-facies at a cm-m scale and complexity and variability of depositional sequences in a lake depositional system.

This study investigates the relationship between litho- and organo-facies at a cm-m scale using mixed siliciclastic and carbonate deposits in four meter-scale sedimentary

cycles in lower Permian Lucaogou low-order cycle (LCG LC; Yang et al., 2007, 2010) in NW China. Four types of organofacies are one-to-one correlated with four lacustrine lithofacies in the meter-scale cycles, suggesting that the processes controlling the deposition and characteristics of litho- and organo-facies are genetically linked during short-term lake extension and contraction. This study provides a workable method combining lithological and organic geochemical data to improve interpretation of lacustrine depositional environments at a cm-m scale and associated sedimentary processes in relatively short period of time. A better understanding of changes of litho- and organo-facies at a cm-m scale improves the interpretation of climatic and depositional processes on cyclic deposition. The methodology of this study is useful for delineating highly variable depositional sequence of a lake depositional system and predicting hydrocarbon distribution and characteristics in other partitioned basins.

2. GEOLOGICAL SETTINGS

This study focuses on four m-scale sedimentary cycles in the Lucaogou low-order cycle (LCG LC) in Tarlong-Taodonggou area, at the southern foothills of Bogda Mountains, NW China (Figure 1a). The Bogda Mountains are a giant anticline, contain Devonian to Quaternary sedimentary and igneous rocks, and separate the Turpan-Hami Basin to the south from the Junggar Basin to the northwest (Zhang, 1981; Yang et al., 2010). Uppermost Carboniferous-Lower Triassic fluvial-lacustrine deposits are exposed as folded strata in N, NW, S, and SW Tarlong and Taodonggou sections (Figure 1b; Chen et al., 1985; Liao et al., 1987; XBGMR, 1993; Carroll et al., 1995; Yang et al., 2007,

2010). They were deposited in the Tarlong-Taodonggou half graben (Yang, 2008; Yang et al., 2010; Obrist-Farner and Yang, 2016, 2017). Recent paleotectonic and paleogeographic reconstruction places the Bogda Mountains in southeastern Kazakhstan Plate, NE Pangea (Figure 1c; Scotese, 2014). The paleoclimatic conditions varied from subhumid to semiarid during the deposition of LCG LC, as interpreted on basis of sedimentary evidence by (Yang et al. 2007, 2010).

LCG LC is defined by Yang et al. (2007, 2010) as sedimentary cycle of similar long-term depositional environments and formed under long-term stable tectonic and/or climatic conditions. The age of LCG LC is estimated from middle Sakmarian to mid Artinskian (Figure 2; Yang et al., 2010). The LCG LC is composed of high-order cycles (HCs), which are defined by repetitive environmental shifts (Yang et al., 2010). They reflect changes in environmental conditions and sedimentary processes. Three types of HCs, namely lacustrine deltaic, lakeplain-littoral, and fluctuating profundal mixed siliciclastic and carbonate cycles, occur in LCG LC (Yang et al., 2007, 2010). They are composed of fluvial-lacustrine siliciclastic, carbonate, and paleosol lithofacies and are decimeter to meter thick. The HCs reflect repetitive changes of fluvial and lacustrine environments during lake contraction and expansion and shoreline transgression and regression. The correlation of the thickness and types of HCs between the Tarlong and Taodonggou sections by Yang et al. (2010) suggests that N Tarlong is both the depositional and subsidence center (Yang et al., 2010). The lithofacies associations in HCs suggest that the LCG lake was mainly balance-filled during the formation of lakeplain-littoral and fluctuating profundal cycles and, in some cases, over-filled to form lacustrine deltaic cycles. Finally, the climatic sensitive lithofacies and paleosols indicate

highly variable subhumid to semiarid paleoclimatic conditions during the formation of the LCG LC (Yang et al. 2010).

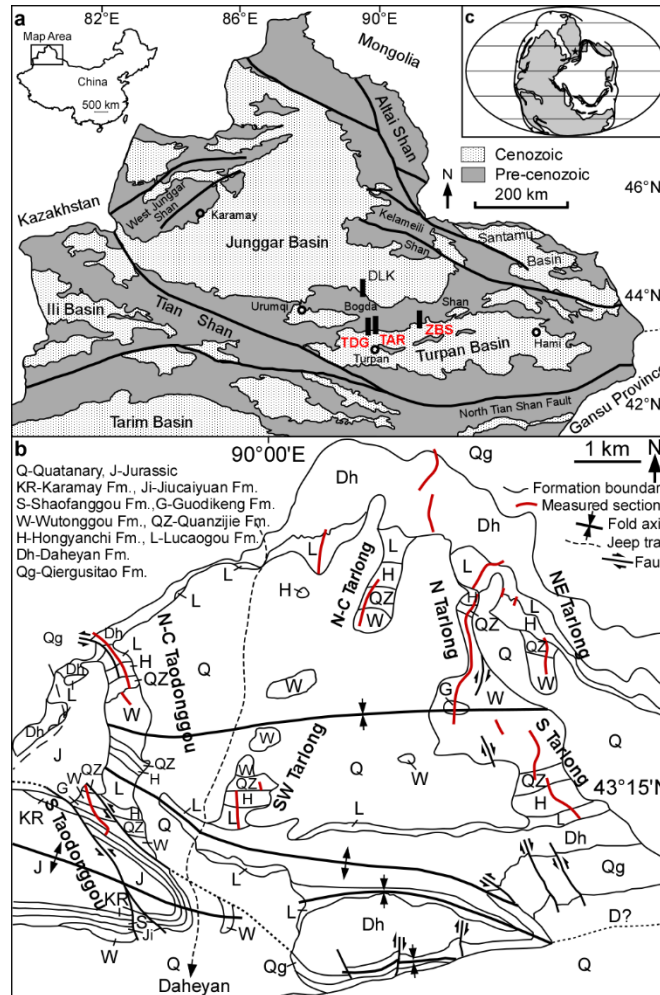


Figure 1. Geological maps of the study area. (a) Geological map of Turpan-Hami Basin, Junggar Basin, Santanghu Basin, Bogda Mountains, and Tianshan in Xinjiang Uygur Autonomous Region, NW China. Black bars show the location of Tarlong (TAR), Taodonggou (TDG), Dalongkou (DLK), and Zhaobishan (ZBS) sections. Modified from Chen et al. (1985), XBGMR (1993), and Yang et al. (2010). (b) Geological map of Tarlong-Taodonggou area. Modified from Yang et al., (2010) and Obrist-Farner and Yang (2016). (c) Paleotectonic and paleogeographic reconstruction of Pangea at early Permian at 290 Ma (Scotese, 2014).

Period	Epoch	Lithostratigraphy (Formation)	Cyclostratigraphy Low-Order Cycles (Yang et al., 2010; Obrist-Farner and Yang 2015)	Revised Cyclostratigraphy (Yang et al., 2010, 2013)	
				New dates	Stages
Triassic	Middle	Karamay	Karamay		247.2 Anisian
	Lower	Shaofanggou	Shaofanggou		251.2 Olenekian
		Jiucaiyuan	Jiucaiyuan		251.902 Induan
		Guodikeng			
Permian	Lopingian	Wutonggou	Wutonggou	253.11 & 253.63 254.22	254.14 Changhsingian
					259.1 Wuchiapingian
	Guadalupian	Quanzijie	Upper Quanzijie Lower Quanzijie	?	265.1 Capitanian
					268.8 Wordian
					272.95 Roadian
	Cisuralian	Hongyanchi	Hongyanchi	281.42	Kungurian
		Lucaogou	Lucaogou		283.5
					290.1 Artinskian
					295.0 Sakmarian
		Daheyan	Upper Daheyan Middle Daheyan Lower Daheyan		298.9 Asselian
Carboniferous Pennsylvanian	Upper	Qiergusitao		301.26 ± 0.05 301.37 ± 0.07	303.7 Gzhelian
				305.50 ± 0.11 306.48 ± 0.32	307.0 Kasimovian

Figure 2. Chrono-, litho, and cyclostratigraphy of Upper Carboniferous-middle Permian strata in the Tarlong-Taodonggou area. Hachured areas indicate missing strata; wavy lines are major unconformities; and dashed lines are disconformities; Absolute ages at stage boundaries are from Cohen et al. (2018). Modified from Yang et al. (2010) and Obrist-Farner and Yang (2016).

3. MATERIALS AND METHODS

Field, petrographic, and geochemical studies have been carried out to identify litho- and organo-facies. The composition, sedimentary texture and structure, fossils, and stratal geometry and boundary relationship of component lithofacies in four HCs were documented in the field, hand samples, and thin-sections to identify lithofacies and interpret their depositional environments. 15 samples in four fluctuating profundal mixed siliciclastic and carbonate HCs in N Tarlong section were collected. Care was taken to

select samples that are at least 30 cm beneath surface and have no signs of surface weathering.

Bulk geochemical and biomarker analyses have been performed in State Key Laboratory of Organic Geochemistry, Guangzhou Institute of Geochemistry, Chinese Academy of Sciences in Guangzhou, China. The results are used to identify organofacies. Samples were first decontaminated through sonication in deionized water and then oven dried at 40 °C before all the geochemical analyses. The total organic carbon (TOC) and total sulfur (TS) of the 100-mesh (<0.15 mm) powdered sample were obtained with a Leco SC-632 carbon sulfur analyzer following removal of carbonates by HCl acid digestion.

Calcite equivalent content (CaCO_3 %) has been measured from inorganic carbon concentration (CO_3^{2-}) for duplicated samples under the assumption that all CO_3^{2-} is present as CaCO_3 . CaCO_3 (%) was calculated using a carbonate content analyzer (Model: GMY-3). Volume of CO_2 was measured after 200 mg of samples have completely reacted with excessive amounts of hydrochloric acid (10 volume %). CaCO_3 (%) value of each sample was evaluated by comparing the CO_2 values with that released from completed reaction of pure calcite and the acid. We recognize the inherent errors in this assumption (i.e. CO_3^{2-} is also present as $\text{CaMg}(\text{CO}_3)_2$, and carbonates other than CaCO_3 are present). Nevertheless, the estimated CaCO_3 shows a reasonable trend of carbonate minerals in all samples.

Mineral composition analysis was conducted using an X-ray diffractometer (Model: Olympus Innova-X BTX-II), equipped with a Co radiation source and operated at 31 kV and 0.4 mA. The exposure time was 70 min with an exposure rate of 3

times/min. Scanning measurements of powdered samples were performed in the range of 3° – 55° (2θ), with a scanning speed of 0.02° (2θ)/min. Results of relative mineral compositions were estimated semiquantitatively using peak area of major minerals and normalized to a total of 100%.

Kerogen extraction was done first by pretreating ~10 g of samples with hydrochloric and hydrofluoric acid to remove all carbonate and siliciclastic components, respectively, following procedures of Durand and Nicaise (1980). Stable organic isotopic composition ($\delta^{13}\text{C}_{\text{org}}$) was measured using combustion system with a coupled elemental analyzer and isotope ratio mass spectrometer (Model: ThermoFinnigan Delta XL Plus GC-IRMS). 20–80 μg of kerogen were added to a stannum boat and combusted at 1800°C under helium carrier gas, following Craig (1953). Isotope ratios were determined based on delta notation (‰) relative to the Vienna Pee Dee Belemnite (V-PDB) standard after Craig (1957). Precision of duplicated samples is $\pm 0.08\text{‰}$ for $\delta^{13}\text{C}_{\text{org}}$. Because isotopic measurements were conducted and expressed relative to the same working standard, the accuracy is reasonably assured.

Extraction, separation, and gas chromatography-mass spectrometry (GC-MS) analysis of saturated fraction of dissolved organic matter in powdered samples are performed following Lu et al. (2018). Identification of individual compounds was achieved by comparing mass spectra and fragmentation patterns with literature and library data, authentic standards, and published mass spectra (Peters et al., 2005).

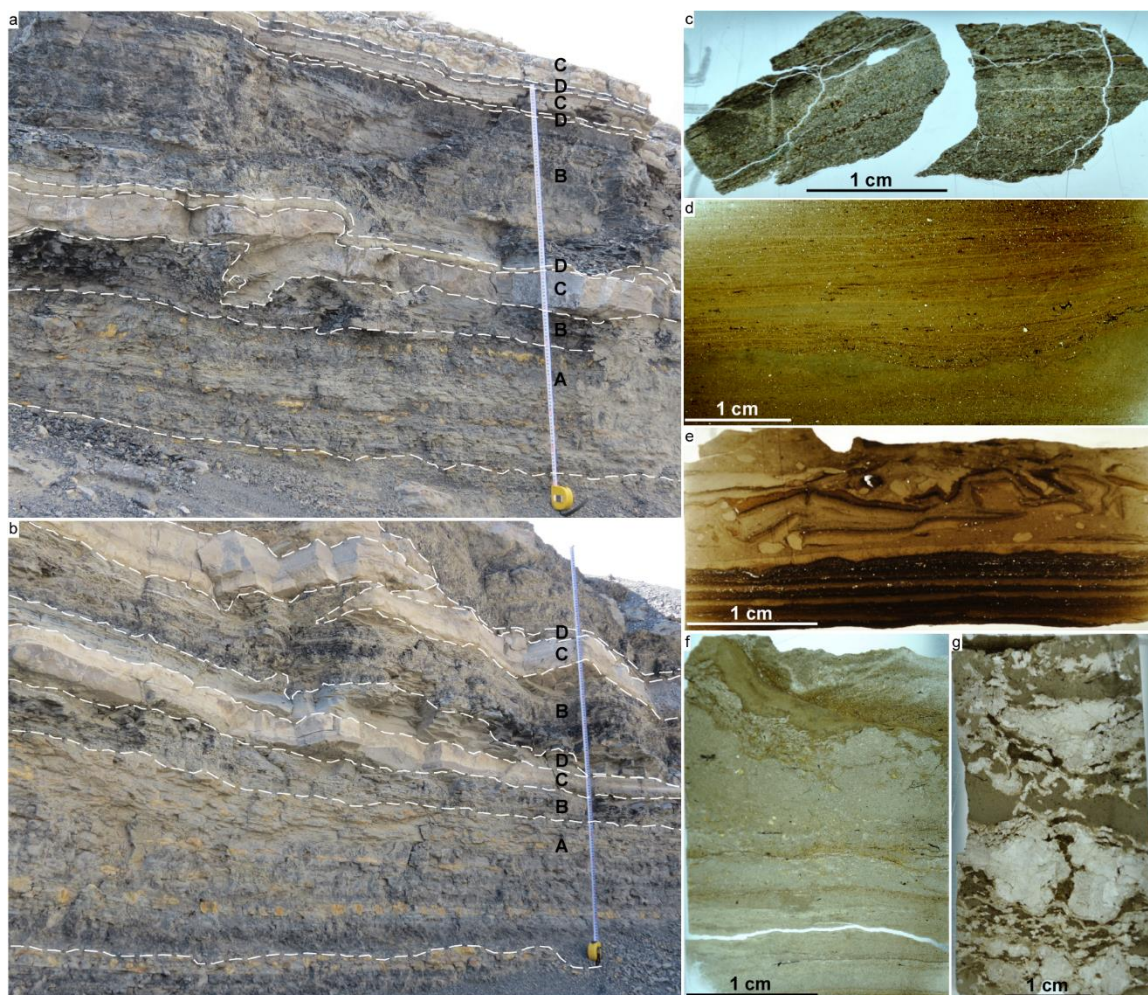


Figure 3. Outcrop and thin section photographs. (a–b) Outcrop photographs of four high-order cycles (HCs) of Lucaogou low-order cycle (LCG LC), each HC is around one meter thick. Component lithofacies are A: Interbedded siltstone and very fine sandstone; B: Black shale; C: Wackestone and dolostone; D: Dolomitic and calcareous shales. (c) Photomicrograph of interbedded siliciclastic siltstone and very fine sandstone. It is dolomite-cemented and massive or weak laminated, and contains abundant higher terrigenous plant remains. It is interpreted as lakeplain deposits. (d) Photomicrograph of siliciclastic shale. It is organic-rich, very well parallel and algal laminated. An erosional surface is in lower part. It is interpreted as profundal deposits. (e) Photomicrography of dolomitic and calcareous shale. The lower part is well laminated, dolomitic, and organic-rich. It contains abundant plant remains and ostracods. It is interpreted as deposits in shallow littoral environments. The upper part has desiccated mud cracks, burrows, undulating laminations, and micro faults mixed with sand-size mud clasts. It is interpreted as formed in dehydration environments. (f) Photomicrography of wackestone. The lower part is well laminated or massive and the upper part is stromatolitic/cryptalgal laminated in thin and wavy beds. It is interpreted as deposits in littoral environments (g) Photomicrography of dolostone. It is algal laminated and interpreted as deposits in littoral environments.

4. RESULTS AND ANALYSES

Four types of lithofacies, including interlaminated coarse siltstone and very fine sandstone, siliciclastic shale, dolomitic and calcareous shales, and wackestone and dolostone, have been identified in four high-order cycles (HCs; Figure 3a, b). They have distinct mineral composition, sedimentary texture and structure, fossil, and/or stratal geometry (Figure 3a, b; Table 1). Interpreted depositional environments show systematic stratigraphic trends, which are used to define high-order lake expansion-contraction cycles.

4.1. LITHOFACIES, DEPOSITIONAL SYSTEMS, AND SEDIMENTARY CYCLES

4.1.1. Lithofacies 1 - Interlaminated Coarse Siltstone and Very Fine

Sandstone. Coarse siltstone and very fine sandstone are commonly interbedded and interlaminated. Sandstones are greenish gray to blackish gray and occur in 2–20 cm thick beds. The sandstone is classified as arkosic arenite. The framework grains are mainly very fine sand-sized, ranging from medium silt to coarse sand. The fine-sand grains are mainly quartz and feldspar, whereas scattered medium- and coarse-sand grains are mainly mud clasts. The silt-size grains are mainly quartz and feldspar with minor lithics, magnetite, and micas. Matrix is ~5% and composed mainly of clay minerals. Cement is composed mainly of calcite and dolomite. Quartz is mainly monocrystalline. Feldspar is mainly albite and K-feldspar, most of which has been partially altered to sericite. The compositions of lithic grains are unidentified due to their small size. The mineral compositions are confirmed by XRD results of 30% quartz, 24–29% feldspar, 13%

kaolinite, 9% calcite, and 4% dolomite (Table 1). The framework grains in sandstones are poorly sorted and angular to subrounded. Parallel and wavy laminations are continuous (Figure 3c). Mud clasts are sand size, angular to sub-angular, and well imbricated. Abundant plant remains and woody debris in coarse-silt to coarse-sand size are commonly parallel to bedding plane. Phytoclasts are commonly opaque, angular lath-shaped, with sharp distinct edges, but their internal structure is commonly obliterated, resulting in a massive and invisible biostructure. Amorphous OM is reddish brown to black, diffuse-edged, irregular-shaped, and structureless, and mainly present in the mud clasts. Finally, the matrix content is less than.

Coarse siltstone is brownish gray to reddish brown and in beds 20–40 cm thick. It contains sandy and gravel grains in the lower part. Silt grains are mainly quartz and feldspar, with minor calcite and dolomite. Clay size grains are about 20%. Sand to granule-size grains are paleosol clasts. Silts are equant, sub-angular to rounded and moderately sorted, whereas sands and granules are sub-angular to sub-rounded and poorly sorted. Abundant phytoclasts are mm-cm in size, well preserved, and randomly distributed. They are opaque and elongate and they have angular and sharp edges and internal scalariform pitting or cross-field pitting (Figure 4a). Reddish orange spores are randomly scattered and commonly occur with phytoclasts (Figure 4a). Some fine-sand-sized clasts have irregular shape and contain various tubes inside (Figure 4b). These tubes have siliciclastic walls and they are filled with organic matter. They are likely worm tubes.

The sandstones and siltstones are interbedded and interlaminated and commonly overlie muddy paleosols of underlying cycle (see below). They form an overall fining-

and thinning-upward trend. The facies have a sharp to slightly erosional base and a gradational to sharp top. The mud clasts in sandstones are interpreted as paleosol rip-up clasts. Possible worm tubes suggest oxic lake water condition. The lithofacies is interpreted as low-medium energy lake-plain to littoral deposits during shoreline transgression (see also Yang et al., 2010).

4.1.2. Lithofacies 2 – Siliciclastic Shale. Siliciclastic shale is blackish gray to black, and occurs as 10–40 cm thick beds. It is composed dominantly of detrital grains and organic matter (OM). Detrital grains are mainly in clay to fine-medium-silt size, with rare coarse-silt to granule size. They are mainly quartz and feldspar with sparse lithic fragments, calcite, and dolomite and sparse clay minerals. This is also supported by 30–52% quartz, 16–20% feldspar, 4–22% dolomite, 4–15% calcite, and 12–16% kaolinite from XRD results (Table 1). Rare mud clasts range from coarse silt to fine granule size and commonly contain amorphous OM. Siliciclastic shale is well parallel laminated with dominantly mm-to-sub-mm laminae (Figure 3d). The laminae are generally continuous and in some cases, wavy and climbing rippled. The bedding plane is sharp to gradational and, in places, rarely erosional. This lithofacies is organic-rich, and variably calcareous or dolomitic (Table 1). It contains common plant remains, amorphous OM, intact ostracod, sparse fish scales, and other skeletal fragments. Phytoclasts are opaque, angular, elongate, and contain internal lath-shaped structure. They are randomly distributed but locally concentrated on bedding plane. Amorphous OM grains are reddish brown to black, diffuse-edged, and structureless (Figure 4c). Ostracod shells consist of single and articulated valves, and are highly compressed and parallel to bedding (Figure 4d).

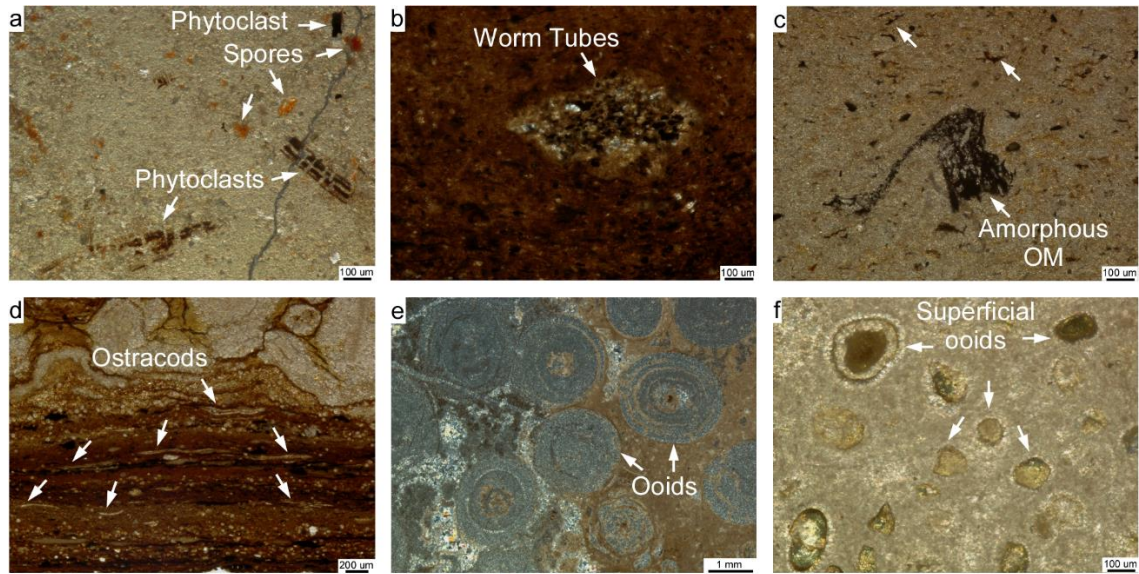


Figure 4. Photomicrographs of four lithofacies. (a) Phytoclasts and spores in Lithofacies 1 in PL; the opaque biostructured phytoclasts break up into lath-shaped particles by splitting along the grain, noting splintery nature and brittle character; the angular outline, elongated shape, and structural grains are clear evidence of phytoclast structure; the orange fragments may be spores of uncertain affinity. (b) Worm tubes in Lithofacies 1 in PL; a transverse section of a bundle of worm tubes in a single grain, with organic matter filling inside the tubes. (c) Well preserved amorphous organic matter in Lithofacies 2 in PL. (d) Highly-compressed ostracods in Lithofacies 2 in PL; they consist of single and a pair of ostracode valves with carapace interior, aligned parallel to the organic-rich laminae. (e) Concentrically coated ooids in Lithofacies 3 in PL, with peloidal nucleus and multiple concentric cortices. (f) Superficial ooids in Lithofacies 3 in PL with only one thin cortical coat around detrital nuclei. The coat is isopachous calcite cement with radial structure in the cortex of the superficial ooids. Some other detrital grains are not coated. (g) Cyanobacteria in Lithofacies 3; noting small ‘bunches’ in irregularly shaped clumps in transverse section are well preserved. (h) Algae in Lithofacies 4 in PL; noting the sand-sized grains are rounded, with smooth and organic wall. (i) Phytoclasts and spores in Lithofacies 4 in PL; clear scalariform pitting in the opaque biostructured phytoclasts shows that the particle was derived from tracheid tissue, and the fine microstructure suggests a possible charcoal origin. (j) Ostracods in Lithofacies 4 in PL; A pair fish-hook-like terminations of a single ostracode valve, these terminations are distinctive features of identification of ostracode remains, in combination with carapace size, structure, and wall morphology. (k) Two grains containing worm tubes in Lithofacies 4 in PL; the grains rupture underlying sub-mm laminae and are covered conformably by laminae; worm tubes in bunches have well preserved wall structure. (l) A dropped grain containing chambers filled with organic matter in Lithofacies 4 in PL; the grain ruptures the underlying interlaminated calcareous and dolomitic laminae and are covered conformably by the laminae. (m–o) SEM-EDS results of the grain and laminae in (l), showing distribution of carbon, calcium, and magnesium, respectively, and confirming presence of organic matter in the grain and interlaminated calcareous and dolomitic laminae.

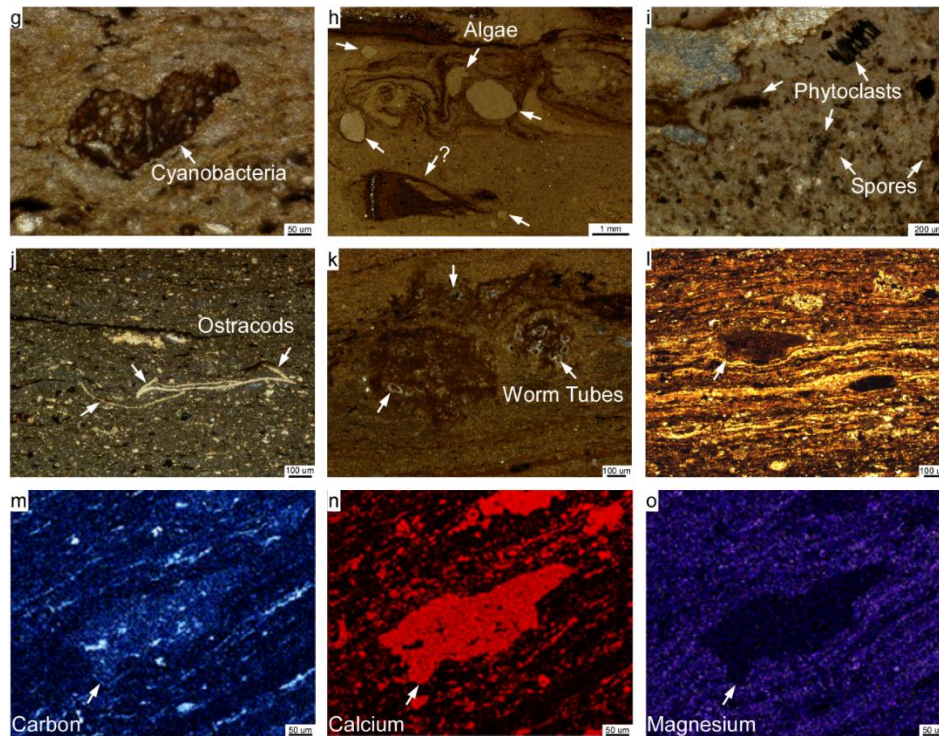


Figure 4. Photomicrographs of four lithofacies. (a) Phytoclasts and spores in Lithofacies 1 in PL; the opaque biostructured phytoclasts break up into lath-shaped particles by splitting along the grain, noting splintery nature and brittle character; the angular outline, elongated shape, and structural grains are clear evidence of phytoclast structure; the orange fragments may be spores of uncertain affinity. (b) Worm tubes in Lithofacies 1 in PL; a transverse section of a bundle of worm tubes in a single grain, with organic matter filling inside the tubes. (c) Well preserved amorphous organic matter in Lithofacies 2 in PL. (d) Highly-compressed ostracods in Lithofacies 2 in PL; they consist of single and a pair of ostracode valves with carapace interior, aligned parallel to the organic-rich laminae. (e) Concentrically coated ooids in Lithofacies 3 in PL, with peloidal nucleus and multiple concentric cortices. (f) Superficial ooids in Lithofacies 3 in PL with only one thin cortical coat around detrital nuclei. The coat is isopachous calcite cement with radial structure in the cortex of the superficial ooids. Some other detrital grains are not coated. (g) Cyanobacteria in Lithofacies 3; noting small ‘bunches’ in irregularly shaped clumps in transverse section are well preserved. (h) Algae in Lithofacies 4 in PL; noting the sand-sized grains are rounded, with smooth and organic wall. (i) Phytoclasts and spores in Lithofacies 4 in PL; clear scalariform pitting in the opaque biostructured phytoclasts shows that the particle was derived from tracheid tissue, and the fine microstructure suggests a possible charcoal origin. (j) Ostracods in Lithofacies 4 in PL; A pair fish-hook-like terminations of a single ostracode valve, these terminations are distinctive features of identification of ostracode remains, in combination with carapace size, structure, and wall morphology. (k) Two grains containing worm tubes in Lithofacies 4 in PL; the grains rupture underlying sub-mm laminae and are covered conformably by laminae; worm tubes in bunches have well preserved wall structure. (l) A dropped grain containing chambers filled with organic matter in Lithofacies 4 in PL; the grain ruptures the underlying interlaminated calcareous and dolomitic laminae and are covered conformably by the laminae. (m–o) SEM-EDS results of the grain and laminae in (l), showing distribution of carbon, calcium, and magnesium, respectively, and confirming presence of organic matter in the grain and interlaminated calcareous and dolomitic laminae. (cont.)

Black shales commonly overlie interbedded and interlaminated siltstone and sandstone of Lithofacies 1, and underlie limestone of Lithofacies 3 (see below) with gradational contacts. The mm-to-sub-mm laminations and absence of bioturbation suggest a low-energy, relatively anoxic, profundal environment. The stratigraphic relationship with sub- and superjacent facies suggest that they are probably maximum transgressive deposits (Yang et al., 2010).

4.1.3. Lithofacies 3 – Wackestone and Dolostone. Wackestone is gray to dark gray, well bedded and laterally consistent, in beds 10-40 cm thick. It contains 10-20% allochems and 25-45% detrital quartz, 0-15% feldspar, and lithic grains in 33-72% calcitic and 0-28% dolomite matrix and cement (Table 1). Detrital grains are mainly medium-coarse silt-sized and angular to sub-angular. Allochems include skeletal fragments, ooids, superficial ooids, pellets, and intraclasts. Skeletal fragments are mainly bivalves, gastropods, ostracods, fish bones, fish scales, and some unidentified skeleton grains. Well-preserved bivalves and fish skeletons are locally abundant. Gastropods and ostracods are well preserved and range from medium to coarse silt in size and coarse silt to medium sand in size, respectively. Ooids range from coarse silt to coarse sand in size and have peloidal nuclei and multiple radial and concentric cortices (Figure 4e). Superficial ooids are mainly coarse silt to very fine sand-sized, with a thin cortex on irregular and angular lithic nuclei (Figure 4f). Intraclasts and pellets are commonly blackened, micritic, and in silt to pebble size. Intraclasts are mostly micritic; some are grapestones. Possible cyanobacteria have various well preserved small bunches in irregularly shaped clumps (Figure 4g). The lower part of wackestone is parallel laminated and rich in siliciclastics and organics; the upper part is algal laminated and micritic

(Figure 3f). Common amorphous OM occurs as reddish brown stains or asphalt along algal laminations. Rare lumps containing apparent cell structures are present in algal laminae. A few opaque phytoclasts are fine to very coarse sand-size. The coarse grains commonly have rectangular cell outlines, suggesting that the clasts were derived from woody tissue.

Dolostones are yellowish gray to dark brown and dense, and occur as 1-20 cm thick beds. They react slowly with dilute hydrochloric acid. They are composed mainly of dolomitic mud or microspars and siliciclastic mud of quartz (Table 1). Dolostone are parallel or algal laminated, thrombotic, or, in a few cases, massive (Figure 3g). Cone-in-cone structures are well-developed in a few highly-recrystallized dolostone. Skeletal grains and organic matter in dolostone similar to those in wackestone.

Wackestones commonly overlie black shale. High abundance of skeletal fragments indicate a quiet and oxic littoral to profundal environment. Dolostones, which commonly interbedded and interlaminated with dolomitic/calcareous shales (see below), overlie wackestones or black shale. They were interpreted as littoral deposits in quiet, shallow, and saline lake water during lake contraction (Yang et al., 2010).

4.1.4. Lithofacies 4 – Dolomitic and Calcareous Shales. Dolomitic and calcareous shales are yellowish brown, gray to dark gray, and black. They are mainly composed of quartz, feldspar, clay minerals, dolomite or calcite, and a few lithic fragments. This is also supported by 24-48% quartz, 19-22% feldspar, 14-27% dolomite, 4-19% calcite, and 11-12% kaolinite from XRD results of 15 samples (Table 1) and presence of calcium- and magnesium-rich laminae from SEM-EDS results (Figure 4l-o). Quartz and feldspar dominate and are in fine-medium silt size. The content of dolomite

and calcite varies. Dolomite is silty and euhedral; and calcite is microcrystalline. Rare elongate gypsum crystals and sand-size calcified nodules are present in some other similar samples (Yang et al., 2007, 2010).

Dolomitic and calcareous shales are interlaminated at a sub-mm (Figure 4l–o) to mm scale (Figure 3e), to form beds 5–15 cm thick. The laminae are dominantly parallel, some wrinkly, and rarely lenticular. The parallel laminae are composed of couplets of organic-rich and dolomitic/calcareous laminae. They are overlain by a mixed layer characterized by wrinkly laminations, micro faults, burrows, mud cracks, and sand-size mud clasts. The contact is erosional. Sparse mud clasts range from coarse silt to coarse sand size, sub-angular to rounded. A few of them distorted underlying laminae and are covered by continuous laminae (Figure 4l). Amorphous OM is abundant; phytoclasts and ostracods are common and concentrated along beddings, whereas fish scales and skeletons are sparsely to commonly scattered. Amorphous OM is reddish brown to black, irregular-shaped, and structureless. It is locally concentrated in parallel laminae, whereas it is highly abundant and randomly distributed in the overlain wrinkly laminae. Some of the amorphous OM is in granule size (Figure 4h). Some of the sand-sized grains are rounded, with smooth and organic wall, and thus likely algae (Figure 4h). Phytoclasts are opaque, elongate, angular, and locally concentrated in parallel laminae. They have sharp edges and internal scalariform pitting or cross-field pitting (Figure 4i). Reddish orange spores are randomly scattered and commonly occur with phytoclasts (Figure 4i). Common ostracode has a pair fish-hook-like terminations and distinctive wall morphology and structure (Figure 4j). Some fine-sand-sized clasts have irregular shape

and contain siliciclastic tubes inside, with organic matter filling in the tubes, and thus likely worm tubes (Figure 4k).

This lithofacies is interpreted as low-energy and evaporative deposits that mixed detrital grains and dolomite and calcite, suggesting intermittent clastic deposition and chemical precipitation in subaqueous or marginal mud flat. Presence of gypsum suggests relatively high salinity in lake water. In addition, mud cracks, micro faults, and wrinkly laminae were probably caused by dehydration and fracture of salt-indurated crust in arid conditions. The couplets of organic-rich and dolomitic/calcareous laminae suggest highly variable periods of deposition, and possibly seasonal climate (Yang et al., 2007, 2010). Organic-rich laminae may have been formed as increased mud influx during wet periods, whereas dolomitic and calcareous laminae may have been formed as reduced mud influx and increased evaporation during dry periods. Dolomitic and calcareous shales commonly overlie wackestone with a gradual contact, and commonly overlain by the transgressive siltstone and sandstone with sharp contact, suggesting they were likely deposited in littoral environments during late regression (Yang et al., 2010).

4.2. FACIES STACKING AND HIGH-ORDER CYCLES

The stacking of the four lithofacies shows systematic changes of lacustrine environments, which define lake expansion and contraction cycles similar to fluctuating profundal mixed carbonate-siliciclastic HCs defined by Yang et al. (2007, 2010). The four HCs are 1 m thick (Figures 5a, b, 6a, b). The basal part of a HC contains Lithofacies 1, which overlies paleosols with a sharp to slightly erosional base and is interpreted as transgressive lake plain to littoral deposits. It underlies Lithofacies 2 of black shales

deposited in sublittoral to profundal environments. The stacking pattern suggests a deepening-upward trend during lake expansion. Upsection, the black shales are overlain by Lithofacies 3 of wackestone and dolostone with a sharp contact, which, in turn, is overlain by Lithofacies 4 of dolomitic and calcareous shales. This succession is interpreted as a shallowing-upward environmental trend during lake contraction. However, paleosols are not present on top of Lithofacies in the four HCs, although they cap some other HCs in the Lucaogou low-order cycle (Yang et al., 2010). The systematic environmental changes upsection in the HCs indicate lake shoreline transgression and regression and expansion and contraction, which were likely caused by lake level rise and fall, respectively. Finally, Yang et al. (2010) speculated that the lake level fluctuations may have been caused by intra-cyclic climatic changes from humid-subhumid during lake expansion to semi-arid to arid during lake contraction.

4.3. ORGANO-FACIES AND CHARACTERISTICS

An organo-facies is subdivision of a rock body which can be distinguished from adjacent subdivisions through organic geochemical characteristics of the sediments, without considering the aspects of the inorganic fraction (Jones and Damaison, 1982). Four distinctive organo-facies (OFs) have been identified in four HCs on the basis of specific bulk geochemical parameters related to abundance and geochemical composition of organic matter and specific biomarker proxies related to types of organic matter. These bulk geochemical parameters includes total organic carbon content (TOC), atomic ratio of hydrogen over carbon (H/C) and carbon over nitrogen (C/N), and organic carbon isotopic composition ($\delta^{13}\text{C}_{\text{org}}$; Tables 1, 2; Figure 7c–f). These biomarker proxies include

proposition of short-chain, mid-chain, and long-chain *n*-alkanes, terrestrial over aquatic ratio (TAR), and ratio of 17 α -hopanes over regular C₂₇₋₂₉ steranes (hopane/sterane., Tables 2 and 3; Figure 8a, b, d).

Table 1. Mineral compositions of four lithofacies and bulk geochemical proxies of four organofacies

Sample No.	Quartz (%) ^a	Feldspar (%) ^b	Calcite (%) ^c	Dolomite (%) ^d	Kaolinite (%) ^e	CaCO ₃ (%) ^f	TOC (wt.%) ^g	TS (wt.%) ^h	H/C ⁱ	C/N ^j	$\delta^{13}\text{C}_{\text{org}}$ (‰) ^k
Lithofacies 1						Organofacies 1					
XZ15-1	29.0	23.7	8.3	3.7	12.9	7.9	0.34	0.259	1.74	25.9	-21.8
XZ15-9	30.0	28.9	9.2	3.9	14.1	14.5	0.25	0.270	1.65	26.3	-22.5
Lithofacies 2						Organofacies 2					
XZ15-6	41.7	15.7	14.6	4.3	12.1	15.1	3.12	0.004	1.87	46.3	-26.1
XZ15-5	41.1	15.9	8.3	5.3	15.8	13.3	2.92	0.000	1.66	43.3	-24.8
XZ15-2	52.1	17.2	15.0	4.0	0	22.4	3.45	0.000	1.63	46.5	-24.1
XZ15-13	30.6	19.9	4.3	22.1	11.7	37.3	4.77	0.015	1.94	40.0	-25.3
XZ15-10	41.8	16.8	7.1	8.6	14.7	16.8	2.81	0.000	1.86	47.8	-26.2
Lithofacies 3						Organofacies 3					
XZ15-7	24.8	14.4	4.2	37.0	10.6	72.0	1.31	0.025	1.76	42.5	-25.7
XZ15-3	27.7	0	72.3	0	0	97.0	0.74	0.000	1.67	39.5	-25.5
XZ15-15	45.5	0	7.8	36.4	0	64.5	3.01	0.019	1.91	48.7	-27.2
XZ15-14	24.1	0	33.1	27.7	0	96.3	0.89	0.009	1.91	42.2	-26.1
XZ15-11	31.8	0	44.6	7.5	0	83.3	1.49	0.000	1.61	42.7	-25.1
Lithofacies 4						Organofacies 4					
XZ15-8	47.5	0	3.7	26.6	11.2	16.3	6.49	0.010	2.02	36.4	-28.6
XZ15-4	34.6	22.2	3.8	26.9	0	18.7	6.11	0.005	1.89	49.9	-27.3
XZ15-12	24.2	19.3	19.1	13.7	12.4	51.3	5.85	0.019	2.14	46.6	-29.6

^a Quartz (%) is calculated as content of quartz over all minerals; ^b Feldspar (%) is calculated as the sum of potassium and sodium feldspar over all minerals; ^c Calcite (%) is calculated as content of calcite over all minerals; ^d Dolomite (%) is calculated as content of dolomite over all minerals; ^e Kaolinite (%) is calculated as content of kaolinite over all minerals; ^f CaCO₃ (%) is measured through comparing CO₂ released from completed reaction of each sample with hydrochloric acid and CO₂ generated from completed reaction of pure calcite with the acid; ^g Total organic carbon content; ^h Total sulfur content; ⁱ Atomic hydrogen/carbon ratio; ^j Atomic carbon/nitrogen ratio; ^k Organic carbon isotope ratio, determined based on delta notation (‰) relative to the Vienna Pee Dee Belemnite (V-PDB) standard.

4.3.1. Organo-Facies (OF) 1. This facies is characterized by an extremely low TOC content of 0.2–0.3 wt.%, low H/C ratio of 1.65 to 1.74, low C/N ratio of 25.9–26.3, and high $\delta^{13}\text{C}_{\text{org}}$ value of -22.5 to -21.8 ‰ (Table 1; Figure 7c–f). This facies is also marked by *n*-alkanes of long-chain (C_{26-34}) \geq mid-chain (C_{20-25}) $>$ short-chain (C_{12-19}), a high TAR of 0.6–2.5, and a very low hopane/sterane ratio of 1.9–2.4 (Table 3; Figure 8a, b, d).

Organic matter (OM) in OF 1 may have been produced by higher plants with low primary productivity. Low TOC was likely caused by low primary productivity and poor preservation of OM in the lake (Meyers, 1997; 2003). OF 1 is rich in ^{13}C , suggesting weak fractionation of ^{12}C from ^{13}C in photosynthesis, as a result of low bioproductivity in the lake. This is supported by a strong correlation between TOC and $\delta^{13}\text{C}_{\text{org}}$ values (Figure 7e). In addition, OM in OF 1 is mainly Type III kerogen, as indicated by low H/C ratio and low C/N ratio (Tissot and Welte 1984; Meyers et al., 1997, 2003). Dominance of long-chain *n*-alkanes and high TAR suggest OM of OF 1 was mainly originated from higher terrestrial plants, with a few from aquatic macrophytes and algae (Eglinton and Hamilton, 1967; Rieley et al., 1991; Meyers and Ishiwatari, 1993; Bush and McInerney, 2013). The interpretation is also supported by woody materials observed under stero- and polarizing microscope. The Low hopane/sterane ratio of OF 1 indicate minor input of bacteria to OM in OF1, because hopanes are typically derived from prokaryotes while steranes are mainly originated from eukaryotes (Ourisson et al., 1979; Rohmer et al., 1984; Volkman, 2003, 2005).

Table 2. Selected geochemical proxies used in this study

Geochemical proxies	Geochemical proxy descriptions	References
Total organic carbon (TOC)*	Amount of residual organic matter in sedimentary rocks	Trask, 1939; Tissot and Welte, 1984; Meyers, 2003
Hydrogen/carbon ratio (H/C)*	Types of kerogen	Tissot and Welte 1984
Carbon/nitrogen ratio (C/N)*	Proportions of algal and land-plant organic matter	Meyers, 1997, 2003
Total sulfur content (TS)	Sulfate-reducing bacteria under anaerobic conditions or formation of pyrite	Casagrande et al., 1979; Casagrande and Ng 1979
Stable organic carbon isotope ($\delta^{13}\text{C}_{\text{org}}$)*	Origins of organic matter and atmospheric pCO_2	Tissot and Welte 1984; Meyers, 1997
Carbon preference index (CPI)	Maturity and sources of organic matter	Bray and Evans, 1961
Odd even preference (OEP)	Maturity and sources of organic matter	Scalan and Smith, 1970
Long chain n-alkanes ($\text{C}_{25}\text{-C}_{35}$)*	Contributions of higher terrestrial plant waxes	Eglinton and Hamilton, 1967; Rieley et al., 1991; Bush and McInerney, 2013
Intermediate chain n-alkanes ($\text{C}_{20}\text{-C}_{24}$)*	Contributions from aquatic macrophytes	Ficken et al., 2000; Sachsenhofer et al., 2006; Bush and McInerney, 2013
Long chain n-alkanes ($\text{C}_{12}\text{-C}_{19}$)*	Contribution of algae and microorganisms	Cranwell et al., 1987; Bush and McInerney, 2013
Terrestrial/aquatic ratio (TAR)*	Ratio between the amount of higher plant OM and algal OM	Bourbonniere and Meyers, 1996; Meyers, 1997
Pristane/Phytane (Pr/Ph)	Pr is preserved in initial oxidation and Ph in initial reduction. Pr/Ph is a redox parameter	Powell and McKirdy, 1973; Didyk et al., 1978; Peters et al., 2005
Tetraterpenoid β -carotane	Reducing conditions involving salinity stratification, evaporative conditions	Hall and Douglas, 1983; Brassell et al., 1988; Peters et al., 2005
Hopanes	Contributions of bacterial membranes, fungi, and cyanobacteria	Ourisson et al., 1979; Rohmer et al., 1992; Ourisson and Albrecht, 1992
Homo-hopane index	Redox conditions, salinity, and biodegradation	Peters and Moldowan, 1991; Peters and Moldowan., 1993
Gammacerane index	Salinity stratified or redox stratified water columns, evaporate or high-salinity environments	Sinninghe Damste et al., 1995; Ritts et al., 1999; Hanson et al., 2001; Sepúlveda et al., 2009; Manzi et al., 2007
Ts/(Ts+Tm) ratio*	Maturity, salinity, and source input	Seifert and Moldowan, 1978; Moldowan et al., 1986; Rullkötter and Marzi, 1988
C_{27} , C_{28} , and C_{29} regular steranes	C_{27} steranes derived from algae, phytoplankton and zooplankton; C_{29} steranes derived from vascular plants or specific freshwater microalgae	Huang and Meinschein, 1979; Volkman et al., 1986; Rieley et al., 1991; Volkman, 1998, 2003, 2005;
17α -hopanes/regular steranes ratio*	Proportions of organic matter from prokaryotic organisms versus eukaryotic organisms	Moldowan et al., 1985; Horsfield et al., 1993; Peters et al., 2005
Diasteranes index	Thermal maturation, redox condition, and source rock composition (carbonate vs siliciclastic)	Mello et al., 1988; Peters et al., 2005
C_{29} steranes $20\text{S}(20\text{S}+20\text{R})$	Thermal maturation, organofacies, weathering, and biodegradation	Seifert and Moldowan, 1986; Rullkötter and Marzi, 1988; Peters et al., 2005
C_{29} steranes $\alpha\beta\beta/(\alpha\alpha\alpha+\alpha\beta\beta)$	Thermal maturation, source input, and depositional environment	Seifert and Moldowan, 1986; Rullkötter and Marzi, 1988
C_{30} moretanes/hopane	Thermal maturation, source input, and depositional environment	Seifert and Moldowan, 1980; Rullkötter and Marzi, 1988

* Bulk and organic geochemical proxies have been used to define organofacies.

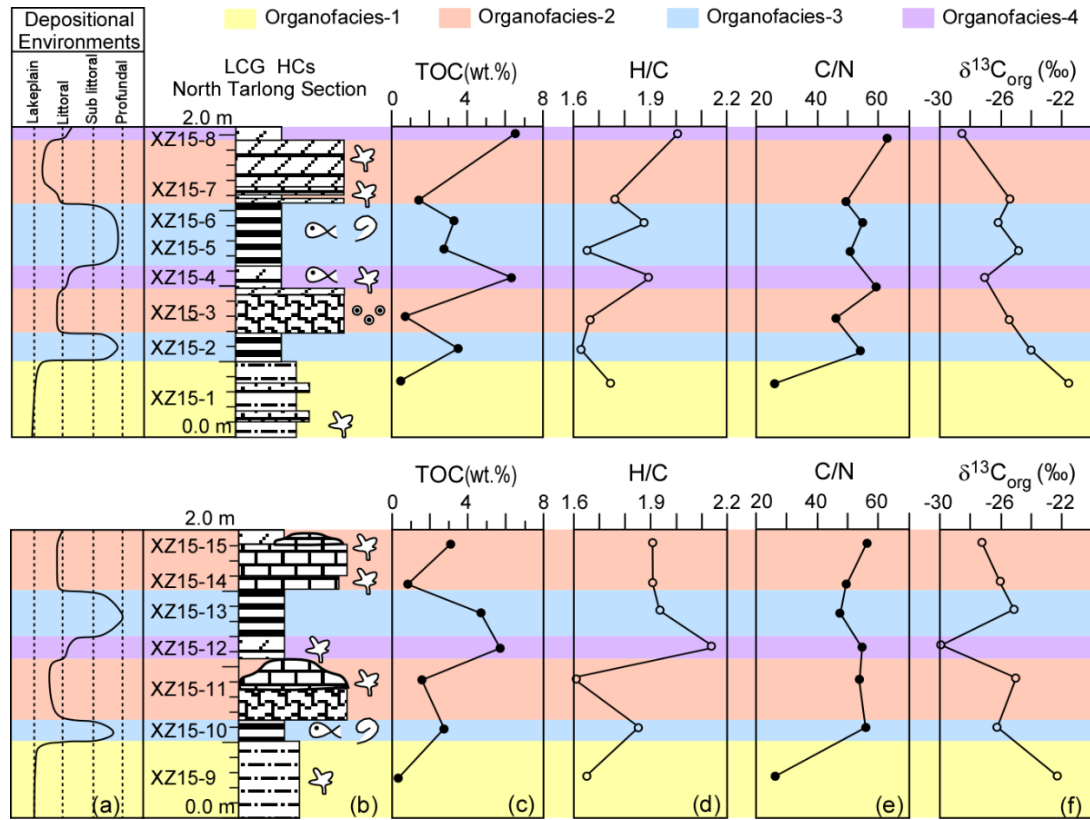


Figure 5. Correlation between geochemical proxies and lithofacies. These include interpreted depositional environments (a), lithofacies (b), total organic carbon (TOC) content (c), ratio of hydrogen over carbon (d), ratio of carbon over nitrogen (e), and stable organic carbon isotopic composition ($\delta^{13}\text{C}_{\text{org}}$) (f).

4.3.2. Organo-Facies 2. This lithofacies is distinguished by very high TOC content of 2.8–4.8 wt.%, medium H/C ratio of 1.63–1.94, high C/N ratio of 40.0–47.8, and medium to low $\delta^{13}\text{C}_{\text{org}}$ value of -26.2 to -24.1‰ (Table 1; Figure 7c–f). It is also described by dominance of short-chain *n*-alkanes, a low to medium TAR of 0.17–1.08, and low to medium hopane/sterane ratio of 1.3–4.9 (Table 3; Figure 8a, b, d).

OM in OF 2 may have been produced by algae and higher plants with very high productivity. High TOC suggests a very high primary productivity and good preservation of OM in the lake water and sediments (Meyers, 1997; 2003). OF 2 is moderately enriched with ^{12}C , suggesting a relatively strong fractionation of ^{12}C from ^{13}C in photosynthesis,

likely as a result of very high bioproductivity in the lake water. This is evidenced by a strong linkage between TOC and $\delta^{13}\text{C}_{\text{org}}$ values (Figure 7e). Additionally, OM in OF 2 is mainly a mixture of Type I and Type III kerogen, as indicated by medium H/C ratio and high C/N ratio (Tissot and Welte 1984; Meyers et al., 1997, 2003). The low to medium TAR and dominance of short-chain *n*-alkanes with high proportions of long-chain *n*-alkanes suggest the majority of OM in OF 2 was derived from algae and a large number of other from higher plant (Meyers and Ishiwatari, 1993; Bush and McInerney, 2013). Similar interpretation is also supported by a mixture of amorphous OM and phytoclasts observed under stereo- and polarizing microscope. The low to medium hopane/sterane ratio indicate minor to moderate input of bacteria OM to OF 2 (Ourisson et al., 1979; Rohmer et al., 1984; Volkman, 2003, 2005).

4.3.3. Organo-Facies 3. OF 3 is depicted by low to medium TOC content of 0.7–3.0 wt.%, low to medium H/C ratio of 1.61–1.91, high C/N ratio of 39.5–48.7, and medium to low $\delta^{13}\text{C}_{\text{org}}$ values of -27.2 to -25.1‰ (Table 1; Figure 7c–f). OF 3 is also outlined by dominance of mid-chain *n*-alkanes with a large number of short-chain *n*-alkanes, medium TAR of 0.31–0.59, and medium to high hopane/sterane ratio of 2.8–10.1 (Table 3; Figure 8a, b, d).

OM in OF 3 may have been produced by macrophytes or sphagnum and algae with relatively low productivity, and some of the OM may have been derived from bacteria or strongly modified by bacteria. The low to medium TOC suggest low–moderate primary productivity and poor preservation of OM in the lake (Meyers, 1997; 2003). OF 3 is moderately enriched in ^{13}C , suggesting relatively weak fractionation of ^{12}C from ^{13}C in photosynthesis, as a result of low–moderate bioproductivity in the lake

(Saltzman and Thomas, 2012). This is supported by a strong relationship between TOC and $\delta^{13}\text{C}_{\text{org}}$ values (Figure 7e). Moreover, OM in OF 3 is dominated by of Type I and Type III kerogens, as suggested by low–medium H/C ratio and high C/N ratio (Tissot and Welte 1984; Meyers et al., 1997, 2003). A medium TAR and dominance of mid-chain *n*-alkanes with high proportions of short-chain *n*-alkanes suggest most of OM in OF 3 was derived from macrophytes or sphagnum and a large number of other from algae (Meyers and Ishiwatari, 1993; Ficken et al., 2000; Bush and McInerney, 2013). A medium to high hopane/sterane ratio suggests nonnegligible input of bacterial OM or strong modification of bacteria on terrestrial and algal OM in OF 3 (Ourisson et al., 1979; Rohmer et al., 1992; Volkman, 2003, 2005). These interpretations are also supported by abundant amorphous OM and algal laminae, common phytoclasts, and sparse cyanobacteria observed under polarizing microscope.

4.3.4. Organo-Facies 4. This facies is characterized with extremely high TOC content of 5.9–6.5 wt.%, a high H/C ratio of 1.89–2.14, high C/N ratio of 36.4–49.9, and very low $\delta^{13}\text{C}_{\text{org}}$ value of -29.6 to -27.3‰ (Table 1; Figure 7c–f). OF 4 is also portrayed by dominance of short- and mid-chain *n*-alkanes, a low TAR of 0.15–0.38, and medium hopane/sterane ratio of 2.7–4.7 (Table 3; Figure 8a, b, d).

OM in OF 4 may have been mainly originated from algae with very high productivity, while a few others from macrophytes or sphagnum. The high TOC content suggests very high primary productivity and good preservation of OM in the lake (Meyers, 1997; 2003). OF 4 is extremely enriched in ^{12}C , suggesting strong fractionation of ^{12}C from ^{13}C in photosynthesis, likely as a result of high bioproductivity in the lake. This is also supported by a strong relationship between TOC and $\delta^{13}\text{C}_{\text{org}}$ values (Figure

7e). Furthermore, OM in OF 4 is mainly Type I kerogen with a large number of Type III kerogen, as suggested by a high H/C ratio and high C/N ratio (Tissot and Welte 1984; Meyers et al., 1997, 2003). A low TAR and dominance of short- and mid-chain *n*-alkanes suggest that the OM in OF 4 was mainly derived from algae with a large amount of OM from macrophytes or sphagnum (Meyers and Ishiwatari, 1993; Ficken et al., 2000; Bush and McInerney, 2013). This is also supported by abundant well-preserved algae with a few phytoclasts observed under polarizing microscope. Medium hopane/sterane ratio suggest a small amount of bacterial OM or moderate modification of bacteria on terrestrial and algal OM in OF 4 (Ourisson et al., 1979; Rohmer et al., 1992; Volkman, 2003, 2005).

4.4. DEPOSITIONAL CONDITIONS AND ORGANIC MATTER MATURITY

Four organo-facies can be identified using bulk geochemical parameters including total organic carbon content (TOC), ratio of hydrogen over carbon (H/C), ratio of carbon over nitrogen (C/N), and organic carbon isotopic composition ($\delta^{13}\text{C}_{\text{org}}$), as well as biomarker proxies including *n*-alkanes, terrestrial over aquatic ratio (TAR), and ratio of 17 α -hopanes over regular C₂₇₋₂₉ steranes. However, redox-, salinity-, and maturity-related proxies cannot define organo-facies in the HCs (Tables 1–3; Figure 8c, e–i).

4.4.1. Proxies Related to Redox Conditions. Several biomarker proxies have been used to interpret redox condition of lake water during the deposition of sediments in the HCs. Ratio of pristane over phytane (Pr/Ph) of all the samples in the HCs is 1.25–1.88, homohopane index is 0.09–0.49, and diasterane index is 0.11–0.54 (Table 3).

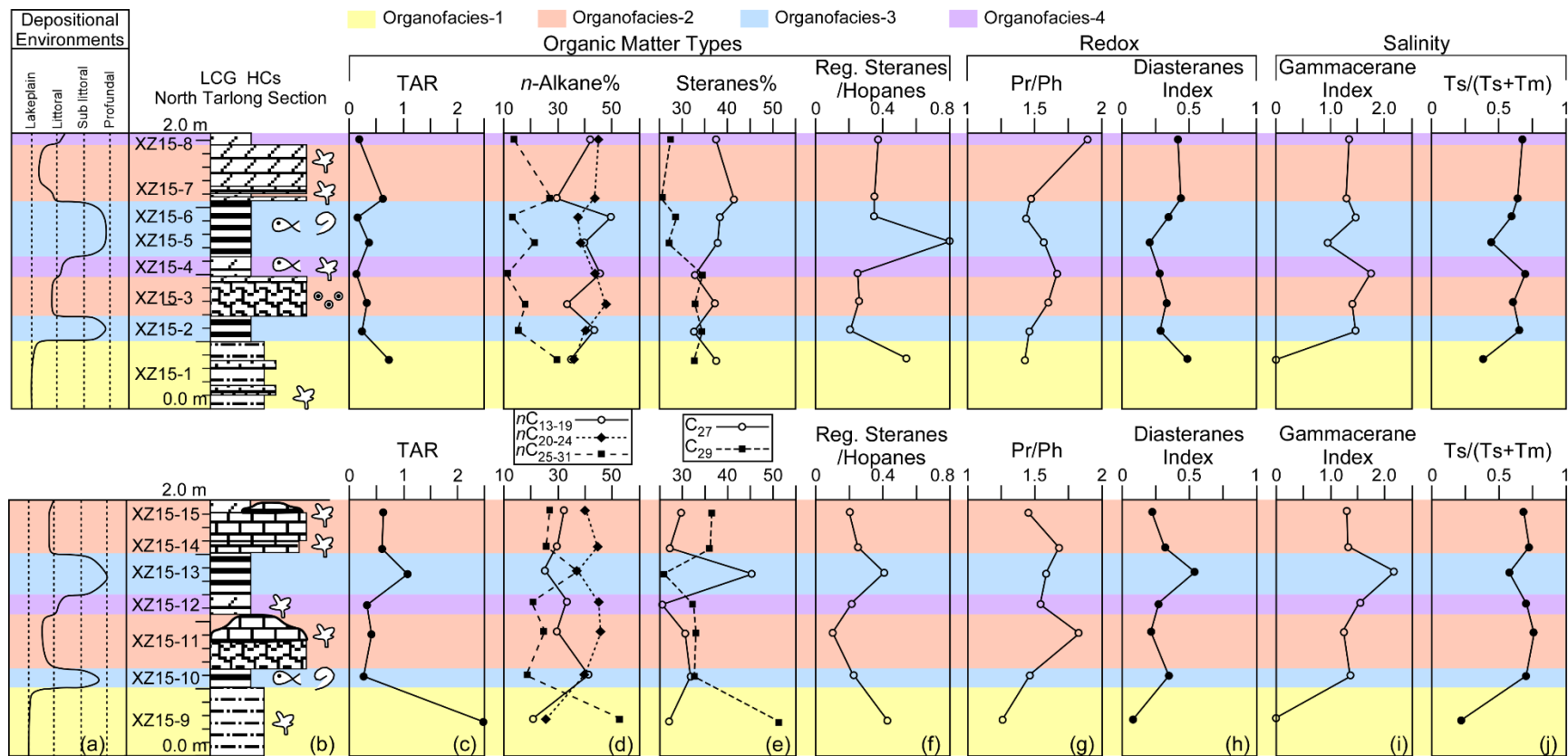


Figure 6. Correlation between biomarker proxies (c-j) and lithofacies (b) and interpreted depositional environments using sedimentary evidence (a). Biomarkers related to organic matter types include: terrestrial aquatic ratio (TAR) (c), proportions of short chain ($C_{13}-C_{19}$), intermediate-chain ($C_{20}-C_{24}$), and long-chain ($C_{25}-C_{31}$) n-alkanes (d), proportions of C_{27} and C_{29} regular steranes (e), regular steranes/17- α hopanes ratio (f); biomarkers related to redox conditions include: pristane/phytane ratio (Pr/Ph) (g) and Diasteranes index (h); biomarkers related to water column salinity include: Gammacerane index (i) and Ts/(Ts+Tm) ratio (j).

Table 3. Values of selected biomarker attributes of four organofacies

Sample No.	Peak ^a	CPI ^b	OEP ^c	N-alkanes (%) ^d			TAR ^e	Pr/Ph ^f	β-carotane ^g	Ga. Index ^h	Homo hop. Index ⁱ	Hop./Ste. ^j	Regular Ste. (%) ^k			Diast. Index ^l	Ts/(Ts+Tm) ^m	C ₃₀ hopane βα/αβ ⁿ	C ₂₉ S(S+R) ^o	C ₂₉ αα/(αα+ββ) ^p
				S	M	L							C ₂₇	C ₂₈	C ₂₉					
Lithofacies 1												Organofacies 1								
XZ15-1	C ₁₆	1.5	1.4	34	36	30	0.67	1.38	n. d.	n. d.	n. d.	1.9	37	30	33	0.49	0.38	0.13	0.36	0.51
XZ15-9	C ₂₉	2.1	1.6	20	24	56	2.51	1.25	n. d.	n. d.	n. d.	2.4	27	22	51	0.11	0.22	0.40	0.49	0.36
Lithofacies 2												Organofacies 2								
XZ15-6	C ₂₁	1.2	1.2	50	37	13	0.17	1.45	trace	1.48	0.32	2.9	39	32	29	0.35	0.60	0.10	0.53	0.41
XZ15-5	C ₂₁	1.3	1.4	40	38	22	0.39	1.57	n. d.	0.96	0.49	1.3	38	35	27	0.20	0.45	0.17	0.57	0.35
XZ15-2	C ₂₀	1.4	1.3	43	40	17	0.24	1.45	n. d.	1.48	0.09	4.9	33	33	34	0.28	0.64	0.15	0.53	0.43
XZ15-13	C ₂₅	1.4	1.3	25	36	39	1.08	1.58	trace	2.17	0.46	2.5	45	29	26	0.54	0.59	0.14	0.38	0.30
XZ15-10	C ₂₀	1.3	1.2	42	40	18	0.30	1.45	n. d.	1.39	0.48	4.5	32	35	33	0.35	0.70	0.06	0.53	0.43
Lithofacies 3												Organofacies 3								
XZ15-7	C ₂₁	1.3	1.3	29	43	28	0.59	1.47	trace	1.34	0.23	2.8	42	34	24	0.42	0.63	0.12	0.40	0.47
XZ15-3	C ₂₁	1.4	1.3	33	48	19	0.31	1.61	n. d.	1.42	n. d.	3.8	37	30	33	0.34	0.61	0.16	0.55	0.43
XZ15-15	C ₂₁	1.3	1.3	32	39	29	0.57	1.44	trace	1.35	0.22	5.0	30	34	36	0.43	0.67	0.11	0.48	0.41
XZ15-14	C ₂₃	1.3	1.3	29	44	27	0.56	1.67	n. d.	1.36	n. d.	4.0	27	37	36	0.30	0.73	0.11	0.43	0.47
XZ15-11	C ₂₃	1.3	1.2	30	46	24	0.46	1.81	n. d.	1.25	n. d.	10.1	31	36	33	0.20	0.76	0.02	0.60	0.36
Lithofacies 4												Organofacies 4								
XZ15-8	C ₂₁	1.4	1.3	42	44	14	0.19	1.88	n. d.	1.38	0.48	2.7	38	35	27	0.40	0.66	0.09	0.54	0.46
XZ15-4	C ₂₁	1.4	1.3	45	44	11	0.15	1.64	n. d.	1.75	n. d.	4.1	33	32	35	0.28	0.68	0.15	0.56	0.40
XZ15-12	C ₂₁	1.3	1.2	34	44	22	0.38	1.54	n. d.	1.54	0.31	4.7	26	42	32	0.27	0.69	0.07	0.53	0.44

^a Peak of *n*-alkanes in TIC traces chromatogram; ^{b-c} Peak areas of *n*-alkanes in TIC traces chromatogram measured for calculating the CPI and OPE values:

CPI=[(nC₂₅+nC₂₇+nC₂₉+nC₃₁)/(nC₂₄+nC₂₆+nC₂₈+nC₃₀)+(nC₂₅+nC₂₇+nC₂₉+nC₃₁)/(nC₂₆+nC₂₈+nC₃₀+nC₃₂)]/2; OEP=(nC₂₅+6×nC₂₇+nC₂₉)/[4×(nC₂₆+nC₂₈)]; ^d Peak of *n*-alkanes in TIC traces chromatogram, S: short chain *n*-alkanes (C₁₂₋₁₉), M: mid-chain *n*-alkanes (C₂₀₋₂₄), and L: long chain *n*-alkanes (C₂₅₋₃₅) normalized to a total of 100%; ^e Peak areas of normal alkanes in TIC traces chromatogram; TAR=(nC₂₇+nC₂₉+nC₃₁)/(nC₁₅+nC₁₇+nC₁₉); ^f Peak areas of isoprenoid in TIC traces from GC for acquiring pristane/phytane (Pr/Ph); ^g β -Carotane in *m/z* 125 and 558 chromatogram, not determined (n.d.); ^h Peak areas in *m/z* 191 chromatogram: gammacerane index (Ga. Index)=10×gammacerane/(gammacerane+C₃₀ 17 α ,21 β -hopane); ⁱ Homohopane index (Homohop. Index) is calculated as peak areas of C₃₅ 17 α ,21 β , (22R + 22S)-pentakishomohopanes over peak areas of C₃₃ counterparts in *m/z* 191 chromatogram; ^j 17 α -Hopanes/regular steranes (Hop./Ste.) is calculated as peak areas of 17 α , (22S+22R)-hopanes consist of the C₂₉₋₃₃ pseudohomologs in *m/z* 191 over sum of 5 α ,14 α ,17 α , (20R + 20S) and 5 α ,14 β ,17 β , (20R + 20S) of C₂₇ cholestanes, C₂₈ methylcholestanes, and C₂₉ ethylcholestanes in *m/z* 217 chromatogram; ^k Peak areas of 5 α ,14 α ,17 α , (20R + 20S) and 5 α ,14 β ,17 β , (20R + 20S) of C₂₇ cholestanes, C₂₈ methylcholestanes, and C₂₉ ethylcholestanes calculated in *m/z* 217 chromatogram and normalized to a total of 100%; ^l Diasteranes index (Diast. Index) is calculated as peak areas of C₂₇ 13 β ,17 α , (20R + 20S)-diacholestanes over sum of C₂₉ 5 α ,14 α ,17 α , (20R + 20S)-24-ethylcholestanes in *m/z* 217 chromatogram; ^m Peak areas in *m/z* 191 chromatogram, Tm: 17 α -22,29,30-trisnorhopane-C₂₇; Ts: 18 α -22,29,30-trisnorhopane-C₂₇; ⁿ Peak area of C₃₀ 17 β ,21 α -moretane over C₃₀ 17 α ,21 β -hopane in *m/z* 191 chromatogram; ^o Peak areas of (20R + 20S) over sum of (20R + 20S) and (20R + 20S) of C₂₉ ethylcholestanes in *m/z* 217 chromatogram; ^p Peak areas of 5 α ,14 α ,17 α , (20R + 20S) over sum of 5 α ,14 α ,17 α , (20R + 20S) and 5 α ,14 β ,17 β , (20R + 20S) of C₂₉ ethylcholestanes in *m/z* 217 chromatogram.

Pr/Ph ratio is generally considered as a redox parameter because phytol converts to pristane in oxic conditions and phytane in anoxic conditions (Didyk et al., 1978). Similar Pr/Ph ratios of 1–2 in the HCs suggest that all samples may have been deposited in dysoxic lake water. However, Pr/Ph values in 1–3 are not recommended for determining redox condition of depositional environments (Peters et al., 2005). In addition, Pr/Ph ratios are known to be affected by maturation (Tissot and Welte, 1984) and by differences in precursors for acyclic isoprenoids (Volkman and Maxwell, 1986; ten Haven et al., 1987). Thermal diagenesis favors preservation of pristane to phytane, result in an increasing Pr/Ph value with maturity (Didyk et al., 1978). Volkman (1988) also suggests that archaeobacteria can be important sources of phytane.

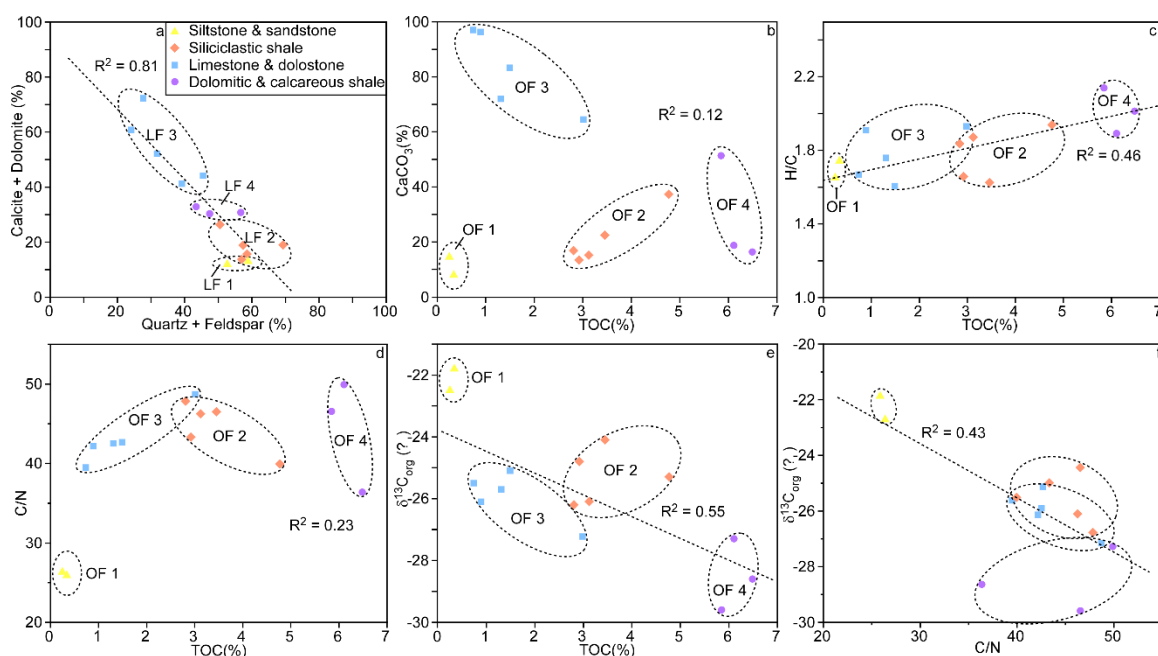


Figure 7. Four types of organofacies. They are differentiated by plots of total organic carbon (TOC) content and stable organic carbon isotope ($\delta^{13}\text{C}_{\text{org}}$) (a), TOC and hydrogen/carbon ratio (H/C) (b), TOC and terrestrial aquatic ratio (TAR) (c), ternary diagram of proportions of short-chain, mid-chain, and long-chain n-alkanes (d), plots of TAR and Ts/(Ts+Tm) ratio (e) and pristane/phytane ratio (Pr/Ph) and Gammacerane index (f).

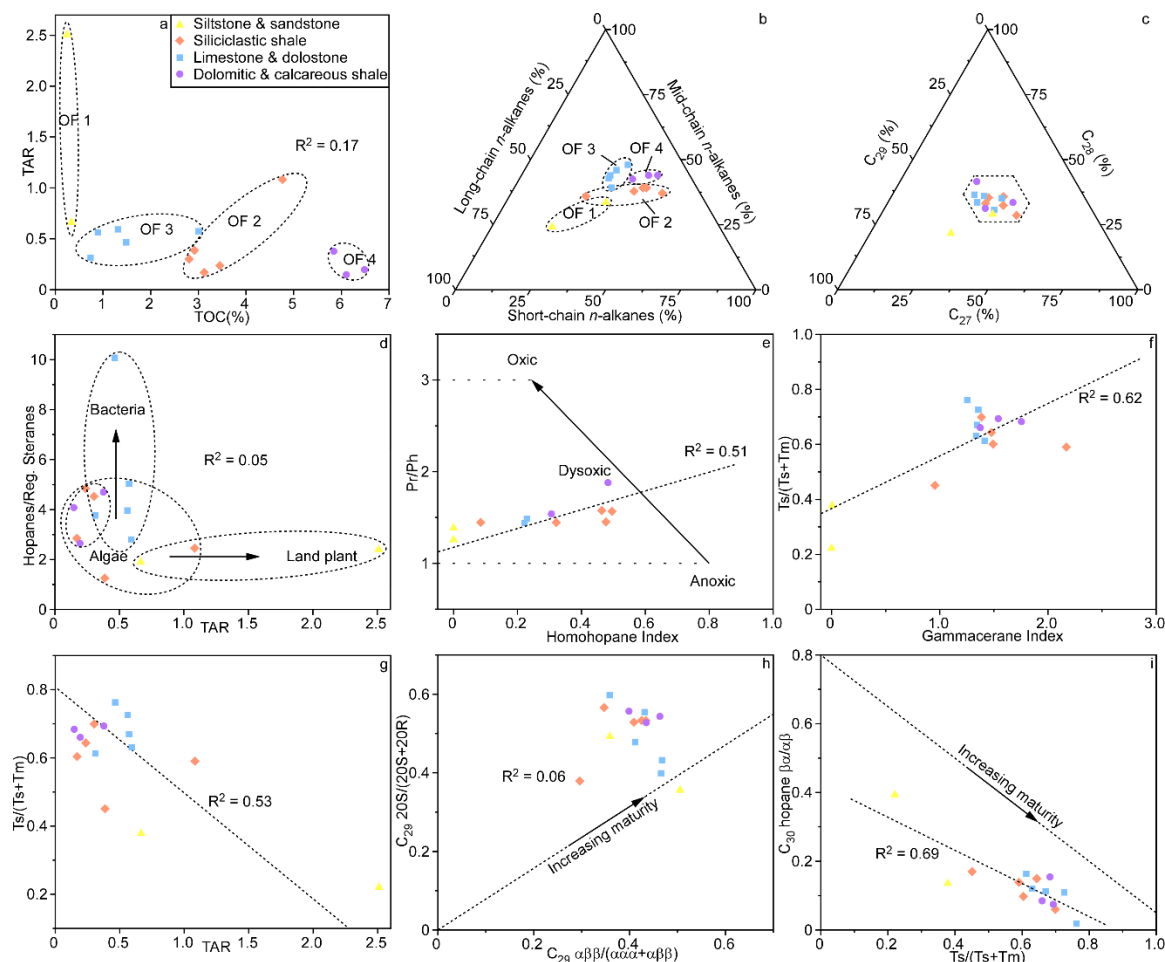


Figure 8. Four types of organofacies. They are differentiated by plots of total organic carbon (TOC) content and stable organic carbon isotope ($\delta^{13}\text{C}_{\text{org}}$) (a), TOC and hydrogen/carbon ratio (H/C) (b), TOC and terrestrial aquatic ratio (TAR) (c), ternary diagram of proportions of short-chain, mid-chain, and long-chain n-alkanes (d), plots of TAR and Ts/(Ts+Tm) ratio (e) and pristane/phytane ratio (Pr/ Ph) and Gammacerane index (f).

Homohopane index is the ratio between the peak area of $\text{C}_{35} 17\alpha, 21\beta, (22\text{R}+22\text{S})$ -pentakishomohopanes and C_{33} counterparts. The low value of homohopane index of all the samples in the HCs suggest dysoxic water body in the lake because low homohopane index have been experientially used to indicate oxic depositional environment (Peters and Moldowan, 1993). The low homohopane index may be influenced by thermal maturation, biodegradation, and sulfur availability in depositional environments (Peters and

Moldowan, 1991). Nevertheless, a strong positive correlation between homohopane index and Pr/Ph indicates that all samples in the HCs were probably deposited in dysoxic lake water (Figure 8e). Similar redox condition of all the samples in the HCs suggest lithofacies may not be used to interpret redox condition and geochemical proxies related to redox condition may not be used to differentiate organofacies in this study. Alternatively, these proxies may not be used to detect subtle changes of redox condition during lake expansion and contraction.

Diasteranes index indicates depositional conditions when samples are at a similar level of thermal maturity (Peters et al., 2005), and is commonly used to distinguish OM from carbonate versus clastic depositional environments as clay minerals catalyze the conversion of sterols to diasterenes (Mello et al., 1988). Low diasterane index of all samples in the HCs suggest dysoxic environments because acidic (low pH) and oxic (high Eh) conditions facilitate generation of diasterene during diagenesis (Moldowan et al., 1986). This interpretation is consistent with that from Pr/Ph and homohopane index.

However, dysoxic lake water indicated by moderate Pr/Ph ratio and low homohopane index in the HCs is contradicted with oxic lake water of Lithofacies 1 and 3 and anoxic condition of Lithofacies 2 interpreted from sedimentary evidences. This suggests that redox condition of lake water interpreted from sedimentary evidences may not be accurate and can be improved with assistance of geochemical proxies. In addition, low value of diasteranes index is typically interpreted as clay-poor or carbonate sediments deposited in high pH and low Eh waters, which facilitate calcite and dolomite precipitation and OM preservation (Mello et al., 1988; Peters et al., 2005). However, diasterane index may not be applied in distinguishing redox conditions of water column

in this study because the trend of diasterane index is not in accordance with trend of Pr/Ph (Figure 6g, h). Additionally, siliciclastic shales have relative high values of diasterane index than dolomitic and calcareous shales in the lower two HCs (Table 3; Figure 6h). But siliciclastic shales have lower values of diasterane index than that in dolomitic and calcareous shales in the upper two HCs (Table 3; Figure 6h). This suggests that the diasterane index may not be controlled by amount of clay but depend on relative content of clay compared with TOC (e.g., Van Kaam-Peters et al., 1998).

4.4.2. Proxies Related to Lake Water Salinity. Gammacerane index, β -carotane, and Ts/(Ts+Tm) ratios have been used to interpret salinity of the water body in the lake. Gammacerane is present in Lithofacies 2, 3 and 4, but not in Lithofacies 1 the samples besides interbedded and interlaminated coarse siltstone and very fine sandstone in the HCs, with gammacerane index ranges in 0.96–2.17 (Table 3). Trace β -carotane is present in two black shales and two dolostones, but absent in all the other samples in the HCs (Table 3). 8α -22,29,30-trisnorneohopane- C_{27} (Ts) and 17α -22,29,30-trisnorhopane- C_{27} (Tm) are present in all samples in the HCs. Lithofacies 1 has low Ts/(Ts+Tm) value of 0.22–0.33, while Lithofacies 2, 3, and 4 have moderate value of 0.38–0.57 (Table 3).

Gammacerane index is widely used as a proxy of salinity because gammacerane is associated with planktonic and bacteriovorous ciliates (Grice et al., 1998), which occur at the interface between oxic and anoxic zones in a stratified water columns (Sinninghe Damste et al., 1995; Sepúlveda et al., 2009). High abundance of gammacerane usually typifies evaporative hypersaline environments in stratified water columns (Ritts et al., 1999; Hanson et al., 2000, 2001; Manzi et al., 2007). Low gammacerane index in Lithofacies 1-4 suggests all the samples deposited in relatively fresh lake water.

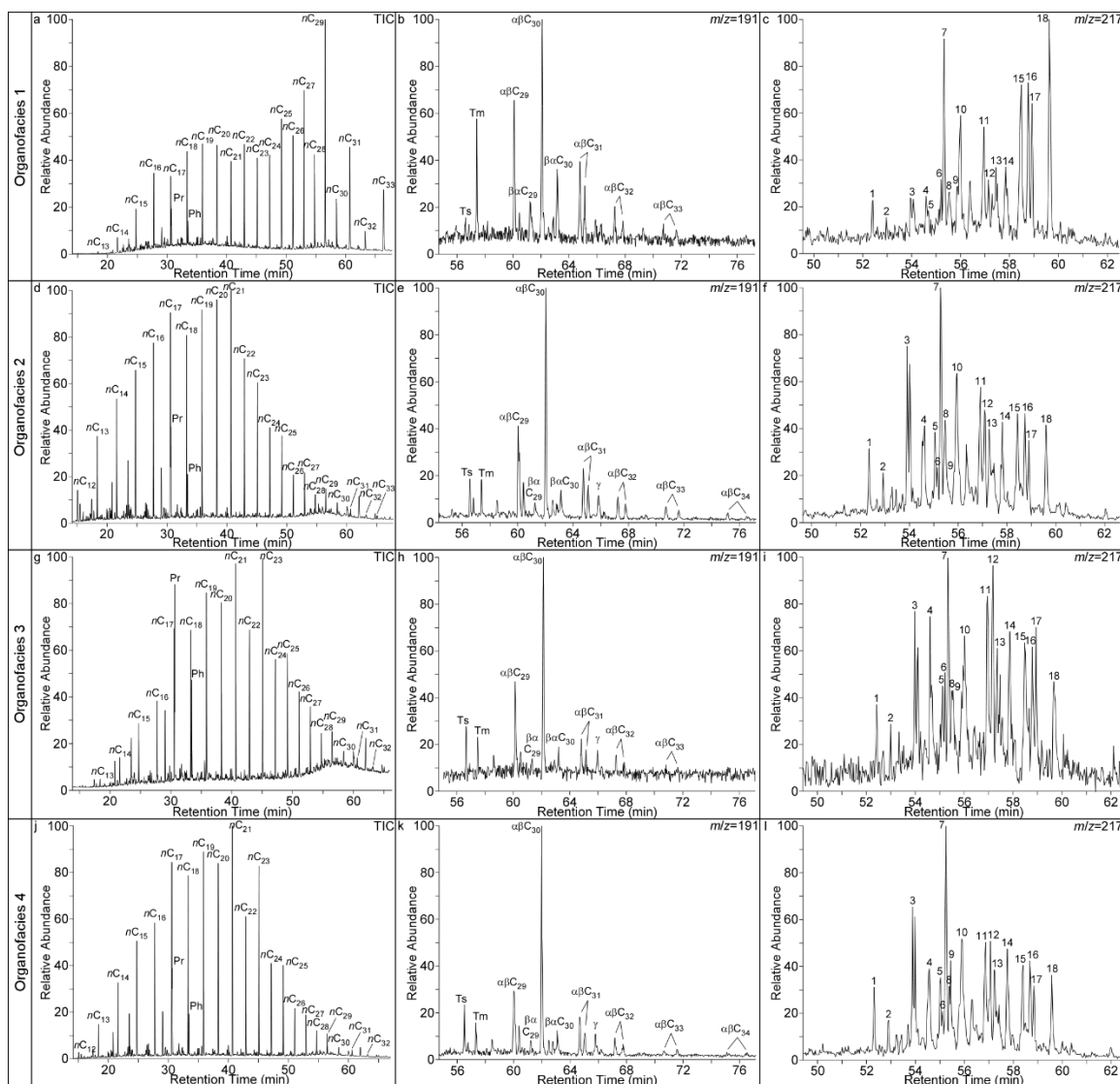


Figure 9. Representative mass chromatograms of n-alkanes (TIC), hopanes ($m/z=191$), and steranes ($m/z=217$) from four organo-facies. Ts: 18α -22,29,30-Trisnorneohopane; Tm: 17α -22,29,30-Trisnorhopane; $\alpha\beta$ 29: 17α , 21β -30-Norhopane; $\beta\alpha$ 29: 17β , 21α -30-Normoretane; $\alpha\beta$ 30: 17α , 21β -Hopane; $\beta\alpha$ 30: 17β , 21α -Moretane; $\alpha\beta$ 31: 22S&R- 17α , 21β -Homohopane; Ga: Gammacerane; $\alpha\beta$ 32: 22S&R- 17α , 21β -Bishomohopane; $\alpha\beta$ 33: 22S&R- 17α , 21β -Trishomohopane; $\alpha\beta$ 34: 22S&R- 17α , 21β -Tetrashomohopane; 1: 20S- 13β , 17α -Diacholestane; 2: 20R- 13β , 17α -Diacholestane; 3: 20S-24-Methyl- 13β , 17α -cholestanes; 4: 20R-24-Methyl- 13β , 17α -cholestanes; 5: 20S- 5α , 14α , 17α -cholestane; 6: 20R- 5α , 14β , 17β -cholestane; 7: 20S-24-Ethyl- 13β , 17α -cholestanes; 8: 20S- 5α , 14β , 17β -cholestane; 9: 20R- 5α , 14α , 17α -cholestane; 10: 20R-24-Ethyl- 13β , 17α -cholestanes; 11: 20S-24-Methyl- 5α , 14α , 17α -cholestanes; 12: 20R-24-Methyl- 5α , 14β , 17β -cholestanes; 13: 20S-24-Methyl- 5α , 14β , 17β -cholestanes; 16: 20R-24-Ethyl- 5α , 14β , 17β -cholestanes; 17: 20S-24-Ethyl- 5α , 14β , 17β -cholestanes; 18: 20R-24-Ethyl- 5α , 14α , 17α -cholestanes.

Table 4. Major characteristics and interpreted depositional environments and conditions of litho- and organo-facies in this study

Organofacies	Chemical Composition	Organic Matter	Redox Condition	Salinity	Lithofacies	Sedimentary Structures	Fossils	Environment
Organofacies 1	Low TOC & low H/C, low C/N, & high $\delta^{13}\text{C}_{\text{org}}$	Low productivity, mainly higher plant, minor algae & macrophytes	Dysoxic	Fresh lakewater	Lithofacies 1 Interlaminated & interbedded siltstone & sandstone	weakly laminated, erosional bases, & possible rootlets	Abundant plant remains & minor amorphous OM	High-energy Lake-plain littoral
Organofacies 2	High TOC, medium H/C, high C/N, & medium-low $\delta^{13}\text{C}_{\text{org}}$	High productivity, mainly algae & higher plants	Dysoxic	Fresh lakewater	Lithofacies 2 Siliciclastic shale	Well-parallel mm-to-sub-mm laminated, climbing rippled, & erosional	Common phytoclasts amorphous OM, ostracods, & fish scales	Low-energy profundal
Organofacies 3	Low-medium TOC, Medium H/C, high C/N, & medium-low $\delta^{13}\text{C}_{\text{org}}$	Low productivity, mainly algae & macrophytes, minor bacteria	Dysoxic	Fresh lakewater	Lithofacies 3 Wackestone & dolostone	Well laminated, algal laminated, & thrombolitic	Common ooids, ostracods, intraclasts, phytoclasts, & algae	Low to high energy littoral-sub littoral
Organofacies 4	Extremely high TOC, high H/C, high C/N, & very low $\delta^{13}\text{C}_{\text{org}}$	High productivity, mainly algae, minor macrophytes	Dysoxic	Fresh lakewater	Lithofacies 4 Calcareous and dolomitic shales	well-parallel sub-mm to mm interlaminated, algal laminated	Abundant amorphous OM phytoclasts, & ostracods	Low-energy littoral

Chemical composition, organic matter, redox condition, and salinity are interpreted on the basis of organic geochemical proxies listed in Table 2.

The tetraterpenoid hydrocarbon β -carotane is considered to be formed in saline water, due to high productivity of specific algae and bacteria during widespread desiccation in arid climate (Hall and Douglas, 1983; Brassell et al., 1988; Peters et al., 2005). Absence or trace amount of β -carotane suggests all lithofacies were likely deposited in fresh lake water. This interpretation is consistent with that from the gammacerane index in the HCs. However, the fresh lake water condition indicated by absence or trace amount of gammacerane and β -carotane is in conflict with the interpretation of saline lake water for Lithofacies 3 and 4 interpreted from sedimentary evidence. This suggests that salinity of lake water interpreted from sedimentary evidence may not be accurate and can be improved with assistance of geochemical proxies. Alternatively, salinity-related proxies may not be used to detect subtle changes of lakewater salinity in the HCs.

$Ts/(Ts+Tm)$ ratio may be used as a salinity-sensitive proxy when samples are at similar thermal maturity level, because it increases in hypersaline depositional environments (Moldowan et al., 1986; Rullkötter and Marzi, 1988; Peters et al., 2005). Low $Ts/(Ts+Tm)$ values suggest all the lithofacies may have been deposited in fresh lake water. This is also supported by a strong positive correlation between gammacerane index and $Ts/(Ts+Tm)$ ratio of all samples (Figure 8f). Alternatively, $Ts/(Ts+Tm)$ ratio is indicative of type of OM because it is partially controlled by contribution of organisms to OM (Moldowan et al., 1986). $Ts/(Ts+Tm)$ ratio has similar pattern with relative abundance of mid-chain *n*-alkanes (Figure 6d, j) and opposite trend with long-chain *n*-alkanes, C_{29} -steranes, TAR, and ratio of regular steranes over hopanes in the HCs (Figure 6c, d, e, f). This is supported by a moderate negative correlation between $Ts/(Ts+Tm)$ and

TAR (Figure 8g). Therefore, low $T_s/(T_s+T_m)$ values of samples in the HCs can alternatively indicate the OM source is from specific macrophytes or sphagnum with possible microbial modification of the OM during deposition.

4.4.3. Maturity-Related Biomarkers. Application of biomarker in types of OM and environmental condition requires consideration of level of maturity, which has potential influence on biomarkers (Peters et al., 2005). Maturity indicators, such as carbon preference index (CPI), odd even preference (OEP), ratio of $\beta\beta/(\beta\beta+\alpha\alpha)$ stereotypes in C_{29} steranes, ratio of $20S/(20S+20R)$ stereochemistry in C_{29} steranes, and ratio of C_{30} $17\beta,21\alpha$ -moretane over C_{30} $17\alpha,21\beta$ -hopane (C_{30} -hopane $\beta\alpha/\alpha\beta$) have been used to interpret the thermal maturity of OM in the samples. The CPI of all samples is 1.2–2.1 and OEP is 1.2–1.6 (Table 3). The ratio of C_{29} $20S/(20S+20R)$ is 0.36–0.57, C_{29} $\beta\beta/(\beta\beta+\alpha\alpha)$ is 0.35–0.51, and C_{30} -hopane $\beta\alpha/\alpha\beta$ is 0.02–0.40 in all samples (Table 3).

The relatively high CPI and OEP with similar values of all the samples in the HCs suggest moderate to high thermal maturity of the OM (Bray and Evans, 1961; Scalan and Smith, 1970), indicating that all samples have similar maturity. In addition, the values of C_{29} $20S/(20S+20R)$ and C_{29} $\beta\beta/(\beta\beta+\alpha\alpha)$ ratios of all the samples suggest moderate to high maturity of OM. Isomerization at C-20 in C_{29} $5\alpha,14\alpha,17\alpha$ -steranes causes an increase of the $20S/(20S+20R)$ ratio with increasing thermal maturity while isomerization at C-14 and C-17 in the C_{29} $20S$ and $20R$ regular steranes causes an increase of the $\beta\beta/(\beta\beta+\alpha\alpha)$ ratio (Seifert and Moldowan et al., 1986). However, the cross points of $20S/(20S+20R)$ and $\beta\beta/(\beta\beta+\alpha\alpha)$ for C_{29} steranes of all the samples are off the maturity trend line (Figure 8h). The disagreement could be caused by different levels of clay catalysis (Huang et al., 1990) and different organo-facies of the samples (Moldowan et

al., 1986). Moreover, a small ratio of C₃₀-hopane $\beta\alpha/\alpha\beta$ of all the samples suggests moderate to high thermal maturity of the OM, because 17 α ,21 β -hopane are thermally more stable than 17 β ,21 α -moretane and the C₃₀-hopane $\beta\alpha/\alpha\beta$ ratio decreases with thermal maturity (Seifert and Moldowan et al., 1986). However, the plots of C₃₀-hopane $\beta\alpha/\alpha\beta$ ratio and Ts/(Ts+Tm) ratio of all the samples in the HCs are off the maturity trend line with strong correlation (Figure 8I). This offline trend could be explained by influence of OM input or depositional environment on both C₃₀-hopane $\beta\alpha/\alpha\beta$ and Ts/(Ts+Tm) ratios (Rullkötter and Marzi, 1988).

Above all, OM of all samples may have been formed in similar condition of fresh dysoxic lake water and preserved with similar thermal condition, suggesting geochemical proxies related to redox condition, salinity, and maturity may not be used to characterize organo-facies in meter-scale HCs.

5. DISCUSSION

5.1. PROXIES DEFINITIVE OF ORGANO-FACIES

Four organo-facies can be identified using bulk geochemical parameters including TOC, H/C ratio, C/N ratio, and $\delta^{13}\text{C}_{\text{org}}$ value, as well as biomarker proxies including *n*-alkanes, TAR, and hopane/sterane ratio. However, each biomarker proxy may not be regarded as definitive OM type indicator to differentiate organo-facies in this study.

Distribution and abundance of *n*-alkanes may indicate types and maturity of OM. However, absolute amount of terrestrial OM is disproportionately over estimated based on *n*-alkanes, as land plants typically contain higher proportions of *n*-alkanes than aquatic

OM (Cranwell et al., 1987; Goossens et al., 1989; Meyers and Ishiwatari, 1993). In addition, lacustrine algae (e.g. *Botryococcus braunii*) may contribute to the C₂₇-C₃₃ *n*-alkanes. (Moldowan et al., 1985; Derenne et al., 1988; Lu et al., 2018). Furthermore, some *n*-alkanes are also sensitive to thermal maturation and biodegradation (Tissot and Welte, 1984). Nonetheless, relative abundance of short-chain *n*-alkanes have a similar trend with H/C ratio and opposite trend with relative abundance of long-chain *n*-alkanes and TAR in the four HCs (Figures 5c, d, 6d), suggesting *n*-alkanes is valuable for determining changes in contribution of OM from terrestrial or aquatic systems. In addition, a moderate correlation between H/C ratio and TOC and no correlation between TAR and TOC (Figure 8a) suggest TOC may have been affected by kerogen types instead of OM types. Low C/N ratio (≥ 10) is commonly used as a proxy for OM derived from terrestrial higher plant (Meyers, 1997). However, C/N ratio has an opposite trend with relative abundance of long-chain *n*-alkanes and TAR in the four HCs (Figures. 5e, 6c, d), suggesting C/N ratio may not be used to differentiate terrestrial and aquatic OM in this study. This is also supported by irrelevance between C/N ratio and TOC (Figure 7d) and a weak negative correlation between C/N ratio and $\delta^{13}\text{C}_{\text{org}}$ value (Figure 7f).

Hopanoids are significant source-indicating biomarkers for bacteria derived organic matter (Ourisson et al., 1979; Rohmer et al., 1992). Hopanes in all the samples have relatively high abundance and similar compound distributions. Hopanes mainly consist of C₂₇ to C₃₅ 17 α ,21 β -hopanes with C₃₀-hopane as the major compound. Relatively low abundance of C₂₉ to C₃₁ 17 β ,21 α -moretanes were detected in all the samples. Hopanes in all the samples suggest input of bacterial OM or bacterial modification on terrestrial and algal OM during deposition.

Relative abundance of C₂₇, C₂₈, and C₂₉ regular steranes on a ternary diagram may be used to differentiate OM source input and depositional settings (Moldowan et al., 1985). C₂₇ steranes are predominately derived from algae and diatom from lacustrine deposits (Volkman, 2003). C₂₈ steranes typically constitute the sterols of specific algae, such as Haptophytes, Cryptophytes, and Prasinophyceae (Goad et al., 1983; Volkman, 1986) and leaf waxes of higher plants (Rieley et al., 1991; Volkman, 2003). C₂₉ steranes are mainly associated with the sterol composition of vascular plants (Rieley et al., 1991; Volkman, 1986). C₂₇, C₂₈, and C₂₉ regular steranes have similar relative abundance in all samples in the HCs (Table 3; Figure 8c), suggesting a mixture of OM derived from higher plants and algae. However, C₂₉ steranes have been also reported in specific microalgae, such as Chrysophyceae, Eustigmatophyceae, and Chlorophyceae and cyanobacteria (Volkman et al., 1998, Volkman, 2003, 2005). C₂₇-steranes have a similar trend with that of short-chain *n*-alkanes, while C₂₉-steranes have a similar trend with long-chain *n*-alkanes in the lower two HCs (Figure 6d, e). But C₂₇-steranes have an opposite trend with that of the short-chain *n*-alkanes, while C₂₉-steranes have an opposite trend with long-chain *n*-alkanes in the upper two HCs (Figure 6d, e). This suggests C₂₇, C₂₈, and C₂₉ regular steranes may not be effective to different type of OM in the HCs, likely due to diverse OM origins of the C₂₇, C₂₈, and C₂₉ regular steranes. Alternatively, it may be caused by the too much overlap of distribution of type of OM on ternary diagram of C₂₇, C₂₈, and C₂₉ regular steranes (Moldowan et al., 1985). Thus, relative abundance of C₂₇, C₂₈, and C₂₉ regular steranes may not be appropriate to characterize organo-facies in the HCs of this study.

Therefore, we emphasize that we do not regard each geochemical index as single, definitive indicator of the type of OM because some biomarkers may have diverse origins and they may have been altered by biological effect and diagenesis. Care must be taken using single source-related. A reasonable assessment will need to be quantitatively taken, combining all the effective geochemical indices and petrographic evidence.

5.2. CORRELATION BETWEEN LITHO- AND ORGANO-FACIES

Four organofacies are one-to-one correlated with four lacustrine lithofacies in the four HCs, suggesting litho- and organo-facies are linked and may have been controlled by sedimentary processes (Figures 7b–f, 8a–b). Similarities and differences of four types of litho- and organo-facies are summarized in Table 4 and Figure 9.

Organofacies (OF) 1 corresponds to Lithofacies (LF) 1 of interbedded and interlaminated coarse siltstone and very fine sandstone. LF 1 is a transgressive deposit experienced wave reworking in relatively high-energy beach and littoral environments during initial lake expansion. OM in OF 1 was mainly originated from higher plants and minor from algae and macrophytes. The small amount of algal OM suggests that the lake was shallow, and aqueous paleoproductivity was low during early lake expansion. The low TOC may be caused by the low productivity as well as dilution of siliciclastic sediments at the lake margin.

OF 2 is linked with LF 2 of siliciclastic shale. The shale was deposited in a low-energy profundal environment as a pelagic or fine-grained density flow deposit during maximum lake expansion. OM in OF 2 was derived from algae and terrestrial higher. Algal growth was likely intensified due to the large lake area while higher plants were

less abundant because the long transport distance and time would have increased wood decay and diminished the supply. Therefore, the relatively high TOC content can be attributed to a high algal productivity and low dilution by siliciclastic sediments.

OF 3 coincides with LF 3 of wackestone and dolostone. The carbonates were likely formed in an evaporative, saline environment with minimal clastic influx in a shallow lake. They were deposited during lake contraction under an arid to semi-arid climate (Yang et al., 2010). The limited clastic influx and the evaporative condition suggest that fresh river water influx into the lake was low so that the influx of higher plant debris was limited. OM in OF 3 was principally derived from algae and macrophytes with a minor contribution from bacteria. The moderate TOC content suggests that the aquatic macrophytes and algae were accumulated in the lake, but their development was limited by supply of necessary nutrients, such as N, P, Na, and Fe, by the small amount of river influx. In addition, low to moderate TOC may be caused by intense microbial decomposition of OM.

OF 4 is associated with LF 4 of dolomitic and calcareous shale. They were deposited in low-energy lake water in littoral environments during the latest regression under semi-arid subhumid climate (Yang et al., 2010). OM in OF 4 was mainly derived from algae with a minor contribution from macrophytes. Sufficient nutrient and oxygen supplied by influx may provide appropriate conditions for growth of algae and macrophytes, resulting in high paleoproductivity.

In summary, litho- and organo-facies are linked. The organofacies defined by proxies indicative of abundance and type of OM, were likely controlled by changes of

contribution from higher plants and algae to OM in the deposits as depositional environments change during lake shoreline transgression and regression.

6. CONCLUSIONS

A centimeter-scale investigation of mixed carbonate and siliciclastic lacustrine deposits in LCG HCs shows that litho- and organo-facies are one-to-one correlated, suggesting they are linked through the physical, chemical, and biological processes during short-term lake expansion and contraction. Four lithofacies include interbedded and interlaminated coarse siltstone and very fine sandstone, siliciclastic shale, wackestone and dolostone, and calcareous and dolomitic shales have been identified. Four organo-facies are identified on the basis of specific bulk geochemical parameters related to chemical composition of organic matter, including TOC, H/C, C/N, and $\delta^{13}\text{C}_{\text{org}}$ and biomarker proxies related to types of organic matter, including *n*-alkanes, TAR, and hopanes/regular steranes rather than proxies related to redox condition, salinity, and maturity. Nevertheless, these proxies improve interpretation of depositional environments of lacustrine deposits interpreted from lithofacies alone at a cm-m scale. The one-to-one correlation of litho- and organo-facies suggests litho- and organo-facies are linked. The organofacies were likely controlled by changes of contribution from higher plants and algae to OM in the deposits as depositional environments change during lake shoreline transgression and regression. The results demonstrate that a holistic approach using lithologic and organic geochemical data is useful in delineating cyclic

changes of depositional environments at a cm-m scale, and therefore can be used to understand short-term sedimentary processes in other lacustrine systems.

ACKNOWLEDGMENTS

We appreciate Drs. H. Lu, G.Y. Sheng, Z.W. Liao, Q.T. Wang, J. Liao, Y.K. Tian, T.L. Wang, and Y.J. Zhang of Guangzhou Institute of Geochemistry, Chinese Academy of Sciences for GC-MS facilities and Drs. D.J. Wronkiewicz, J. Obrist-Farner, and S. Gao of Missouri S&T for advices. Thanks to Drs. J. Wang, M.L. Wan, and S.W., Mei of Nanjing Institute of Geology and Paleontology, Chinese Academy of Sciences and Y.R. Lv, and J. Duan of Missouri S&T for field help. This research was partially supported by NSF GEOSCI [grant number 1714749] and NSF China [grant number 41428201] to Wan Yang, four student research grants from Geological Society of America, American Association of Petroleum Geologists, and State Key Laboratory of Organic Geochemistry, Chinese Academy of Sciences [grant number SKLOG-201603] to Xin Zhan, and NSF China [grant number 41428201] to Qiao Feng.

REFERENCES

- Bohacs, K.M., Carroll, A.R., Neal, J.E., and Mankiewicz, P.J., 2000. Lake basin type, source potential, and hydrocarbon character: An integrated sequence-stratigraphic-geochemical framework. In: Gierlowski-Kordesch, E.H. and Kelts, K.R. (Eds.), *Lake Basins through Space and Time*. American Association of Petroleum Geologists Studies in Geology 46, 3–34.

- Bourbonniere, R.A. and Meyers, P.A., 1996. Sedimentary geolipid records of historical changes in the watersheds and productivities of Lakes Ontario and Erie. *Limnology and Oceanography* 41, 352–359.
- Bradley, W.H., 1925. A contribution to the origin of the Green River Formation and its oil shale. *American Association of Petroleum Geologists Bulletin* 9, 247–262.
- Brassell, S.C., Eglinton, G., Sheng, G., and Fu, J.M., 1988. Biological markers in lacustrine Chinese oil shales. *Geological Society, London, Special Publications* 40, 299–308.
- Bray, E.E. and Evans, E.D., 1961. Distribution of n-paraffins as a clue to recognition of source beds. *Geochimica et Cosmochimica Acta* 22, 2–15.
- Bush, R. and McInerney, F.A., 2013. Leaf wax n-alkane distributions in and across modern plants: Implications for paleoecology and chemotaxonomy. *Geochimica et Cosmochimica Acta* 117, 161–179.
- Carroll, A.R. and Bohacs, K.M., 1999. Stratigraphic classification of ancient lakes: balancing tectonic and climatic controls. *Geology* 27, 99–102.
- Carroll, A.R. and Bohacs, K.M., 2001. Lake-type controls on petroleum source rock potential in nonmarine basins. *American Association of Petroleum Geologists Bulletin* 85, 1033–1053.
- Carroll, A.R., Brassell, S.C., and Graham, S.A., 1992. Upper Permian lacustrine oil shales, southern Junggar Basin, Northwest China. *American Association of Petroleum Geologists Bulletin* 76, 1874–1902.
- Carroll, A.R., Graham, S.A., and Hendrix, M.S., 1995. Late Paleozoic tectonic amalgamation of northwestern China: sedimentary record of the northern Tarim, northwestern Turpan, and southern Junggar basins. *Geological Society of America Bulletin* 107, 571–594.
- Carroll, A.R., 1998. Upper Permian lacustrine organic facies evolution, southern Junggar Basin, NW China. *Organic Geochemistry* 28, 649–667.
- Casagrande, D.L., Idowu, G., Friedman, A., Rickert, P., Siefert, K., and Schelnz, D., 1979. H₂S incorporation in coal precursors: origins of organic sulphur in coal. *Nature* 282, 599–600.
- Casagrande, D.L., Ng, L., 1979. Incorporation of elemental sulphur in coal as organic sulphur. *Nature* 282, 59–89.
- Chen, Z., Wu, N., Zhang, D., Hu, J., Huang, H., Shen, G., Wu, G., Tang, H., and Hu, Y., 1985. Geologic map of Xinjiang Uygur Autonomous Region, scale 1: 2,000,000. Beijing, Geologic Publishing House, 1 sheet.

- Cohen, K.M., Finney, S.C., Gibbard, P.L., and Fan, J.X., 2018. The ICS International Chronostratigraphic Chart. *Episodes* 36, 199–204.
- Craig, H., 1953. The geochemistry of the stable carbon isotopes. *Geochimica et Cosmochimica Acta* 3, 53–92.
- Craig, H., 1957. Isotopic standards for carbon and oxygen and correction factors for mass-spectrometric analysis of carbon dioxide. *Geochimica et Cosmochimica Acta* 12, 133–149.
- Cranwell, P.A., Eglinton, G., and Robinson N., 1987. Lipids of aquatic organisms as potential contributors to lacustrine sediments-II. *Organic Geochemistry* 11, 513–527.
- Curiale, J. and Lin R., 1991. Tertiary deltaic and lacustrine organic facies: comparison of biomarker and kerogen distributions. *Organic Geochemistry* 17, 785–803.
- Curiale, J.A., Cole, R.D., and Witmer, R.J., 1992. Application of organic geochemistry to sequence stratigraphic analysis: Four Corners Platform Area, New Mexico, U.S.A. *Advances in Organic Geochemistry* 19, 53–75.
- Derenne, S., Largeau, C., Casadevall, E., and Connan, J., 1988. Comparison of torbanites of various origins and evolutionary stages. Bacterial contribution to their formation. Cause of lack of botryococcane in bitumens. *Organic Geochemistry* 12, 43–59.
- Didyk, B.M., Simoneit, B.R.T., Brassell, S.C., and Eglinton, G., 1978. Organic geochemical indicators of palaeoenvironmental conditions of sedimentation. *Nature* 272, 216–222.
- Durand, B. and Nicaise, G., 1980. Procedures for kerogen isolation. In: Durand, B. (Ed.), *Kerogen-Insoluble Organic Matter from Sedimentary Rocks*. Editions Technip, Paris, pp. 35–53.
- Eglinton, G. and Hamilton, R.J., 1967. Leaf epicuticular waxes. *Science* 156, 1322–1335.
- Ficken, K.J., Li, B., Swain, D.L., and Eglinton, G., 2000. An n-alkane proxy for the sedimentary input of submerged/floating freshwater aquatic macrophytes. *Organic Geochemistry* 31, 745–749.
- Fu, J., Sheng, G., Peng, P., Brassell, S.C., Eglinton, G., and Jiang, J., 1986. Peculiarities of salt lake sediments as potential source rocks in China. *Organic Geochemistry* 10, 119–126.
- Fu, J., Sheng, G., Xu, J., Eglinton, G., Gowar, A.P., Jia, R., Fan, S., and Peng, P., 1990. Application of biological markers in the assessment of paleoenvironments of Chinese non-marine sediments. *Organic Geochemistry* 16, 769–779.

- Goossens, H., Duren, R.R., de Leeuw, J.W., and Schenck, P.A., 1989. Lipids and their mode of occurrence in bacteria and sediments-2. Lipids in the sediment of a stratified, freshwater lake. *Organic Geochemistry* 14, 27–41.
- Goad, L.J., Holz, G.G., and Beach, D.H., 1983. Identification of (24S)-24-methylcholesta-5, 22-dien-3 β -ol as the major sterol of a marine cryptophyte and a marine haptophyte. *Phytochemistry* 22, 475–476.
- Grice, K., Klein Breteler, W.C.M., Schouten, S., Grossi, V., de Leeuw, J.W., and Sinninghe Damsté, J.S., 1998. Effects of zooplankton herbivory on biomarker proxy records. *Paleoceanography* 13, 686–693.
- Hall, P.B. and Douglas, A.G., 1983. The distribution of cyclic alkanes in two lacustrine deposits. In: M. Bjorøy, and et al., (Eds.), *Advances in Organic Geochemistry*, New York, J. Wiley and Sons, pp. 576–587.
- Hanson, A.D., Zhang, S.C., Moldowan, J.M., Liang, D.G., and Zhang B.M., 2000. Molecular organic geochemistry of the Tarim Basin, Northwest China. *American Association of Petroleum Geologists Bulletin* 84, 1109–1128.
- Hanson, A.D., Ritts, B.D., Zinniker, D., Moldowan, J.M., and Biffi, U., 2001. Upper Oligocene lacustrine source rocks and petroleum systems of the northern Qaidam basin, northwest China. *American Association of Petroleum Geologists Bulletin* 85, 601–619.
- Horsfield, B., Curry, D.J., Bohacs, K., Littke, R., Rullkötter, J., Schenk, H.J., Radke, M., Schaefer, R.G., Carroll, A.R., Isaksen, G., and Witte, E.G., 1994. Organic geochemistry of freshwater and alkaline lacustrine sediments in the Green River Formation of the Washakie Basin, Wyoming, USA. *Organic Geochemistry* 22, 415–440.
- Huang, D.F., Li, J.C., and Zhang, D.J., 1990. Maturation sequence of continental crude oils in hydrocarbon basins in China and its significance. *Organic Geochemistry* 16, 521–529.
- Huang, W.Y. and Meinshein, W.G., 1979. Sterols as ecological indicators. *Geochimica et Cosmochimica Acta* 43, 739–45.
- Jeffery, B., 2010. Rift basin-fill architecture of fluvial-lacustrine lower Permian Lucaogou and Hongyanchi low-order cycles, Bogda Mountains, NW China. Unpublished Master. Wichita State University, pp. 115.
- Jones, R.W. and Demaison, G.J., 1982. Organic Facies - stratigraphic concepts and exploration tool. In: Saldivar-Sali, A. (Ed.), *Proceedings of the Second ASCOPE Conference and Exhibition*. Manila, Asean Council on Petroleum, pp. 51–68.

- Liao, Z., Lu, L., Jiang, N., Xia, F., Song, F., Zhou, Y., Li, S., and Zhang, Z., 1987. Carboniferous and Permian in the western part of the east Tianshan Mountains. Eleventh Congress of Carboniferous Stratigraphy and Geology, Guidebook Excursion 4. Beijing, China, pp. 50.
- Lu, H., Zhang, Y.J., Feng, Q., Ji, L.M., Zhang, M.Z., Peng, P.A., Sheng, G.Y., and Liu, D.H., 2018. Geochemical and petrographic evidence for the co-occurrence of races B and L of *Botryococcus braunii* in the Maoming oil shales, China. *Organic Geochemistry* 125, 14–23.
- Manzi, V., Roveri, M., Gennari, R., Bertini, A., Biffi, U., Giunta, S., Iaccarino, S.M., Lanci, L., Lugli, S., Negri, A., Riva, A., Rossi, M.E., and Taviani M., 2007. The deep-water counterpart of the Messinian Lower Evaporites in the Apennine foredeep: the Fanantello section (Northern Apennines, Italy). *Palaeogeography, Palaeoclimatology, Palaeoecology* 251, 470–499.
- Mello, M.R., Telnaes, N., Gaglianone, P.C., Chicarelli, M.I., Brassell, S.C., and Maxwell, J.R., 1988. Organic geochemical characterization of depositional paleoenvironments in Brazilian marginal basins. *Organic Geochemistry* 13, 31–46.
- Meyers, P.A. and Ishiwatari, R., 1993. Lacustrine organic geochemistry-an overview of indicators of organic matter sources and diagenesis in lake sediments. *Organic Geochemistry* 20, 867–900.
- Meyers, P.A., 1997. Organic geochemical proxies of paleoceanographic, paleolimnologic, and paleoclimatic processes. *Organic Geochemistry* 27, 213–250.
- Meyers, P.A., 2003. Applications of organic geochemistry to paleolimnological reconstructions: a summary of examples from the Laurentian Great Lakes. *Organic Geochemistry* 34, 261–289.
- Moldowan, J.M., Seifert, W.K., and Gallegos, E.J., 1985. Relationship between petroleum composition and depositional environment of petroleum source rocks. *American Association of Petroleum Geologists Bulletin* 69, 1255–1268.
- Moldowan, J.M., Sundararaman, P., and Schoell, M., 1986. Sensitivity of biomarker properties to depositional environment and/or source input in the Lower Toarcian of S. W. Germany. *Organic Geochemistry* 10, 915–926.
- Obrist-Farner, J. and Yang, W., 2016. Implications of loess and fluvial deposits on paleoclimatic conditions during an icehouse–hothouse transition, Capitanian upper Quanzijie low-order cycle, Bogda Mountains, NW China. *Palaeogeography, Palaeoclimatology, Palaeoecology* 441, 959–981.
- Obrist-Farner, J. and Yang, W., 2017. Provenance and depositional conditions of fluvial conglomerates and sandstones and their controlling processes in a rift setting, mid-Permian lower and upper Quanzijie low order cycles, Bogda Mountains, NW China. *Journal of Asian Earth Sciences* 138, 317–340.

- Ourisson, G., Albrecht, P., and Rohmer, M., 1979. The hopanoids: palaeo-chemistry and biochemistry of a group of natural products. *Pure and Applied Chemistry* 51, 709–729.
- Ourisson, G. and Albrecht, P., 1992. Hopanoids. 1. Geohopanoids: The Most Abundant Natural Products on Earth. *Accounts of Chemical Research* 25, 398–402.
- Peters, K.E. and Moldowan, J.M., 1991. Effects of source, thermal maturity, and biodegradation on the distribution and isomerization of homohopanes in petroleum. *Organic Geochemistry* 17, 47–61.
- Peters, K.E. and Moldowan, J.M., 1993. *The biomarker guide*, first ed.: Interpreting geochemical fossils in petroleum and ancient sediments, Prentice Hall, Englewood, Cliffs, New Jersey.
- Peters, K.E., Walter, M.M., and Moldowan, J.M., 2005. *The Biomarker Guide*, second ed.: Biomarkers and Isotopes in Petroleum Exploration and Earth History. Cambridge University Press, UK.
- Powell, T.G. and McKirdy, D.M., 1973. Relationship between ratio of pristane to phytane, crude oil composition and geological environment in Australia. *Nature*, 243, 37–39.
- Rieley, G., Collier, R.J., Jones, D.M., and Eglinton, G., 1991. The biogeochemistry of Ellesmere Lake, U. K. - I: Source correlation of leaf wax inputs to the sedimentary record. *Organic Chemistry* 17, 901–912.
- Ritts, B.D., Hanson, A.D., Zinniker, D., and Moldowan, J.M., 1999. Lower-Middle Jurassic nonmarine source rocks and petroleum systems of the northern Qaidam Basin, northwest China. *American Association of Petroleum Geologists Bulletin* 83, 1980–2005.
- Rohmer, M., Bissleret, P., and Neunlist, S., 1992. The hopanoids, prokaryotic triterpenoids and precursors of ubiquitous molecular fossils. In: Moldowan, J.M., Albrecht, P., Philp, R.P., (Eds.), *Biological Markers in Sediments and Petroleum: A Tribute to Wolfgang K. Seifert*. Prentice Hall, Englewood Cliffs, New Jersey, pp. 1–17.
- Rullkötter, J. and Marzi, R., 1988. Natural and artificial maturation of biological markers in a Toarcian shale from northern Germany. *Organic Geochemistry* 13, 639–45.
- Saltzman, M.R. and Thomas, E., 2012. Carbon Isotope Stratigraphy, in Gradstein, F.M., Ogg, J.G., Schmitz, M.D., Ogg, G.M., eds., *The Geological Time Scale 2012*: Oxford Press, UK, 1139 p.

- Sachsenhofer, R.F., Bechtel, A., Kuffner, T., Rainer, T., Gratzer, R., Sauer, R., and Sperl, H., 2006. Depositional environment and source potential of Jurassic coal-bearing sediments (Gresten Formation; Höflein gas/condensate field; Austria). *Petroleum Geoscience* 12, 99–114.
- Scalan, R.S. and Smith, J.E., 1970. An improved measure of the odd-to-even predominance in the normal alkanes of sediment extracts and petroleum. *Geochimica et Cosmochimica Acta* 34, 611–620.
- Scotese, C.R., 2014. Atlas of Permo-Carboniferous Paleogeographic Maps (Mollweide Projection), Maps 53-64. PALEOMAP PaleoAtlas for ArcGIS The Late Paleozoic, v. 4. PALEOMAP Project, Evanston, IL.
- Seifert, W.K. and Moldowan, J.M., 1978. Applications of steranes, terpanes and monoaromatics to the maturation, migration and source of crude oils. *Geochimica et Cosmochimica Acta* 42, 77–95.
- Seifert, W.K. and Moldowan, J.M., 1986. Use of biological markers in petroleum exploration. In: Johns, R.B., (Ed.), *Methods in Geochemistry and Geophysics*, v. 24. Elsevier, Amsterdam, pp. 261–290.
- Sepúlveda, J., Wendler, J., Leiderb, A., and Kuss, H.J., Summons, R.E., Hinrichs, K.U., 2009. Molecular isotopic evidence of environmental and ecological changes across the Cenomanian–Turonian boundary in the Levant Platform of central Jordan. *Organic Geochemistry* 40, 553–568.
- Sinninghe Damsté, J.S., Kenig, F., Koopmans, M.P., Köster, J., Schouten, S., Hayes, J.M., and de Leeuw, J.W., 1995. Evidence for gammacerane as an indicator of water-column stratification. *Geochimica et Cosmochimica Acta* 59, 1895–1900.
- Slatt, R.M. and Rodriguez, N.D., 2012. Comparative sequence stratigraphy and organic geochemistry of gas shale: Commonality or coincidence? *Journal of Natural Gas Science and Engineering* 8, 68–84.
- Ten Haven, H.L., de Leeuw, J.W., Rullkötter, J., and Sinninghe Damsté, J.S., 1987. Restricted utility of the pristane/phytane ratio as a palaeoenvironmental indicator. *Nature* 330, 641–643.
- Tissot, B.P. and Welte, D.H., 1984. *Petroleum Formation and Occurrence: A New Approach to Oil and Gas Exploration*. Springer-Verlag, New York.
- Trask, P.O., 1939. Organic content of recent marine sediments. In: Trask, P.O. (Ed.), *Recent Marine Sediments*. American Association of Petroleum Geologists, Tulsa.
- Tyson, R.V., 1995. *Sedimentary Organic Matter*, first ed. Chapman and Hall, London.

- Van Kaam-Peters, H.M.E., Koster, J., Van Der Gaast, S.J., Dekker, M., De Leeuw, J.W., and Sinninghe Damsté, J.S., 1998. The effect of clay minerals on diasterane/sterane ratios. *Geochimica et Cosmochimica Acta* 62, 2923–2929.
- Volkman, J.K. and Maxwell, J.R., 1986. Acyclic isoprenoids as biological markers. In: Johns, R.B. (Ed.), *Biological Markers in the Sedimentary Record*. Elsevier, Amsterdam, pp. 1–42.
- Volkman, J.K., 1986. A review of sterol markers for marine and terrigenous organic matter. *Organic Geochemistry* 9, 83–99.
- Volkman, J.K., 1988. Biological marker compounds as indicators of the depositional environments of petroleum source rocks. In: Fleet, A.J., Kelts, K., Talbot, M.R. (Eds.), *Lacustrine Petroleum Source Rocks*. Blackwell, London, pp. 103–122.
- Volkman, J.K., 2003. Sterols in microorganisms. *Applied Microbiology and Biotechnology* 60, 495–506.
- Volkman, J.K., 2005. Sterols and other triterpenoids: source specificity and evolution of biosynthetic pathways. *Organic Geochemistry* 36, 139–159.
- XBGMR (Xinjiang Bureau of Geology and Mineral Resources), 1993. *Regional Geology of Xinjiang Uygur Autonomous Region, Geological Memoirs, Series 1, No. 32*. Geological Publishing House, Ministry of Geology and Mineral Resources of China, Beijing (in Chinese).
- Yang, W., Liu, Y., Feng, Q., Lin, J., Zhou, D., and Wang, D., 2007. Sedimentary evidence of Early-Late Permian mid-latitude continental climate variability, southern Bogda Mountains, NW China. *Palaeogeography, Palaeoclimatology, Palaeoecology* 252, 239–258.
- Yang, W., Feng, Q., Liu, Y., Tabor, N., Miggins, D., Crowley, J.L., Lin, J., and Thomas, S., 2010. Depositional environments and cyclo- and chronostratigraphy of uppermost Carboniferous-Lower Triassic fluvial-lacustrine deposits, southern Bogda Mountains, NW China - A terrestrial paleoclimatic record of mid-latitude NE Pangea. *Global and Planetary Change* 73, 15–113.
- Yang, W., 2008. Depositional systems analysis within a seismic sequence stratigraphic framework, Turpan–Hami basin. Internal Report. Tu-Ha Petroleum Bureau, NW China, PetroChina, pp. 49 (in Chinese).
- Zhang, X., 1981. *Regional Stratigraphic Chart of northwestern China, Branch of Xinjiang Uygur Autonomous Region*. Geological Publishing House, Beijing, pp. 496 (in Chinese).

II. ENHANCED ARIDITY AND SEASONALITY OF MID-LATITUDE NORTHEAST PANGAEA INDUCED BY LATE PALEOZOIC DEGLACIATION

Contributing Authors: Xin Zhan^{1,†}, Wan Yang^{1,†}, Yujiao Zhang^{2,3}, Qiao Feng⁴

Author Affiliations:

¹ Geology and Geophysics Program, Missouri University of Science and Technology, 1400 N. Bishop, Rolla, MO 65409, U.S.A.

² State Key Laboratory of Organic Geochemistry, Guangzhou Institute of Geochemistry, Chinese Academy of Sciences, 511 Kehua Street, Guangzhou 510640, China

³ University of the Chinese Academy of Sciences, 19 Yuquan Road, Beijing 100049, China

⁴ Shandong Provincial Key Laboratory of Depositional Mineralization and Sedimentary Minerals, Shandong University of Science and Technology, 579 Qianwangang Road, Qingdao 266000, China

[†] Correspondence and requests for materials should be addressed to xz793@mst.edu and yangwa@mst.edu

ABSTRACT

Paleoclimate of low- and mid-latitude Pangea changed dramatically from humid to arid during the late Paleozoic ice age. Relationship between climate of paleo-tropics and glacial cyclicity in Southern Hemisphere has been suggested, however, linkage between climate of mid-latitude North Hemisphere and Gondwanan glacial cyclicity has been unresolved. Hereby we investigate climate of southeastern Kazakhstan mid-latitude northeast Pangea and its linkage with Gondwanan glaciation in early Permian. High organic carbon isotopic values ($\delta^{13}\text{C}_{\text{org}}$) of lower Lucaogou and Hongyanchi deposits in Bogda area, NW China are consistent with low atmospheric pCO_2 during retreat and waxing stages of Gondwanan glaciation in early Sakmarian and Artinskian–early Kungurian, respectively, whereas low $\delta^{13}\text{C}_{\text{org}}$ values of middle-upper Lucaogou deposits are coherent with high atmospheric pCO_2 during interglaciation in mid-late Sakmarian. A humid and seasonal climate is suggested by a mixture of laminated shales and massive mudstones, varves with dropstones, and low gammacerane index, corresponding to Gondwanan glaciation retreat in early Sakmarian. Enhanced aridity and seasonality are evidenced by dominance of laminated shales, varved deposits, and high gammacerane index, coinciding with interglacial during mid-late Sakmarian. Increased humidity and seasonal stability are indicated by dominance of massive and bioturbated siltstones and low gammacerane index, accompanying with regional glaciation in eastern Gondwana during Artinskian–early Kungurian. The climatic changes in southeastern Kazakhstan mid-latitude northeast Pangea are largely correlated with that in low-latitude eastern Pangea and North China and synchronous with Gondwanan glacial cycles, suggesting

that waxing and waning of ice sheets in Southern Hemisphere may have played a significant role in climatic changes of Northern Hemisphere.

1. INTRODUCTION

The late Paleozoic ice age (LPIA: 320–260 Myr ago) is one of the most important climatic events on the Earth as it witnessed the most widespread, longest glaciation, and dynamic glacial cyclicity during the Phanerozoic, coinciding with collision of Gondwana and Laurasia to create Pangea (Frakes and Crowell, 1967; Crowell, 1978; Eyles, 1993; Isbell et al., 2003a, 2003b, 2012; Fielding et al., 2008a, 2008b, 2008c; Gulbranson et al., 2010). The icehouse-to-greenhouse transition on vegetated Earth during the LPIA is the only record documented in geological history, which may provide profound implication for prediction of climatic change in recent global warming.

A better understanding of the dynamic LPIA requires an accurate reconstruction of eustasy, paleogeography, paleoclimate, and distribution and evolution of Gondwanan ice sheets during the Carboniferous and Permian (Crowell, 1978; Heckel, 1986, 2008; Rygel et al., 2008; Fielding et al., 2008a). However, uncertainty remains over the timing, duration, extent, depositional settings, and driving forces of these glaciation, as well as their feedbacks, especially temporal synchronicity between the glacial episodes in South Hemisphere and cyclothems in the Northern Hemisphere (Isbell et al., 2003b, 2008, 2016; Fielding et al., 2008c; Stemmerick, 2008; Lopez-Gamundi and Buatois, 2010; Montañez and Poulsen, 2013). Most of the studies have been conducted on climatic changes of paleo-tropics and subtropical, whereas the relationship between paleoclimatic

changes across mid-latitude North Hemisphere and Gondwanan glacial cyclicity remains enigmatic. In this study, precipitation and seasonality of southeastern Kazakhstan at the mid-latitude northeast Pangea were interpreted from sedimentary features and biomarker proxies of lower Permian Lucaogou and Hongyanchi Formations in Bogda area, NW China. The records in Bogda were compared with that in other basin in low- and mid-latitude of Pangea and North China in order to investigate the linkage between climate changes in low- and mid-latitude of Northern Hemisphere and Gondwanan glacial–interglacial cycles from early Sakmarian to early Kungurian.

2. GEOLOGICAL SETTINGS

The Lucaogou and Hongyanchi low-order cycle (LC; Yang et al., 2010) of this study are exposed in the Tarlong-Taodonggou and Zhaobishan area at the southern foothills of Bogda Mountains, Xinjiang Uygur Autonomous Region, Northwestern China (Figure 1A). The Bogda Mountains are a giant anticline, contain Devonian to Quaternary sedimentary and igneous rocks (Zhang, 1981; Yang et al., 2010). Uppermost Carboniferous-Lower Triassic fluvial-lacustrine deposits are exposed as folded strata in Tarlong, Taodonggou, and Zhaobishan areas. (Figure 1B, C; Chen et al., 1985; Carroll et al., 1995; Yang et al., 2010; Obrist and Yang, 2016; Fredericks, 2016). The strata in Tarlong-Taodonggou area were interpreted as alluvial, fluvial, and lacustrine deposits in a half graben on the basis of the rapid lateral facies and thickness changes in the area with reference to the stratal and basin geometries on seismic sections in nearby Turpan-Hami Basin (Yang, 2008; Yang et al., 2010; Obrist and Yang, 2016). Recent plate-tectonic and

paleogeographic reconstruction places the Bogda area in southeastern Kazakhstan Plate, mid-latitude northeastern Pangea (Figure 1D; modified from Scotese, 2014).

Low-order cycle (LC) is an informal cyclostratigraphic unit defined by Yang et al. (2007; 2010) on the basis of long-term trends of depositional environments and tectonic and/or climatic conditions. Lucaogou and Hongyanchi LCs are largely correlated with the Lucaogou and Hongyanchi formations, respectively. Lucaogou LC overlies upper Daheyan LC and underlies Hongyanchi LC, which is underlain by Quanzijie LC with an unconformity encompassing maximum of ~ 14 Ma (Yang et al., 2010; Obrist and Yang, 2016). The age of Lucaogou and Hongyanchi LC is estimated as Sakmarian and Artinskian-early Kungurian, respectively, as poorly constrained by U/Pb zircon ages of 301.26 ± 0.05 Ma from ash-fall tuff in the uppermost lower Daheyan LC and 281.42 ± 0.10 Ma from ash-fall tuff ~30 m below Hongyanchi-Quanzijie unconformity in south Tarlong (Figure 2A; Yang et al., 2010; Obrist and Yang, 2016). Lucaogou LC contains mainly fluctuating profundal deposits intercalated with lakeplain-littoral and lacustrine deltaic deposits while Hongyanchi LC consists of a mixture of lacustrine deltaic, fluctuating profundal, and meandering and braided stream deposits (Figure 2A; Yang et al., 2010). Cyclic deposits in Lucaogou and Hongyanchi LCs reflect repetitive changes of fluvial and lacustrine environments during lake contraction and expansion (Figure 2A; Yang et al., 2010). The paleoclimate of north Tarlong fluctuated between subhumid to semiarid in Lucaogou time, whereas mainly humid in early Hongyanchi time, fluctuated between subhumid and humid in middle-late Hongyanchi time, and gradually changed from subhumid to semiarid at the end of Hongyanchi time, as indicated by sedimentary evidences (Yang et al., 2007; 2010).

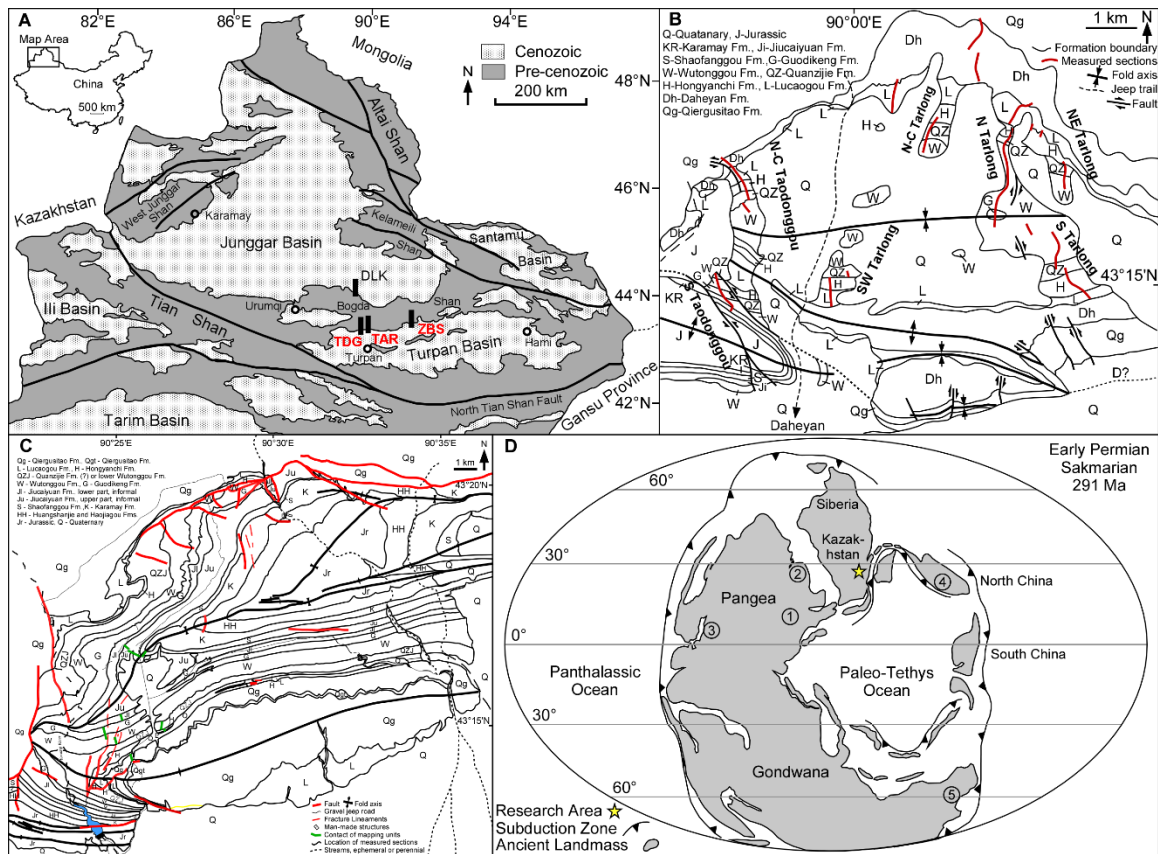


Figure 1. (A) Geological map of the study area. It shows Turpan-Hami Basin, Junggar Basin, Santanhu Basin, Bogda Mountains, and Tianshan in Xinjiang Uygur Autonomous Region, NW China. Black boxes show the location of Tarlong (TAR), Taodonggou (TDG), and Zhaobishan (ZBS) sections. Modified from Chen et al. (1985) and Yang et al. (2010). (B) Geological maps of Tarlong-Taodonggou area. Modified from Yang et al. (2010) and Obrist-Farner and Yang (2016). (C) Geological maps of Zhaobishan. Modified from Fredericks, 2016. (D) Paleotectonic and paleogeographic reconstruction of Pangea and Gondwana at early Permian (291 Ma), showing the study area in the southeast Kazakhstan Plate at mid-latitude NE Pangea and location of ① Lodève Basin, France, ② Western Urals, Russia, ③ Kansas, U.S. Midcontinent, ④ Yongcheng Basin, North China, and ⑤ Queensland, Australia (Ziegler et al., 1997; Scotese, 2014).

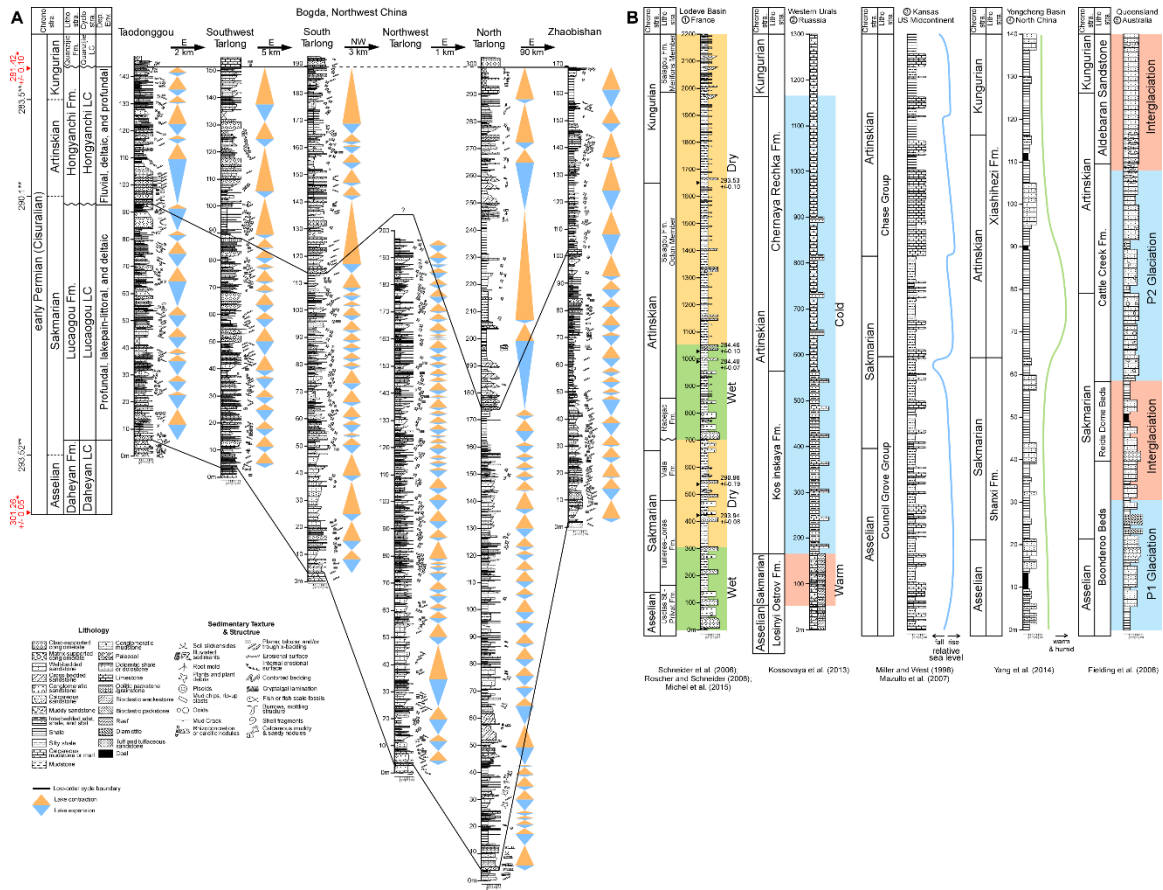


Figure 2. Lithological columns. It shows lower Permian strata in Bogda, northwest China, in comparison with terrestrial and marine deposits of the same interval in low-, mid-, and high-latitude. Correlation of Lucaogou and Hongyanchi low-order cycles in Taodonggou, south, southwest, northwest, and north Tarlong, and Zhaobishan sections is on the basis of Yang et al. (2010) and unpublished data of Wan Yang. High-precision U/Pb zircon ID-TIMS ages (*) in Bogda are from Yang et al. (2010) and Obrist-Farner and Yang (2016). Absolute ages (**) at stage boundaries of international time scale are from Cohen et al. (2018). Black thick lines mark low-order cycle boundaries. Orange and blue triangles represent interpreted lake contraction and expansion, respectively, modified from Yang et al. (2009). Cyclothems and interpreted climate or relative sea level in ①Lodève Basin, France are modified from Schneider et al. (2006), Roscher and Scheider (2006), and Michel et al. (2015), ②Western Urals, Russia, modified from Kossovaya et al. (2013), ③Kansas, U.S. Midcontinent, modified from Miller and West (1998) and Mazullo et al. (2007), ④Yongcheng Basin, North China, modified from Yang et al. (2014), and ⑤Queenslan, Australia, modified from Fielding et al. (2008b).

3. METHODOLOGY AND DATA

Petrographic and geochemical studies of lacustrine deposits were carried out to interpret precipitation and seasonality in terms of physical and chemical conditions of lake water. 103 Lucaogou organic-rich shales, dolomitic shales, calcareous shales, siltstones, sandstones, conglomerates, and limestone and 46 Hongyanchi organic-rich shales, dolomitic shales, calcareous shales, and siltstones in Taodonggou, northern, southern, northwest, and southwest Tarlong, and Zhaobishan sections were collected for petrographic and geochemical analyses (Tables S1–S6). Care was taken to select samples that are at least 30 cm beneath surface and have no signs of surface weathering and alteration. Petrographic observations of 89 Lucaogou and 46 Hongyanchi samples were carried out using stereo- and polarizing microscope, respectively. Geochemical analyses of 80 Lucaogou and 36 Hongyanchi samples were conducted in Guangzhou Institute of Geochemistry, Chinese Academy of Sciences.

Content of total organic carbon (TOC) was obtained with a Leco SC-632 carbon analyzer through combustion of organic carbon to CO₂. 60–120 mg of samples were first decontaminated through sonication using deionized water and oven dried at 40 °C. Samples were then powdered to a 100-mesh size (<0.15 mm) and soaked in excess 10% hydrochloric acid and kept at 40 °C for one day to remove inorganic carbonate material. After washed with deionized water until neutral, the samples were dried in the oven at 40 °C for one day before measurement. The combustion oven temperature was held at 400 °C for 3 minutes and heated to 850 °C for 5 minutes at a rate of 25 °C/min. Precision of duplicate samples and detection limit are $\pm 0.025\%$ and 0.005% for TOC, respectively.

Kerogen extraction was done first by pretreating 10–20 g of each sample with 38% hydrochloric and 30% hydrofluoric acid to remove all inorganic carbonate and siliciclastic components, respectively, following processes of Durand and Nicaise (1980). Kerogen was extracted as the acid-insoluble residues after centrifuged and washed with deionized water until neutral. Proportions of carbon (C) and nitrogen (N) content in kerogen were measured using the combustion method via an Elemental Analyzer (Model: Vario Macro Cube, Elementar, Germany) after Prahl et al. (1980). Stable organic isotopic composition ($\delta^{13}\text{C}_{\text{org}}$) was measured using combustion system with a coupled elemental analyzer and isotope ratio mass spectrometer (Model: ThermoFinnigan Delta XL Plus GC-IRMS). Kerogen for each sample was weighed based on the proportion of organic carbon content in kerogen, and 20–80 μg of kerogen were added to a stannum boat and combusted at 1800 °C under helium carrier gas, following Craig (1953). Isotope ratios are determined based on delta notation (‰) relative to the Vienna Pee Dee Belemnite (V-PDB) standard after Craig (1957). Precision and accuracy were monitored through analysis of two powdered standards every twenty running of kerogen samples. Measured precision of $\delta^{13}\text{C}_{\text{org}}$ was maintained at $\pm 0.08\text{‰}$ for replicated samples.

Biomarker analysis of extracted organic matter from each sample was conducted using Gas Chromatography (GC) and Gas Chromatography-Mass Spectrometry (GC-MS). Organic matter was extracted from 80–120 g of each crushed samples using a solvent mixture of dichloromethane and methanol of a 9:1 at 48 °C for 72 hours. After evaporative removal of extraction solvent, the extracts were dissolved in hexane and centrifuged to remove asphaltenes. Maltene was fractionated through column chromatography using activated thin layer alumina and silica gel. Aliphatic, aromatic and

polar fractions were separated using hexane, a mixture of hexane and dichloromethane at a 3:2, and methanol, respectively. Saturated fraction was analyzed using Agilent 7890A GC and Thermo Trace GC Ultra/DSQII GC-MS following the same heating procedure. Helium (400–700 kPa) was used as carrier gas at a flow rate of 1.0 ml/min. GC was coupled with a 5975C MSD instrument and Triple-Axis Detector, using a HP-5 fused silica capillary column with a size of 30 m × 0.25 mm i.d. and 0.25 μm film thickness. Samples were injected in a splitless mode with the detector temperature at 260 °C. The oven temperature was set initially at 80 °C and held for 2 min, then increased to 300 °C at a heating rate of 4 °C/min and held for 25 min. The spectrometer of GC-MS was operated in the electron ionization (EI) mode at 70 eV. The MS full scan ranges from m/z 50 to 650 with a 0.5 s total scan time and selected ion monitoring (SIM) are m/z = 78, 123, 191, 217, 231 for saturate fractions. Identification of individual compounds was achieved by comparing mass spectra and fragmentation patterns with literature and authentic standards (Peters et al., 2005) using Chemstation software and Xcalibur software from Finnigan. Values of biomarker parameters were calculated based on integrated peak area of relative intensity.

4. RESULTS

4.1. SEDIMENTARY CHARACTERISTICS OF LUCAOGOU AND HONGYANCHI MUDSTONES

Heterogeneous laminated shales (62 out of 78 mudstones) dominate in entire Lucaogou low-order cycle (LC) in all the sections and varves with dropstone (2 out of 7 varves) are restricted in basal Lucaogou LC in northern and northwest Tarlong sections,

whereas homogenous massive and bioturbated mudstones (42 out of 46 mudstones) prevail in the entire Hongyanchi LC in all the sections (Figure 3A). Lucaogou shales are black to blackish gray, thin to thick platy, mm- to sub-mm-laminated (Figure 4; Tables S1–S6). Laminations are mainly parallel to wavy, with a few others are algal-laminated, cross-bedded, lenticular, climbing rippled, and rarely massive. Lucaogou shales are mainly organic-rich and variably calcareous or dolomitic. They contain common to abundant plant remains and amorphous organic matter, with a few ostracods, fish scale, and rare benthic fossils and burrows. Hongyanchi siltstones are mainly dark gray and greenish to yellowish gray, principally massive, sparsely to moderately bioturbated, and rarely laminated (Figure 5; Tables S1–S6). Hongyanchi siltstones are predominantly organic-rich and rarely calcareous or dolomitic. They have common plant remains, amorphous organic matter, burrows, fish scale, and sparse ostracods.

Fine- and coarse-grained sediment couplet are confined to lower and middle Lucaogou LC and they are absent in Hongyanchi LC. The thin-section images of LCG shales show sediment couplet comprise paired contrasting laminations of lighter layers of coarser silt-fine sand and darker layers of clay (Figure 4I-L) and paired contrasting laminations of lighter layers of clay and darker layers of coarser silt-fine sand with organic matter (Figure 4M-N). Two thin-section images of basal Lucaogou varves in north and northwest Tarlong show two coarse-sand-sized clasts rupture underlying sub-mm laminated organic-rich laminae and are covered conformably by organic-rich laminae (Figure 4M–N). The mineral composition of the clasts is unidentified.

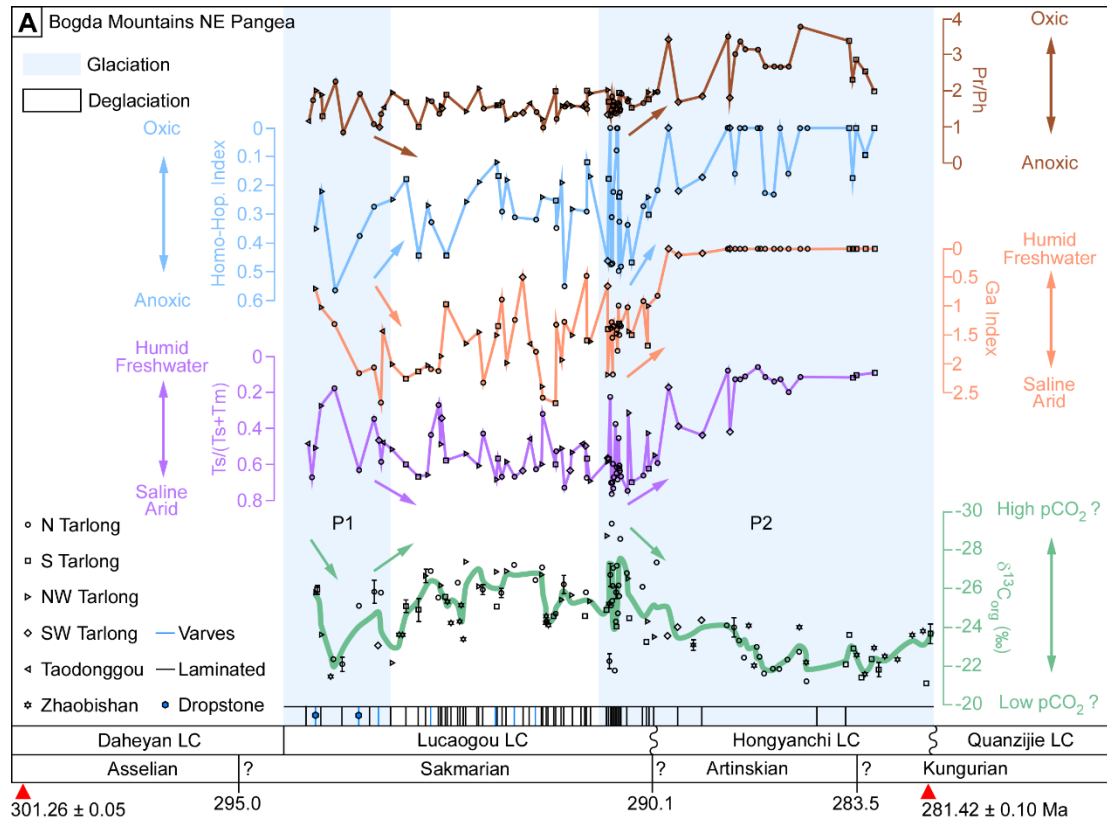


Figure 3. Correlation of Asselian–Kungurian climate in north hemisphere, equator, and south hemisphere. (A) Redox condition, precipitation, and seasonality of southeastern Kazakhstan mid-latitude northeast Pangea during early Sakmarian–early Kungurian. Geochemical and sedimentary proxies are plotted on a depth scale with thickness of Lucaogou and Hongyanchi LCs in all the sections normalized to that in north Tarlong. Stages are estimated based on correlation of 3-point moving average of $\delta^{13}\text{C}_{\text{org}}$ values (green curve) of 101 lacustrine shales and siltstones in Taodonggou, north, south, southwest, and northwest Tarlong, and Zhaobishan sections with $\delta^{13}\text{C}_{\text{carb}}$ value in western paleoequatorial Euramerica and south China (black dots in (B); Saltzman and Thomas, 2012), with constraint of absolute geochronologic ages of 281.42 ± 0.10 Ma in the uppermost Hongyanchi LC and 301.26 ± 0.05 Ma in the uppermost lower Daheyan LC (Yang et al., 2010). High $\delta^{13}\text{C}_{\text{org}}$ values are consistent with low atmospheric CO_2 during waxing stages of glacial P1 in early Sakmarian and glacial P2 in Artinskian–early Kungurian, whereas low $\delta^{13}\text{C}_{\text{org}}$ values are coincided with high atmospheric CO_2 during waning stages of interglacial between P1 and P2 in mid-late Sakmarian. Redox condition of water body is reconstructed from Pr/Ph (brown curve) and homohopane index (blue curve). Precipitation is reconstructed on basis of gammacerane index (orange curve) and Ts/(Ts+Tm) (purple curve). Seasonality is reconstructed based on laminated shales, varved deposits, and dropstone. An overall trend of enhanced aridity and seasonality coincide with deglaciation in mid-late Sakmarian and reduced aridity and seasonality coincided with the glaciation in Artinskian–early Kungurian. (B) Relationship between Asselian–Kungurian pCO₂ and climate in paleoequatorial western Euramerica (Montañez et al., 2007). Temporal distribution of glaciation and deglaciation is constructed on basis of stratigraphic distribution of diamictites, rhythmites, dropstones, and keel turbate structures in Antarctica and Australian (Jones and Fielding, 2004). Inferred paleotropical sea-surface temperatures (SSTs, orange interval) are reported as temperature anomalies relative to 17.5 °C estimated from $\delta^{18}\text{O}$ of brachiopod (Montañez et al., 2007). The atmospheric pCO₂ (red curve) is estimated from inorganic $\delta^{13}\text{C}$ of pedogenic carbonate and organic carbon isotopic value ($\delta^{13}\text{C}_{\text{org}}$) of fossil plant matter using Monte Carlo simulation (Montañez et al., 2007).

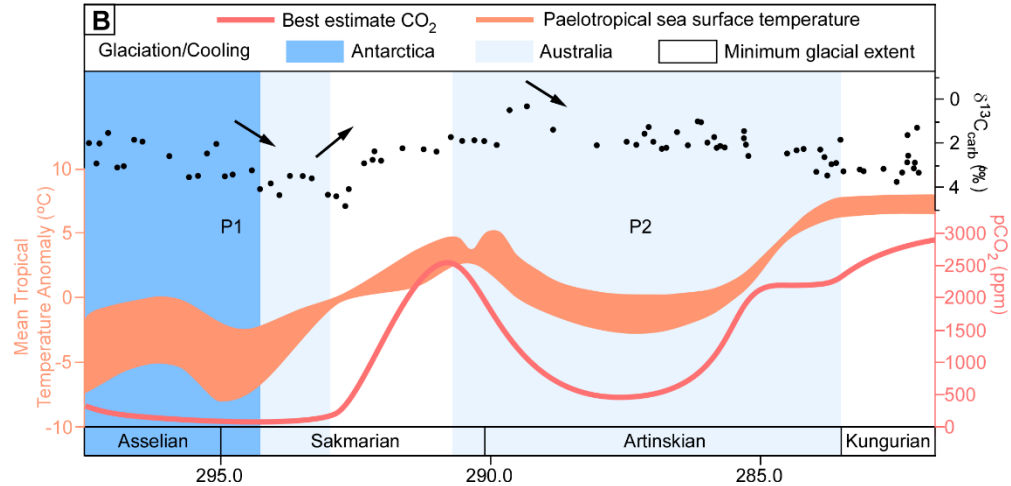


Figure 3. Correlation of Asselian–Kungurian climate in north hemisphere, equator, and south hemisphere. (A) Redox condition, precipitation, and seasonality of southeastern Kazakhstan mid-latitude northeast Pangea during early Sakmarian–early Kungurian. Geochemical and sedimentary proxies are plotted on a depth scale with thickness of Lucaogou and Hongyanchi LCs in all the sections normalized to that in north Tarlong. Stages are estimated based on correlation of 3-point moving average of $\delta^{13}\text{C}_{\text{org}}$ values (green curve) of 101 lacustrine shales and siltstones in Taodonggou, north, south, southwest, and northwest Tarlong, and Zhaobishan sections with $\delta^{13}\text{C}_{\text{carb}}$ value in western paleoequatorial Euramerica and south China (black dots in (B); Saltzman and Thomas, 2012), with constraint of absolute geochronologic ages of 281.42 ± 0.10 Ma in the uppermost Hongyanchi LC and 301.26 ± 0.05 Ma in the uppermost lower Daheyan LC (Yang et al., 2010). High $\delta^{13}\text{C}_{\text{org}}$ values are consistent with low atmospheric CO_2 during waxing stages of glacial P1 in early Sakmarian and glacial P2 in Artinskian–early Kungurian, whereas low $\delta^{13}\text{C}_{\text{org}}$ values are coincided with high atmospheric CO_2 during waning stages of interglacial between P1 and P2 in mid-late Sakmarian. Redox condition of water body is reconstructed from Pr/Ph (brown curve) and homohopane index (blue curve). Precipitation is reconstructed on basis of gammacerane index (orange curve) and $\text{Ts}/(\text{Ts}+\text{Tm})$ (purple curve). Seasonality is reconstructed based on laminated shales, varved deposits, and dropstone. An overall trend of enhanced aridity and seasonality coincide with deglaciation in mid-late Sakmarian and reduced aridity and seasonality coincided with the glaciation in Artinskian–early Kungurian. (B) Relationship between Asselian–Kungurian pCO_2 and climate in paleoequatorial western Euramerica (Montañez et al., 2007). Temporal distribution of glaciation and deglaciation is constructed on basis of stratigraphic distribution of diamictites, rhythmites, dropstones, and keel turbate structures in Antarctica and Australian (Jones and Fielding, 2004). Inferred paleotropical sea-surface temperatures (SSTs, orange interval) are reported as temperature anomalies relative to 17.5°C estimated from $\delta^{18}\text{O}$ of brachiopod (Montañez et al., 2007). The atmospheric pCO_2 (red curve) is estimated from inorganic $\delta^{13}\text{C}$ of pedogenic carbonate and organic carbon isotopic value ($\delta^{13}\text{C}_{\text{org}}$) of fossil plant matter using Monte Carlo simulation (Montañez et al., 2007). (cont.)

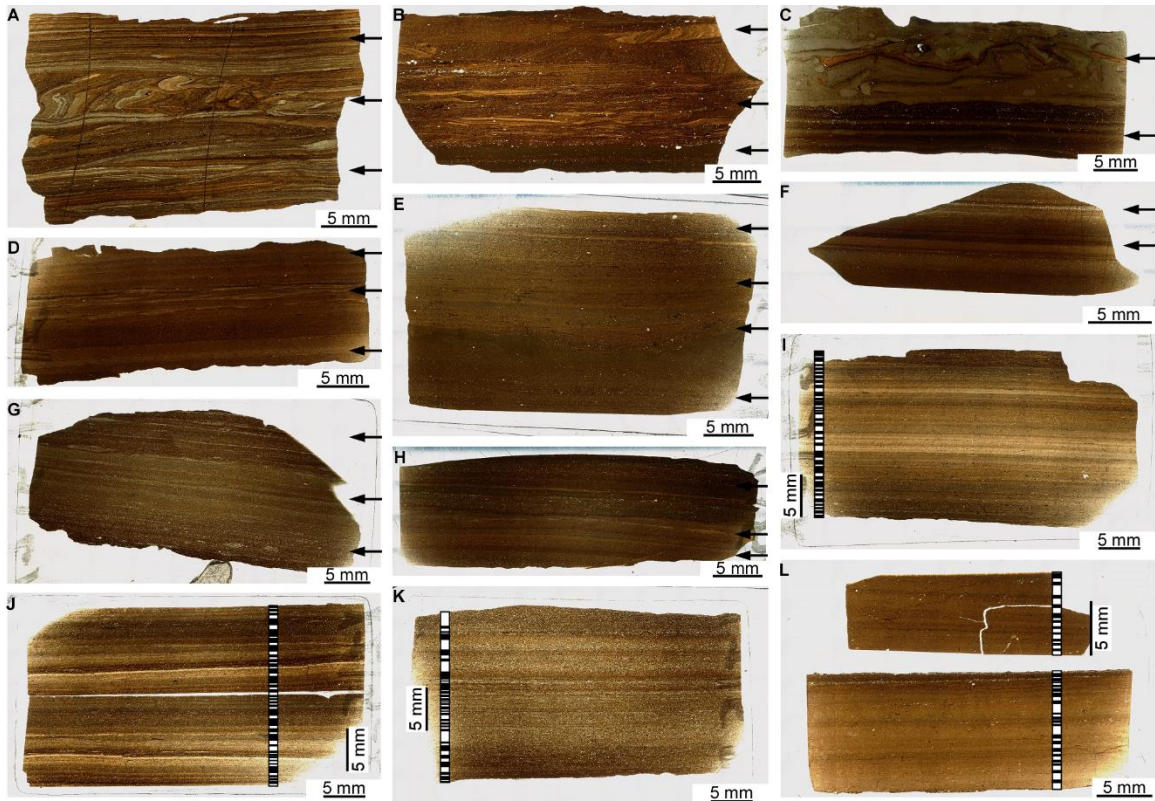


Figure 4. Photomicrographs of Lucaogou shale thin-sections in plain light, showing heterogeneous laminae. (A) lower part is mm-laminated, low-angle cross-laminated, non-parallel, and discontinuous; middle part is contorted, folded; upper part is mm-laminated, planar, parallel, and continuous; (B) lower part is mm-laminated, planar, parallel, continuous, and organic-rich; middle part is sub-mm-laminated, wavy, parallel, and discontinuous; upper part is contorted; (C) lower part is mm-laminated, planar, parallel, and continuous; upper part is organic-rich and lenticular-laminated with undulating micro-faults and mud clasts; (D) lower part is mm-laminated, planar, parallel, and continuous; middle part is lenticular-laminated, wavy, and discontinuous; upper part is sub-mm-laminated, planar, parallel, and continuous; (E) lower part is sub-mm-laminated, planar, parallel, and continuous; middle lower part is curved, parallel, and continuous, with erosional surface; middle upper part is wavy, nonparallel, and continuous; upper part is sub-mm-laminated, planar, nonparallel, and discontinuous; (F) lower and middle parts are sub-mm-laminated, planar, well parallel, and continuous; upper part is planar, parallel or nonparallel, and discontinuous; (G) lower part is sub-mm-laminated, planar, parallel, and continuous; middle part is mm-laminated, wavy, parallel, and continuous; upper part is lenticular and sub-mm-laminated, planar, parallel, and discontinuous; (H) lower part is sub-mm-laminated, planar, parallel, and continuous; middle part is lenticular-laminated, nonparallel, discontinuous, and erosional; upper part is sub-mm-laminated, planar, parallel, and discontinuous; (I–L) sub-mm laminated, planar, well parallel, and continuous sediment couplets; the black and white bars on the left or right of the images show paired contrasting laminations of lighter layers of coarser silt and darker layers finer clay, suggesting alternating sedimentation; (M–N) sub-mm laminated, planar, well parallel, and continuous couplets; the black and white bars corresponding to paired laminations of darker layers of coarser silt-fine sand with organic matter and lighter layers of clay; two clasts rupture underlying sub-mm laminated organic-rich laminae in the sediment couplets and are covered conformably by organic-rich laminae, suggesting that the clasts are extraclasts not being transported by bedload and interpreted as dropstones.

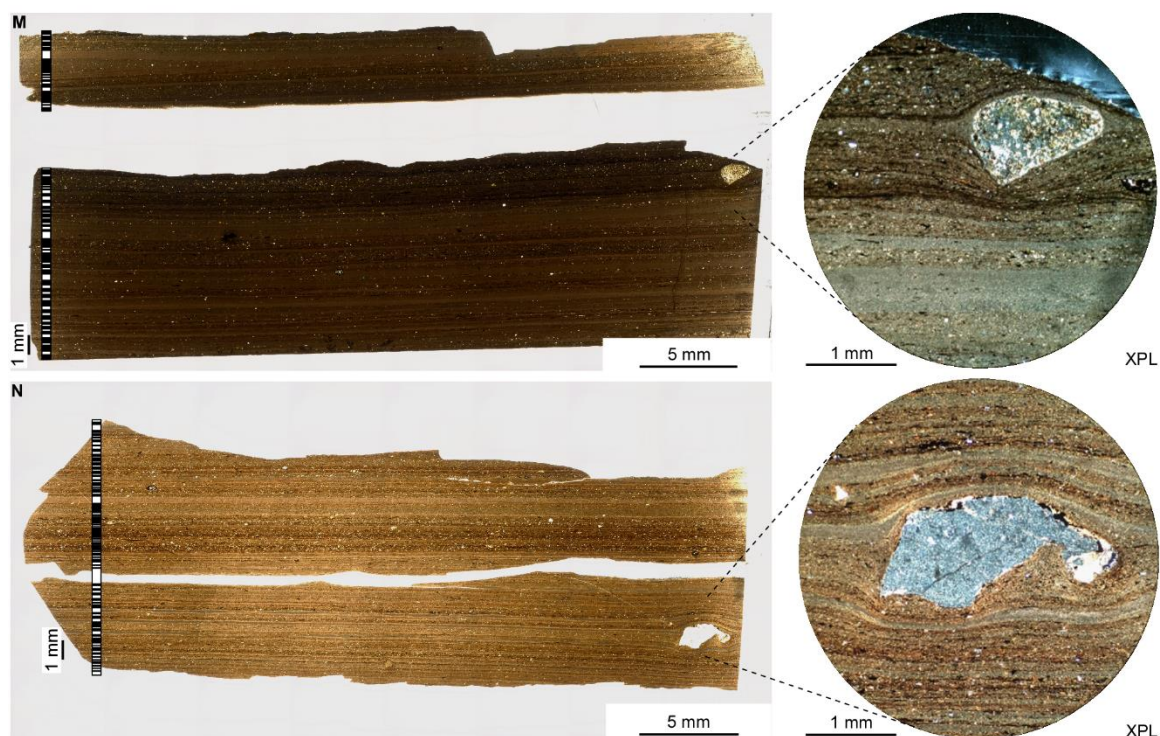


Figure 4. Photomicrographs of Lucaogou shale thin-sections in plain light, showing heterogeneous laminae. (A) lower part is mm-laminated, low-angle cross-laminated, non-parallel, and discontinuous; middle part is contorted, folded; upper part is mm-laminated, planar, parallel, and continuous; (B) lower part is mm-laminated, planar, parallel, continuous, and organic-rich; middle part is sub-mm-laminated, wavy, parallel, and discontinuous; upper part is contorted; (C) lower part is mm-laminated, planar, parallel, and continuous; upper part is organic-rich and lenticular-laminated with undulating micro-faults and mud clasts; (D) lower part is mm-laminated, planar, parallel, and continuous; middle part is lenticular-laminated, wavy, and discontinuous; upper part is sub-mm-laminated, planar, parallel, and continuous; (E) lower part is sub-mm-laminated, planar, parallel, and continuous; middle lower part is curved, parallel, and continuous, with erosional surface; middle upper part is wavy, nonparallel, and continuous; upper part is sub-mm-laminated, planar, nonparallel, and discontinuous; (F) lower and middle parts are sub-mm-laminated, planar, well parallel, and continuous; upper part is planar, parallel or nonparallel, and discontinuous; (G) lower part is sub-mm-laminated, planar, parallel, and continuous; middle part is mm-laminated, wavy, parallel, and continuous; upper part is lenticular and sub-mm-laminated, planar, parallel, and discontinuous; (H) lower part is sub-mm-laminated, planar, parallel, and continuous; middle part is lenticular-laminated, nonparallel, discontinuous, and erosional; upper part is sub-mm-laminated, planar, parallel, and discontinuous; (I–L) sub-mm laminated, planar, well parallel, and continuous sediment couplets; the black and white bars on the left or right of the images show paired contrasting laminations of lighter layers of coarser silt and darker layers finer clay, suggesting alternating sedimentation; (M–N) sub-mm laminated, planar, well parallel, and continuous couplets; the black and white bars corresponding to paired laminations of darker layers of coarser silt-fine sand with organic matter and lighter layers of clay; two clasts rupture underlying sub-mm laminated organic-rich laminae in the sediment couplets and are covered conformably by organic-rich laminae, suggesting that the clasts are extraclasts not being transported by bedload and interpreted as dropstones. (cont.)

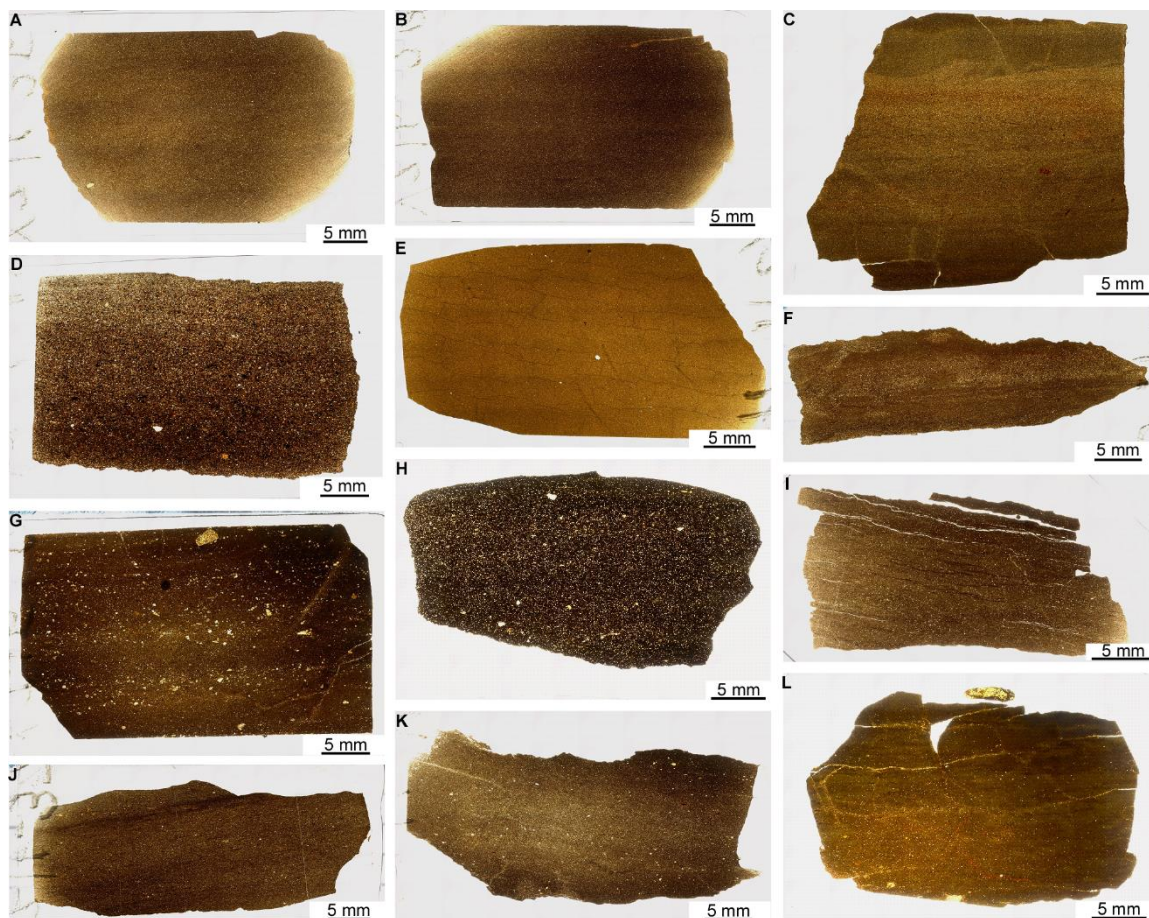


Figure 5. Photomicrographs of Hongyanchi siltstone thin-sections in plain light, showing homogeneous sedimentation. (A) massive; (B) massive; (C) mainly massive, minor weakly wavy-laminated; (D) massive with a few scattered sand-size grains; (E) massive and mottled fabric, probably weakly bioturbated; (F) massive, weakly laminated, and mottled fabric; (G) mainly massive, minor weakly laminated, coarse silt-size and sand-size grains are overall normal grading; (H) massive with a few scattered sand-size grains; (I) mainly massive, minor weakly wavy-laminated and discontinuous laminae; (J) mainly massive, minor weakly laminated, nonparallel, and discontinuous laminae; (K) massive; (L) mottled fabric, probably moderately bioturbated.

4.2. ORGANIC GEOCHEMICAL CHARACTERISTICS OF LUCAOGOU AND HONGYANCHI MUDSTONES

The lacustrine deposits in Lucaogou and Hongyanchi LCs have similar TOC and proportions of n-alkanes and steranes. TOC of all Lucaogou samples ranges in 0.01–14.30% with a mean value of 2.28%, while TOC of Hongyanchi samples ranges in 0.07–

5.98% with a mean value of 2.36% (Table 1; Figure 6A). Lucaogou and Hongyanchi samples have similar C/N ratios of 25.9–61.2 and 17.9–53.4, with a mean value of 45.3 and 37.4, respectively (Table 1). Relative abundance of n-alkanes extracted from all the Lucaogou and Hongyanchi samples are in the order of mid-chain (C_{20-25}), short-chain (C_{12-19}), and long-chain (C_{26-34}) n-alkanes with a mean proportion of 45.5, 36.9, 17.6% and 47.2, 33.8, 18.9%, respectively (Table 1; Figure 6B). C_{27-29} regular steranes in Lucaogou samples have similar relative abundance and distribution with a mean proportion of 32.5, 33.8, and 33.7%, while that in Hongyanchi samples have slightly different relative abundance and distribution with a mean proportion of 35.6, 26.4, and 38.0% (Table 1; Figure 6C). Lucaogou deposits have ratios of $C_{29} \alpha\beta\beta/(aaa + \alpha\beta\beta)$ regular steranes confined to 0.21–0.51, with a mean value of 0.38, whereas Hongyanchi deposits have the ratios restricted to 0.12–0.73, with a mean value of 0.29 (Table 1). Ratios of C_{27} Dia./($Dia. + Reg.$), calculated as C_{27} diasteranes/(diasteranes + regular steranes), range between 0.05–0.24, with a mean value of 0.15 in Lucaogou deposits, while the ratios between 0.17–0.53, with a mean value of 0.33 in Hongyanchi deposits (Table 1). Hopanes in Lucaogou and Hongyanchi samples are mainly composed of C_{27-35} $17\alpha,21\beta$ -hopanes and C_{29-30} $17\beta,21\alpha$ -moretane, with the $C_{30} \alpha\beta$ -hopane dominates in all the Lucaogou and Hongyanchi samples. The ratios of $C_{30} 17\alpha,21\beta$ -hopanes over C_{29} regular steranes ($C_{30} \text{ Hop.}/C_{29} \text{ Reg. sterane}$) are extremely high, ranging from 1.9–25.1 and 1.4–56.5, with the average values of 7.2 and 9.6 in Lucaogou and Hongyanchi samples, respectively (Table 1; Tables S7–S12).

The $\delta^{13}C_{org}$ values of lacustrine deposits in Tarlong, Taodonggou, and Zhaobishan sections decreased $\sim 5\text{‰}$ in lower Lucaogou LC and increased more than 5‰ in upper

Lucaogou LC (Fig. 3A). The $\delta^{13}\text{C}_{\text{org}}$ values of lower Lucaogou deposits range from -21.89 to -26.19‰, with a mean value of -23.86‰. The $\delta^{13}\text{C}_{\text{org}}$ values of mid and upper Lucaogou deposits are from -21.88 to -29.59‰, with a mean value of -25.63‰, whereas $\delta^{13}\text{C}_{\text{org}}$ values of Hongyanchi deposits range between -21.07 and -24.42‰, with a mean value of -22.74‰ (Figure 3A; Table 2).

Lucaogou and Hongyanchi deposits have different relative abundance of redox-sensitive biomarkers, including acyclic isoprenoids pristane and phytane, homohopane, and diasteranes. Lucaogou deposits have low ratio of pristane over phytane (Pr/Ph) with a mean value of 1.60, high homohopane index with a mean value of 0.28, and low diasteranes index with a mean value of 0.30, whereas Hongyanchi deposits have high Pr/Ph ratio with a mean value of 2.76, low homohopane index with a mean value of 0.08, and high diasteranes index with a mean value of 1.32 (Table 2; Figure 6E, F).

Lucaogou and Hongyanchi deposits have different relative abundance of salinity-sensitive biomarkers, including gammacerane, C_{27} 8 α -22,29,30-trisnorneohopane (Ts), and C_{27} 17 α -22,29,30-trisnorhopane (Tm). Lucaogou deposits have relatively high gammacerane index and Ts/(Ts+Tm) ratio with a mean value of 1.53 and 0.56, respectively, whereas Hongyanchi deposits have low gammacerane index and Ts/(Ts+Tm) ratio with a mean value of 0.12 and 0.17, respectively (Table 2; Figure 6E, I).

Table 1. Geochemical proxies diagnostic for content, type, and maturity of organic matter in 103 LCG and 47 HYC samples

	TOC (wt%)*	C/N [†]	<i>n</i> -Alkanes (%) [§]			Regular Steranes (%) [#]			C ₃₀ Hop. /C ₂₉ Reg.**	C ₂₇ Dia/ (Dia+Reg) ^{††}	C ₂₉ αββ/(αββ+α αα) ^{§§}
			S	M	L	C ₂₇	C ₂₈	C ₂₉			
LCG LC	2.28	45.28	36.9	45.5	17.6	32.5	33.8	33.7	7.2	0.15	0.38
HYC LC	2.36	37.36	33.8	47.2	18.9	35.6	26.4	38.0	9.6	0.33	0.29

* Total organic carbon content. [†] Content of carbon over nitrogen (C/N) in kerogen. [§] Peak areas of *n*-alkanes in TIC traces chromatogram: S – short chain *n*-alkanes (C₁₂-C₁₉), M – mid-chain *n*-alkanes (C₂₀-C₂₅), L – long chain *n*-alkanes (C₂₆-C₃₄). [#] Peak areas of 5α,14α,17α,(20R + 20S) and 5α,14β,17β,(20R + 20S) of C₂₇ cholestanes, C₂₈ methylcholestanes, and C₂₉ ethylcholestanes calculated in *m/z* 217 chromatogram and normalized to a total of 100%. ** C₃₀ αβ-hopane/C₂₉ regular steranes (C₃₀ Hop. /C₂₉ Reg.) was calculated as ratio of C₃₀ 17α,21β-hopane over sum of 5α,14α,17α,(20R + 20S) and 5α,14β,17β,(20R + 20S) of C₂₉ ethylcholestanes. ^{††} C₂₇ diasteranes/(C₂₇ diasteranes + C₂₇ regular steranes) was calculated by peak areas of C₂₇ 13β,17α,(20R + 20S)-diacholestanes over sum of C₂₇ 13β,17α,(20R + 20S)-diacholestanes, C₂₇ 5α,14α,17α,(20R + 20S) cholestanes, and C₂₇ 5α,14β,17β,(20R + 20S) cholestanes in *m/z* 217 chromatogram. ^{§§} Ratio of 5α,14β,17β,(20R + 20S) C₂₉ ethylcholestanes over sum of 5α,14α,17α,(20R + 20S) and 5α,14β,17β,(20R + 20S) of C₂₉ ethylcholestanes in *m/z* 217 chromatogram. Detailed data are shown in Supplementary Information Tables 7–12.

Table 2. Geochemical proxies diagnostic for pCO₂, redox condition, lake-water salinity in 103 LCG and 47 HYC samples

	δ ¹³ C _{org} (‰)*	Pr/Ph [†]	Homo. Index [§]	Diast. Index [#]	Ga. Index ^e	Ts/(Ts+Tm) ^f
LCG LC	-25.37	1.60	0.28	0.30	1.53	0.56
HYC LC	-22.74	2.76	0.08	1.32	0.12	0.17

* Organic carbon isotope ratio, determined based on delta notation (‰) relative to the Vienna Pee Dee Belemnite (V-PDB) standard. [†] Peak areas of isoprenoid in TIC traces from GC for acquiring ratio of pristane/phytane (Pr/Ph). [§] Homohopane index (Homo. Index) was calculated using peak areas of C₃₅ 17α,21β,(22R + 22S)-pentakishomohopanes over peak areas of C₃₃ counterparts in *m/z* 191 chromatogram. [#] Diasteranes index (Diast. Index) was calculated by peak areas of C₂₇ 13β,17α,(20R + 20S)-diacholestanes over sum of C₂₉ 5α,14α,17α,(20R + 20S)-24-ethylcholestanes in *m/z* 217 chromatogram. ** Gammacerane index (Ga. Index) was calculated as 10 × gammacerane/(gammacerane + C₃₀ 17α, 21β-hopane) in *m/z* 191 chromatogram. ^{††} Peak areas in *m/z* 191 chromatogram, Tm – 17α-22,29,30-trisnorhopane-C₂₇; Ts – 8α-22,29,30-trisnorneohopane-C₂₇. Detailed data are shown in Supplementary Information Tables 7–12.

5. DISCUSSION

5.1. PRECURSOR ORGANISMS INDICATED BY ORGANIC GEOCHEMICAL EVIDENCES

TOC values are indicative of relative concentration of organic matter because they are dependent on supply and preservation of OM, as well as sedimentation supply rate and dilution of siliciclastic and biogenic material (Tyson 1995; Meyers, 1997). TOC values are likely irrelevant of lithologies of the fluvial–lacustrine deposits in Lucaogou and Hongyanchi LCs, as indicated by similar ranges of TOC in dolomitic, calcareous, and organic-rich shales, limestones, and siltstones (Figure 6A). Within similar lacustrine environments, similar TOC values in different lithologies of Lucaogou and Hongyanchi deposits suggest relatively high and consistent biological productivity with proper preservation of organic matter during Lucaogou-Hongyanchi time.

Proportion of *n*-alkanes provides clues on contribution of precursor organisms to the organic matter. The mid-chain *n*-alkanes mainly originate from sphagnum (Bush and McInerney, 2013) or aquatic macrophytes (Ficken et al., 2000). Short-chain *n*-alkanes, especially *n*-C₁₅, *n*-C₁₇, *n*-C₁₉, are principally originated from phytoplankton (Meyers and Ishiwatari, 1993; Bush and McInerney, 2013), whereas long chain lipids, especially *n*-C₂₇, *n*-C₂₉, *n*-C₃₁, are commonly derived from cuticular leaf waxes of higher plants (Meyers and Ishiwatari, 1993; Bush and McInerney, 2013). Precursor organisms of organic matter remained consistent during Lucaogou-Hongyanchi time, as indicated by similar proportions of mid-, short-, and long-chain *n*-alkanes in Lucaogou and Hongyanchi deposits (Figure 6B). Additionally, dolomitic, calcareous, and organic-rich shales, limestones, and siltstones have similar distribution of mid-, short-, and long-chain

n-alkanes, suggesting that the biological sources of organic matter are not related to lithologies of Lucaogou and Hongyanchi samples.

Steranes have been used as valuable tools in geochemical correlation, environmental study, and tracking biological evolution of eukaryotes (Peters et al., 2005). The C₂₈ steranes are mainly associated with the sterol composition of specific algae (e.g., Haptophytes, Cryptophytes, and Prasinophyceae; Volkman, 1986) and leaf waxes in higher plants (Rieley et al., 1991; Volkman, 2003). C₂₉ steranes are predominately derived from vascular plants (Rieley et al., 1991; Volkman, 1986), whereas C₂₇ steranes typically constitute the sterols of algae, diatom, and zooplankton (Volkman, 2003). Similar distribution of C_{27–29} regular steranes in Lucaogou and Hongyanchi deposits suggests the precursor organisms that produced organic matter did not change during Lucaogou-Hongyanchi time (Figure 6C). Moreover, it appears that biological sources of organic matter are not relevant with lithologies of Lucaogou and Hongyanchi deposits, because different lithologies comprise similar proportions of C_{27–29} regular steranes. These interpretations are consistent with that from distributions of *n*-alkanes.

The most probable biogenic precursors of hopanes are hopanoids, which are generated from membranes of aerobic bacteria and photosynthetic cyanobacteria (Rohmer et al., 1984; Ocurisson and Albrecht, 1992). High abundance of hopanes over steranes in both Lucaogou and Hongyanchi samples suggests a considerable contribution of prokaryotic organisms to organic matter in the lake (Table 1). Overall, contribution of higher plant, algae, and bacteria into organic matter is similar in both Lucaogou and Hongyanchi deposits, as indicated by similar relative abundance of *n*-alkanes, steranes, and hopanes. This is consistent with observations on outcrops and under microscopes.

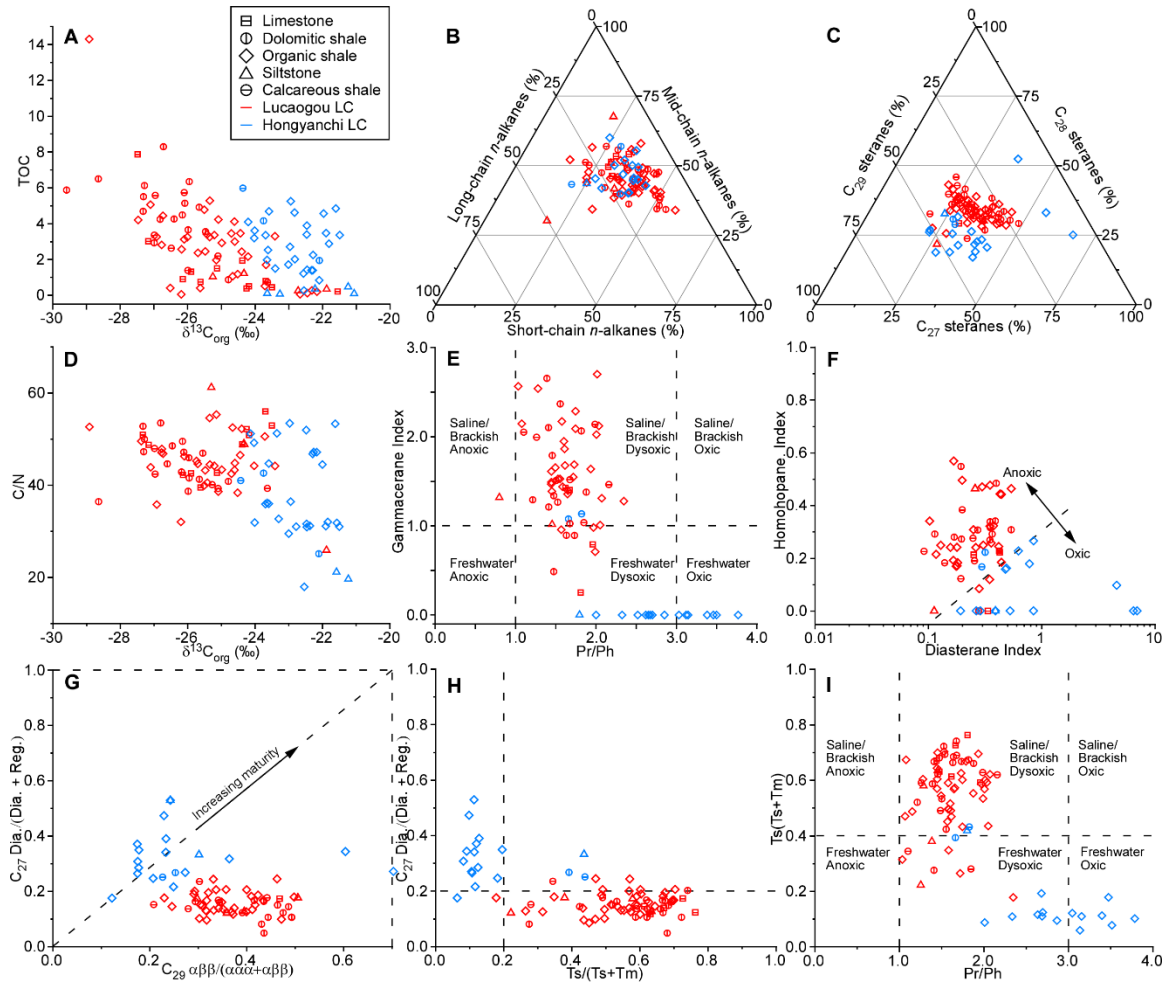


Figure 6. Geochemical proxies diagnostic for types and maturity of organic matter, redox condition, and lakewater salinity in terms of lithology. (A) scatter plot of TOC versus $\delta^{13}\text{C}_{\text{org}}$, showing similar TOC in LCG and HYC deposits, $\delta^{13}\text{C}_{\text{org}}$ values are higher in HYC than in LCG deposits; (B) (C) ternary diagrams of proportions of long-chain (C_{26-34}), mid-chain (C_{20-25}), and short-chain n -alkanes (C_{12-19}) and C_{27} steranes, C_{28} methylcholesteranes, and C_{29} ethylcholesteranes, similar proportions suggest similar origins of organic matter in LCG and HYC LCs; (D) scatter diagram of C/N versus $\delta^{13}\text{C}_{\text{org}}$ in kerogen, no correlation between $\delta^{13}\text{C}_{\text{org}}$ and C/N suggests that $\delta^{13}\text{C}_{\text{org}}$ is not related with origins of organic matter; (E) scatter plot of Pr/Ph versus gammacerane index, LCG LC has low Pr/Ph and high gammacerane index whereas HYC LC has high Pr/Ph and low gammacerane index suggest that LCG deposit is formed in relatively more anoxic and saline environment than HYC deposits; (F) scatter plot of homohopane index versus diasterane index, high homohopane index and low diasterane index in LCG deposits suggest anoxic waterbody, low homohopane index and high diasterane index in HYC deposits suggest oxic waterbody; (G) scatter diagram of C_{27} diasteranes/(diasteranes + regular steranes) and C_{29} ethylcholesteranes $\alpha\beta\beta/(\alpha\alpha\alpha + \alpha\beta\beta)$, similar values of the two proxies of LCG and HYC deposits suggest similar thermal maturity of organic matter; (H) scatter diagram of C_{27} Dia./(Dia. + Reg.) and $\text{Ts}/(\text{Ts} + \text{Tm})$, no correlation between the two proxies suggests that $\text{Ts}/(\text{Ts} + \text{Tm})$ is controlled by depositional environments instead of thermal maturity of the organic matter; (I) scatter plot of Pr/Ph versus $\text{Ts}/(\text{Ts} + \text{Tm})$ ratio, LCG LC has low Pr/Ph and high $\text{Ts}/(\text{Ts} + \text{Tm})$ ratio whereas HYC LC has high Pr/Ph and low $\text{Ts}/(\text{Ts} + \text{Tm})$ ratio suggest that LCG deposit is formed in relatively more anoxic and saline environment than HYC deposits.

5.2. ORGANIC CARBON ISOTOPE STRATIGRAPHY

Organic carbon isotope stratigraphy of Lucaogou and Hongyanchi LCs in northwest China have been used to correlate with organic carbon and inorganic carbon isotope stratigraphy of lower Permian in order to estimate age of Lucaogou and Hongyanchi LCs. Although with spatial and temporal variability, stable carbon isotopic trends and excursions in stratigraphic records have been generally applied in chemostratigraphic and geochronologic correlations, because fractionation of ^{13}C and ^{12}C in organic carbon (C_{org}) and carbonate carbon (C_{carb}) reservoirs reflects Earth's carbon cycling between atmosphere, hydrosphere, lithosphere, and biosphere (Siegenthaler and Sarmiento, 1993; Falkowski et al., 2000; Saltzman and Thomas, 2012). In this study, increasing trends of $\delta^{13}\text{C}_{\text{org}}$ value in lower Lucaogou LC and Hongyanchi LC in Bogda, NW China coincide with increasing trends of $\delta^{13}\text{C}_{\text{carb}}$ value of marine limestones in western paleoequatorial Euramerica and south China (Saltzman and Thomas, 2012) in early Sakmarian and Artinskian–early Kungurian, respectively, whereas a decreasing trend of $\delta^{13}\text{C}_{\text{org}}$ value in mid-upper Lucaogou LC corresponds to a decreasing trend $\delta^{13}\text{C}_{\text{carb}}$ value (Saltzman and Thomas, 2012) in mid-late Sakmarian (Figure 3A, B). In addition, the general trends of $\delta^{13}\text{C}_{\text{org}}$ in southeastern Kazakhstan, mid-latitude northeast Pangea are consistent with $\delta^{13}\text{C}_{\text{org}}$ trends in paleoequatorial western Euramerica, north China Platform (Montañez et al., 2007), and paleo-high-latitude eastern Australia (Birgenheier et al., 2010; Frank et al., 2015), as well as trends of $\delta^{13}\text{C}_{\text{carb}}$ in paleoequatorial western Euramerica and south China (Buggisch et al., 2011) and paleo-high-latitude Russia (Buggisch et al., 2011). Thus, the Lucaogou LC likely ranges in early-latest Sakmarian and Hongyanchi LC likely ranges in Artinskian–early Kungurian,

as evidenced by the correlation of carbon isotope stratigraphic profiles and constrain of U/Pb zircon ages of 301.26 ± 0.05 Ma in uppermost lower Daheyan LC and 281.42 ± 0.10 Ma in uppermost Hongyanchi LC.

Fossil plant $\delta^{13}\text{C}_{\text{org}}$ and pedogenic carbonate $\delta^{13}\text{C}_{\text{carb}}$ records in paleoequatorial Eurameriacan have been used to estimate Permo-Carboniferous atmospheric pCO_2 (Figure 3B; Montañez et al., 2007, 2016). Photosynthesis is the main process fractionating $^{12}\text{C}_{\text{org}}$ from $^{13}\text{C}_{\text{org}}$, resulting in depletion of heavy isotope (^{13}C) in organic matter (Freeman and Haye, 1992). The relationships between atmospheric CO_2 content and the carbon isotopic compositions of atmospheric CO_2 and C_3 plants have been established (Hayes et al., 1999). CO_2 concentration (pCO_2) between atmosphere and stoma of C_3 plants lead to the discrimination against ^{13}C during the production of their tissues (Farquhar et al., 1982; 1989; Hayes et al., 1989). As a result, the $\delta^{13}\text{C}_{\text{org}}$ is -18 to -16‰ more negative than atmospheric $\delta^{13}\text{C}$ and an increase of $\delta^{13}\text{C}_{\text{org}}$ likely suggests a decrease of atmospheric pCO_2 , and vice versa (Smith and Epstein, 1971; O’Leary, 1981, 1988).

The $\delta^{13}\text{C}_{\text{org}}$ values in this study are more likely associated with atmospheric CO_2 rather than variations of ^{12}C fractionating between land plant and lacustrine algae, giving that similar biological sources of organic matter in Lucaogou and Hongyanchi deposits are evidenced by similar distributions of *n*-alkanes, steranes, and hopanes. In addition, $\delta^{13}\text{C}_{\text{org}}$ values are likely independent of abundance and origins of organic matter and lithologies, as suggested by irrelevance between $\delta^{13}\text{C}_{\text{org}}$ values and TOC, ratios of carbon over nitrogen in kerogen (C/N), and lithologies, respectively (Figure 6A, D). C/N ratio can be used to differentiate organic matter derived from algae and terrestrial plant due to

richness of protein and absence of cellulose in algae while a small amount of protein and plenty of cellulose in vascular plants (Meyers, 1997).

The $\delta^{13}\text{C}_{\text{org}}$ values of fluvial-lacustrine deposits in Bogda are likely related to changes of atmospheric pCO_2 , coinciding with Gondwanan glaciation and deglaciation. The increasing trend of $\delta^{13}\text{C}_{\text{org}}$ with fluctuating values in lower Lucaogou LC corresponded to end of waxing stages of Gondwanan glaciation (P1) in early Sakmarian (Figure 3A, B; Isbell et al., 2003a, 2003b, 2012; Montañez et al., 2007; Fielding et al., 2008a, 2008b, 2008c), suggesting oscillations of atmospheric CO_2 during possible stepped glacial retreat on Gondwana land. The general decreasing trend of $\delta^{13}\text{C}_{\text{org}}$ values coincided with increasing atmospheric CO_2 during waning stage of interglaciation between P1 and P2 in mid-late Sakmarian, whereas increasing trend of $\delta^{13}\text{C}_{\text{org}}$ values were consistent with decreasing atmospheric CO_2 during glacial P2 in Artinskian–early Kungurian (Figure 3A, B). These results are consistent with widespread collapse of ice sheets over most of Gondwana accompanying with a series of postglacial transgressive deposits driven by glacioeustasy, coincided with increasing atmospheric CO_2 and tropical sea-surface temperatures in mid Sakmarian (Isbell et al., 2003b; Montañez et al., 2007, 2016; Fielding et al., 2008b, 2008c; Stollhofen et al., 2008; Lopez-Gamundi and Buatois, 2010; Montañez and Poulsen, 2013) and periodic returns of regional glaciation in eastern Gondwanan in Artinskian, including eastern Australia (Fielding et al. 2008a, Mory et al. 2008; Waterhouse and Shi 2010; Frank et al., 2015), western Australia (Eyles et al., 2003, 2006), and New Zealand (Waterhouse and Shi 2010). The coincidence of Gondwana glacial–interglacial transitions and atmospheric pCO_2 changes through simulations (Poulsen et al., 2007; Peyser and Poulsen, 2008) and interpretation from paleo-tropical

Eurameriacan (Eyles, 1993; Montañez et al., 2007, 2016) and southeastern Kazakhstan of this study suggests a linkage existed between Gondwanan glaciation and atmospheric $p\text{CO}_2$.

5.3. CLIMATIC CONDITIONS INDICATED BY SEDIMENTARY EVIDENCE

5.3.1. Redox Condition Indicated by Lamination and Bioturbation.

Lamination and bioturbation can be used to assess redox condition because laminated shales are typically formed as continuous sediment accumulation settle out of suspension in relatively quiet and anoxic depositional conditions while bioturbation in mudstones is associated with oxygen level, nutrient availability, and sedimentation rate in bottom water during deposition (Lazar et al., 2015). However, preservation of lamination alone in shales is not necessary to suggest an anoxic water column. The laminated fabrics of shales may not be disrupted by any aerobic organisms even if free oxygen was available to support the organisms because laminations and beddings can be preserved under disturbance of bioturbation when sedimentation rate is high. Nevertheless, well-developed laminations, absence of bioturbation, and rare benthic fossils in Lucaogou shales collectively suggest relatively quiet and anoxic bottom-water during Sakmarian. Absence of laminations and presence of common burrows and discontinuous bedding destroyed by moderate bioturbation in Hongyanchi siltstones indicate oxic and energetic water condition during Artinskian–early Kungurian. Remarkably, laminated shales are confined to interglacial stage between P1 and P2 in mid-late Sakmarian while a mixture of laminated shales and massive siltstones are constrained in glacial retreat stage of P1 in early Sakmarian, whereas massive and bioturbated siltstones are restricted in glacial stage of P2 in Artinskian–early Kungurian (Figure 3A). It is striking that laminated black

shales are dominated in the Usclas-St Privat, Tuilières-Loiras, and Viala Formations (late Asselian-Sakmarian) in the Lodève basin, France, while massive clayish siltstones are dominated in the Octon Member of Salagou Formation (mid-late Artinskian; Figure 2B; Schneider et al., 2006; Michel et al., 2015). This is also similar to laminated sediments occurred in interglacial intervals and bioturbated sediments deposited during last glacial interval, on basis of core sediment records in tropical Atlantic (Peterson et al., 2000) and eastern tropical North Pacific (Ganeshram et al., 2002).

5.3.2. Seasonality Indicated by Couplets and Dropstones. The light-colored coarse-grained and darker-colored fine-grained sediment couplets in Lucaogou shales (Figure 4I-L) are typically interpreted as annual clastic varves while the light-colored fine-grained and darker-colored coarse-grained sediment couplets in Lucaogou shales (Figure 4M-N) are typically interpreted as annual clastic-biogenic (mixed) varves. Varves are all annually deposited rhythmic laminations of sediments in lacustrine and marine, formed from glacial retreat or changes of carbonate and evaporite precipitation and biological production due to seasonality (De Geer, 1912; Clausen and Boy, 2000; Zolitschka et al., 2015).

Varved deposits in Lucaogou LC suggest strong seasonality in southeastern Kazakhstan at mid-latitude northeast Pangea during early-mid Sakmarian, whereas absence of varves in Hongyanchi LC suggests weak seasonality during Artinskian–early Kungurian. The light-colored laminae in the clastic varves formed when coarse silt and fine sand deposited immediately after being transported while fine silt and clay suspended longer as sediments transported from surrounding drainage basin, likely caused by ice or snow melting during summer. On the contrary, the dark-colored laminae

accumulated when fine-grained clay settled down from the leftover suspension of clay particles and no further sediments influx in an ice-covered lake during winter.

Alternatively, the coarser sediments were transported and deposited in the lake due to enhanced rainfall in wet seasons while only finer sediments deposited in the lake as a result of decreased rainfall in dry seasons. In either scenario, seasonal changes of temperature or precipitation are responsible for the influx of allochthonous siliciclastic components into the lake for formation of varves. In clastic-biogenic (mixed) varves, the darker laminae contains coarse silt and fine sand with abundant organic matter deposited during warm and humid seasons when bio-productivity was high, whereas pale laminae consists of fine silt and clay with rare organic matter deposited during cold and dry seasons when bio-productivity was low. Lucaogou varved deposits are similar to varved lake sediments in the Usclas-St Privat, Tuilières-Loiras, and lower part of Viala Formations in the Lodève basin (Schneider et al., 2006; Michel et al., 2015), suggesting strong seasonality of mid- and low-latitude northeastern Pangea during Sakmarian.

The two clasts rupturing the underlying laminae in shales from basal Lucaogou LC are interpreted as dropstones. Dropstones are outsized and exotic clasts of anomalous lithology vertically or oblique introduced into fine-grained matrix, posing a hydrodynamic paradox between oversized clasts and low energy depositional process of the matrix (Bennett et al., 1996). The small size of the dropstones in Lucaogou shales suggest a seasonal frozen lake rather than iceberg in Tarlong-Taodonggou lake because ice-rafted dropstones in seasonally frozen lake environments usually have limited size comparing with that from ice bergs (Bennett et al., 1996). Therefore the dropstones in Lucaogou shales may have been transported by ice rafting during cold season and

deposited when seasonal lake ice melted, although deposition of dropstones have been best interpreted by ice rafting and melting related to glacial event (e.g., Le Heron et al., 2017), non-glacial processes derived from delta collapse during ice retreat (e.g., Vesely et al., 2018), grain flow and debris flows, biological rafting agents, and volcanic projectiles (Bennett et al., 1996). In addition, Yang et al. (2007) also interpreted dropstones in an organic-rich shale of Lucaogou LC from melting lake ice. Collectively, laminated shales, dropstones, and disrupted varves in Lucaogou LC comprise the strongest evidence of strong seasonality of southeastern Kazakhstan at mid-latitude northeast Pangea in Sakmarian, whereas massive and bioturbated sediments of Hongyanchi LC suggest weak seasonality during Artinskian–early Kungurian (Figure 3A).

5.4. CLIMATIC CONDITIONS INDICATED BY ORGANIC GEOCHEMICAL EVIDENCES

5.4.1. Precipitation Indicated by Biomarkers. High gammacerane index and $Ts/(Ts+Tm)$ ratio in mid-upper Lucaogou deposits suggest saline-brackish lake water, which was likely originated in arid climatic conditions during mid-late Sakmarian while low gammacerane index and $Ts/(Ts+Tm)$ ratio in lower Lucaogou and Hongyanchi deposits indicate the lake was freshwater, and likely occurred in humid climatic conditions during early Sakmarian and Artinskian–early Kungurian (Figure 3A). Gammacerane is a highly specific indicator of stratified water column (Sinninghe Damsté et al., 1995), commonly result from hypersalinity at depth (Peters et al., 2005). Gammacerane may be associated with reduction of tetrahymanol in membranes of certain protozoa (Ourisson et al., 1987; ten Haven et al., 1989) or bacterivorous ciliates which occur at the interface between oxic and anoxic zones in stratified water columns

(Sinninghe Damste et al., 1995; Sepúlveda et al., 2009). $Ts/(Ts+Tm)$ ratios may be used as a salinity-sensitive proxy when samples are at similar thermal maturity level, because $Ts/(Ts+Tm)$ ratios increase in hypersaline depositional environments (Moldowan et al., 1986; Rullkötter and Marzi, 1988). Gammacerane index and $Ts/(Ts+Tm)$ ratio, as proxies of salinity, can further indicate arid conditions because saline lakes are distributed worldwide in semi-arid to arid climatic zones, under control of high evaporation and low precipitation (Waiser and Robarts, 2009).

Precipitation indicated by biomarkers in Lucaogou and Hongyanchi LCs are broadly consistent with climate interpretation from high-order cycle types and paleosols (Yang et al., 2007, 2010). In addition, low and high gammacerane index and $Ts/(Ts+Tm)$ ratio of Lucaogou deposits suggest highly fluctuating precipitation and humid climate in the end of glacial P1 during early Sakmarian and interglacial stage between P1 and P2 during mid-late Sakmarian. Stable trends of low gammacerane index and $Ts/(Ts+Tm)$ ratio of Hongyanchi deposits suggest constantly arid climate in glacial stage of P2 during Artinskian–early Kungurian. This is in accordance with seasonality interpreted from varves and dropstones. Remarkably, precipitation and seasonality in Bogda are likely linked with glacial activity, as evidenced by synchronous changes of these salinity-sensitive biomarkers and changes of $\delta^{13}C_{org}$ (Figure 3A). A gradual increase of gammacerane index and $Ts/(Ts+Tm)$ ratio was accompanied by a gradual increase of $\delta^{13}C_{org}$ during the transition from glaciation P1 to interglaciation in early Sakmarian. A rapid decrease of gammacerane index and $Ts/(Ts+Tm)$ ratio occurred simultaneously with a striking increase of $\delta^{13}C_{org}$ during the transition from interglaciation to glaciation P2 in latest Sakmarian.

5.4.2. Redox Condition Indicated by Biomarkers. Relatively low values of Pr/Ph and diasteranes index and high values of homohopanes index of Lucaogou deposits suggest Lucaogou lake was relatively more anoxic than Hongyanchi lake, in which deposits are characterized by relatively high values of Pr/Ph and diasteranes index and low values of homohopanes index (Figure 3A). Pr/Ph ratio, homohopane index, and diasteranes index are generally considered as a redox parameters when organic matter has similar thermal maturity (Peters et al., 2005), because pristane may be oxidized from phytol side chain of chlorophylls whereas phytane may be reduced from phytol in chlorophylls (Didyk et al., 1978) and C₃₅ hopanes and diasteranes are commonly associated with highly reducing conditions (Moldowan et al., 1986; Peters and Moldowan., 1991). Multiple redox-sensitive biomarkers of Lucaogou and Hongyanchi samples show persistent result of redox conditions of lake water from early Sakmarian to early Kungurian. This is also consistent with redox condition of depositional environments interpreted from laminated shales and varved deposits in Lucaogou LC and massive and bioturbated siltstones in Hongyanchi LC.

Redox condition of water column, as an integrated effect of oxygen cycling in biosphere, atmosphere, and geosphere of a lake system, reflects basin hydrology and climate. Oxygen is depleted by biological and inorganic oxidation while supplied with oxygenated fresh waters from fluvial influx, via exchange with atmosphere, and as byproduct of photosynthesis. Redox condition is not related to lithologies because organic-rich shales can be deposited in both oxic and anoxic environments interpreted from redox-sensitive biomarkers (Figure 6E, F). Redox condition of the lake water is likely related to basin hydrology and climate, as evidenced by concurrent changes of

redox-sensitive biomarkers and precipitation-sensitive biomarkers (Figure 3A). A slightly decreasing trend of Pr/Ph and increasing trend of homohopane index coincide with an overall increasing trend of gammacerane index and Ts/(Ts+Tm) ratio during the transition from glacial stage of P1 to interglacial stage in early Sakmarian. A dramatic increase of Pr/Ph and decrease of homohopane index are coincident with a remarkable decrease of gammacerane index and Ts/(Ts+Tm) ratio during the transition from interglacial to glacial stage of P2 in latest Sakmarian. Sufficient oxygen in lake water were likely supplied by constant influx in humid climate whereas an anoxic lake were likely caused by limited influx in arid climate.

5.4.3. Thermal Maturity and Use of Biomarkers. Similar values of biomarker parameters including steranes isomerization, diasteranes, and terpanes indicate samples in Lucaogou and Hongyanchi LCs have similar thermal maturity, so the use of biomarkers in interpretation of precursor organisms, redox condition, and lakewater salinity is reasonable. Ratio of $\alpha\beta\beta/(\alpha\alpha\alpha + \alpha\beta\beta)$ for C₂₉ regular steranes (20S + 20R) is highly specific for maturity because isomerization at C-14 and C-17 in the C₂₉ steranes causes an increase in $\beta\beta$ isomers with increase of maturity (Seifert and Moldowan, 1986). Ratio of Dia./(Dia. + Reg.) is typically effective to describe thermal maturity because diasteranes are thermally more stable than regular steranes, although it is partly affected by acidic clays in oxic depositional environments (Peters et al., 2005). C₂₇ 18 α -trisnor-hopane (Ts) is more stable than C₂₇ 17 α -trisnor-hopane (Tm) during catagenesis, therefore, Ts/(Ts+Tm) ratio is generally used as one of most reliable indicators for maturity assessment of samples from similar environments (Seifert and Moldowan, 1978; Peters et al., 2005).

Lucaogou and Hongyanchi deposits have similar ranges of $C_{27} \text{ Dia.}/(\text{Dia.} + \text{Reg.})$ and $C_{29} \alpha\beta\beta/(\alpha\alpha\alpha + \alpha\beta\beta)$ ratios along the maturity gradient, suggesting organic matter of Lucaogou and Hongyanchi deposits have similar maturity ranging from immature to submature (Figure 6G). Relatively low ratios of $C_{27} \text{ Dia.}/(\text{Dia.} + \text{Reg.})$ of Lucaogou deposits can be explained by organic-rich and carbonate-rich rocks deposited in relatively anoxic water column. This is consistent with sedimentological evidence and redox-sensitive biomarker proxies. In addition, no overlap of Lucaogou and Hongyanchi samples in the diagram of $C_{27} \text{ Dia.}/(\text{Dia.} + \text{Reg.})$ versus $Ts/(Ts+Tm)$ suggest that these two maturity-sensitive biomarker parameters may have been affected by different depositional conditions of Lucaogou and Hongyanchi lakes (Figure 7H). Furthermore, $Ts/(Ts+Tm)$ versus Pr/Ph ratios of Lucaogou and Hongyanchi samples (Figure 6I) show similar interpretations of redox conditions and salinity of lakewater interpreted from gammacerane index and Pr/Ph ratios (Figure 6E). Therefore, $Ts/(Ts+Tm)$ ratios were probably controlled by lakewater salinity, and thus can be used as a salinity-sensitive proxy (e.g., (Moldowan et al., 1986; Rullkötter and Marzi, 1988)). Last, ratios of $C_{27} \text{ Dia.}/(\text{Dia.} + \text{Reg.})$, $C_{29} \alpha\beta\beta/(\alpha\alpha\alpha + \alpha\beta\beta)$, and $Ts/(Ts+Tm)$ are probably not linked with lithologies, as evidenced by non-correlation between any of these proxies and lithologies.

5.5. CAUSES OF CLIMATIC CHANGES

Dramatic climate changes during Pennsylvanian–Permian have been inferred from climate-sensitive lithotypes, stable isotopic records, and modeling (Poulsen et al., 2007; Montañez et al., 2007; Tabor and Poulsen, 2008; Boucot et al., 2013). Northwestern Pangea and western Gondwana remained arid while Siberia, southern Gondwana, and eastern Tethyan blocks experienced persistent humidity, whereas western

and central equatorial Pangea, northern Pangea, eastern Gondwana experienced an increased aridity (Chumakov and Zharkov, 2002; Tabor and Poulsen, 2008; Boucot et al., 2013). By analogy with modern climate patterns, long-term drying trends of western and central tropical Pangea have been attributed to northward migration of most of Pangea out of tropical humid climatic zones into northern subtropical arid zone during 320–280 Ma (Tabor and Poulsen, 2008; Tabor et al., 2008). However, continental drift cannot explain increasing humidity of southeastern Kazakhstan in mid-latitude northeastern Pangea and the Lodève basin in low-latitude northeastern Pangea in Artinskian because they remained in the same climatic zone as indicated by a southward drift of $\sim 3^\circ$ of Kazakhstan and $\sim 6^\circ$ of the Lodève basin during 300–280 Ma (Tabor and Poulsen, 2008; Scotese, 2014). The general aridification of low-latitude Pangea may have been caused by increasing distance from moisture sources and amplified continentality as a result of withdrawal of epeiric seas and assembly of Pangea (Parrish, 1993; Tabor and Montañez, 2002; Scotese, 2014). However, land-sea distribution and supercontinentality do not explain intercalation of humid and arid climate in of Bogda and the Lodève basin in low- and mid-latitude of northeastern Pangea and Yongcheng Basin in North China.

The cyclic deposits and intercalation of humid and arid climate in low- and mid-latitude Northern Hemisphere may have been controlled by Gondwanan glacial activities. Because the cyclic deposits in Bogda during late Asselian-early Kungurian are similar to cyclothems in ① Lodève Basin of France, ② western Urals of Russia, ③ Mid-Continent Basin in Kansas, ④ Yongcheng Basin in North China, and ⑤ Queensland, Australia during the same interval (Fig. 2B; Schneider et al., 2006; Michel et al., 2015; Kossovaya et al., 2013; Miller and West, 1998; Mazullo et al., 2007). It is striking that humid and

arid climate of Bogda are correlated with that in the Lodève Basin and Yongcheng Basin during early Sakmarian-late Artinskian (Figures 2B, 3A; Schneider et al., 2006; Roscher and Schneider, 2006; Michel et al., 2015; Yang et al., 2014; 2016). The humid climate of Bogda in early Sakmarian is correlated with wet phase of Usclas-St Privat and lower Tuilières-Loiras Formations in the Lodève Basin and humid condition of lower Shanxi Formation in the Yongcheng Basin during late Asselian-early Sakmarian. The arid climate of Bogda in mid Sakmarian is correlated with dry phase of upper Tuilières-Loiras and Viala Formations in the Lodève Basin and less humid condition of mid Shanxi Formation in the Yongcheng Basin during mid Sakmarian. The humid climate of Bogda in Artinskian is correlated with wet phase of Rabejac Formation in the Lodève Basin and humid condition of Xiashihezi Formation in the Yongcheng Basin during Artinskian.

In addition, the humid climate of Bogda, Lodève Basin, and Yongcheng Basin during early Sakmarian and Artinskian are largely correlated with cold ocean water in western Urals, sea level fall in Mid-Continent, and glaciation of eastern Australia while arid climate of Bogda, Lodève Basin, and Yongcheng Basin during mid Sakmarian are correlated with warm ocean water in western Urals, sea level rise in Mid-Continent, and interglaciation of eastern Australia (Figures 2B, 3A). Coincidence of climate changes in low- and mid-latitude northeast Pangea and North China, sea level changes in paleotropical western Pangea, temperature changes of ocean water in mid-latitude northeast Pangea, and glacial activities in Australia suggest that precipitation of North Hemisphere may have been probably linked with Gondwanan glacial cycles.

Waxing and waning of ice sheets on Gondwana have been proposed to exert a significant control on large-scale atmospheric circulation over low-latitude Pangea

(Perlmutter and Matthews, 1989; Cecil, 1990; Chumakov and Zharkov, 2002; Cecil et al., 2003; Tabor and Poulsen, 2008; Peyser and Poulsen, 2008; Montañez and Poulsen, 2013). Atmospheric high pressure zone over Gondwanan ice sheets may have compressed the of Intertropical Convergence Zone (ITCZ) into a narrow belt of humidity and stability over equatorial Pangea during glacial, whereas shrinkage of polar high-pressure cells may have permitted seasonal migration of the ITCZ toward the summer-hemisphere mid-latitudes, result in amplified aridity and seasonality across equatorial Pangea during interglacial (Figure 7A, B; Cecil, 1990; Parrish, 1993; Miller et al., 1996; Cecil et al., 2003; Poulsen et al., 2007; Tabor and Poulsen, 2008; Allen et al., 2011). A low pressure zone over mid-latitude North Hemisphere may have been produced in accompany with the squeezed narrow ITCZ over equatorial Pangea during glacial, giving rise to humid and stable climate over mid-latitude northeast Pangea (Figure 7A). A low pressure zone of rainfalls over mid-latitude northeast Pangea may have been generated when the seasonal migration of the ITCZ reach 30° North Hemisphere in boreal summer during interglacial, while a high pressure zone without rainfall over mid-latitude northeast Pangea may have been developed when the ITCZ migrated to equatorial Pangea and 30° South Hemisphere in austral summer during interglacial, result in arid and seasonal climate of mid-latitude northeast Pangea (Figure 7B). Collectively, these models suggest enhanced aridity and seasonality during interglacial while reinforced humidity and stability during glacial, which are reconciled with climatic changes of Bogda, Lodève Basin, and Yongcheng Basin and Gondwanan glacial cycles during Sakmarian–early Kungurian.

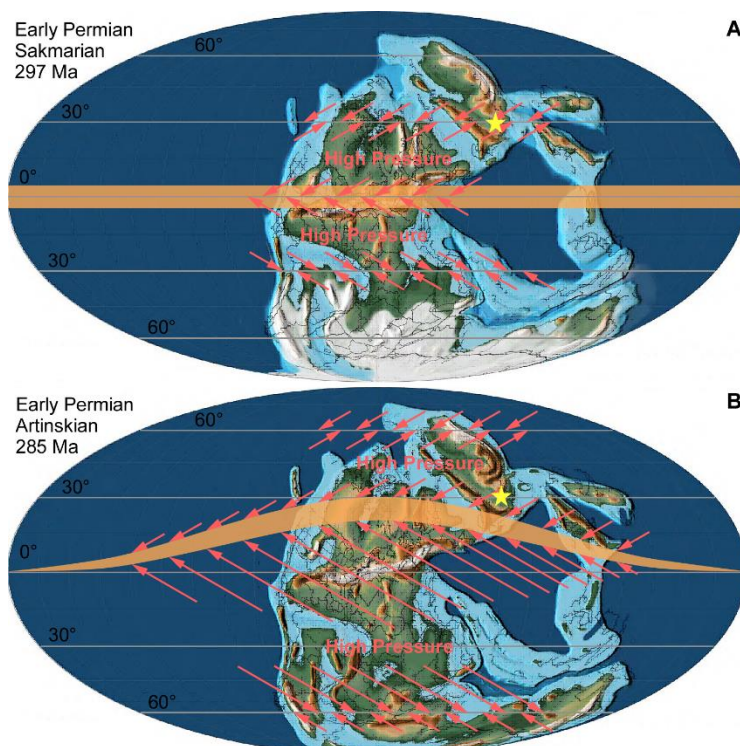


Figure 7. Conceptual model. Climate changes were caused by migration of Intertropical Convergence Zone (ITCZ) during waxing and waning of ice sheets on Gondwana, modified from Cecil et al. (2003). (A) Atmospheric high pressure zone over Gondwanan ice sheets squeezed migration of the ITCZ into a narrow belt of humidity and stability over equatorial Pangea and a low pressure zone over mid-latitude North Hemisphere during glacial. (B) Shrinkage of polar high-pressure cells during interglacial produced a low pressure zone of rainfalls over mid-latitude NE Pangea when the ITCZ reach mid-latitude North Hemisphere in boreal summer while a high pressure zone without rainfall when the ITCZ migrated to equator and South Hemisphere in other seasons.

However, shortcomings still limit a satisfactory model of Pennsylvanian–Permian climates. Geochronological and stable $\delta^{13}\text{C}_{\text{org}}$ correlations of the glacial stages P1 and P2 and interglacial stage in southeastern Kazakhstan mid-latitude northeast Pangea with Gondwanan glacial–interglacial cycle in South Hemisphere have relatively coarse resolution. This highlights the need of higher high-resolution chronostratigraphic dating to improve the time frame and constrain the correlation of stratigraphic records in North Hemisphere with Gondwanan glaciation and interglaciation. In addition, uncertainty

remains on impact of seasonal shifts of the ITCZ over northeast and tropical Pangea in response of high pressure cells produced over Gondwanan ice sheets (Peyser and Poulsen, 2008). This requires further exploration on climate changes of mid- and high-latitude Pangea during Pennsylvanian–Permian. More climate-sensitive lithostratigraphic and geochemical indicators are also needed to estimate the influence of the data–climate model. Last but not least, multiple climate factors, instead of single independent climate factor, may have been collectively exerted substantial effects on climate changes at different temporal and spatial scale. This emphasizes on consideration of the overall picture of global climatic changes during the late Paleozoic glacial age.

6. CONCLUSIONS

Climatic changes of southeastern Kazakhstan mid-latitude northeast Pangea may have been under control of migration of the ITCZ, constrained by dynamic glacial cyclicity in Southern Hemisphere during the late Paleozoic. Humidity and seasonality are suggested by a mixture of laminated shales and massive siltstones, varves with dropstones, and low gammacerane index and $Ts/(Ts+Tm)$ ratios, corresponding to late Paleozoic retreat of glacial P1 over most of Gondwana in early Sakmarian. Enhanced aridity and seasonality evidenced by sub-mm- and mm-laminated shales, varved deposits, and high gammacerane index and $Ts/(Ts+Tm)$ ratios are confined to interglacial stage between P1 and P2 during mid-late Sakmarian. Increased humidity and reduced seasonality indicated by massive and bioturbated siltstones, absence of varves, and low gammacerane index and $Ts/(Ts+Tm)$ ratios coincided with glacial stage of P2 in

Artinskian–early Kungurian. The climatic changes in southeastern Kazakhstan mid-latitude northeast Pangea are largely correlated with that in low-latitude eastern Pangea and North China and synchronous with Gondwanan glacial cycles, suggesting that waxing and waning of ice sheets in Southern Hemisphere may have played a significant role in climatic changes of Northern Hemisphere. Humid and stable climate of southeastern Kazakhstan may have been caused by a low pressure zone of rainfalls over mid-latitude northeast Pangea and a stable ITCZ over equatorial Pangea during glacial. Arid and seasonal climate over southeastern Kazakhstan may have been induced by a dominance of high pressure zone without rainfalls and seasonal migration of the ITCZ between 30° of North and South Hemisphere during interglacial.

However, a growing need for testing impact of climate factors in data-climate models requires more sensitive-climate indicators, higher high-resolution geochronologic dating, and better-constrained correlation between stratigraphic records in North and South Hemisphere. This study provides a workable method of relatively well-constrained time frame via combination of stable $\delta^{13}\text{C}_{\text{org}}$ chemostratigraphy and geochronologic ages. Notably, this study also shows that common lithotypes and biomarkers, including laminated shales, varves, dropstones, gammacerane index, and $\text{Ts}/(\text{Ts}+\text{Tm})$ ratios can be used to interpret climatic changes over southeastern Kazakhstan mid-latitude northeast Pangea, and thus can be used as climate-sensitive proxies for reconstruction of paleoclimates in other continental stratigraphic successions. This will contribute to better understanding of the linkage between glacial–interglacial dynamics in South Hemisphere and climatic responses in paleo-tropics and North Hemisphere.

ACKNOWLEDGMENTS

We appreciate for Dr. Hong Lu, Dr. Qingtao Wang, Taoli Wang, Dr. Jing Liao, Dr. Yankuan Tian, and Dr. Shutao Gao of Guangzhou Institute of Geochemistry, Chinese Academy of Sciences and Dr. Qiao Feng and Bingkai Wang of Shandong University of Science and Technology for GC-MS and GC-IRMS facilities. We would like to thank Dr. Zewen Liao, Dr. Guoying Sheng, and Dr. Zhao-Wen Zhan of Guangzhou Institute of Geochemistry, Chinese Academy of Sciences, Mingli Wan of Nanjing Institute of Geology and Palaeontology, Chinese Academy of Sciences, Dr. David J. Wronkiewicz, Dr. Jonathan Obrist Farner, and Dr. Stephen Gao of Missouri S&T for advices. This research was partially supported by four student research grants from Geological Society of America, American Association of Petroleum Geologists, and State Key Laboratory of Organic Geochemistry, Chinese Academy of Sciences (grant no. SKLOG-201603) to Xin Zhan, NSF China grant (41428201) and NSF GEOSCI grant (1714749) to Dr. Wan Yang, and the Strategic Priority Research Program of Chinese Academy of Sciences (grant no. XDA14010102) to Yujiao Zhang.

APPENDIX A. SUPPLMENTARY MATERIAL

Table S1. Sedimentary characteristics of samples in north Tarlong

Sample	Meters over base of LCG (m)	Low-Order Cycle	Lithology	Sedimentary Textures & Structures	Depositional Environments
XZ16-16	243.2	HYC LC	Siltstone	Greenish gray, variably silty, platy, massive, laterally persistent, weakly calcareous, common ostracods	Littoral
XZ16-15	240.1	HYC LC	Siltstone	Dark gray, thick platy, mainly massive, weakly parallel & wavy laminated, common iron nodules, non-calcareous, no fossils	Profundal
XZ16-14	235.2	HYC LC	Siltstone	Dark gray, thick platy, massive & wavy laminated, climbing ripples, common iron nodules, non-calcareous, no fossils	Profundal
XZ16-13	231.6	HYC LC	Siltstone	Dark gray, thin platy, massive, non-calcareous, no fossils	Profundal
XZ16-12	229.0	HYC LC	Siltstone	Blackish gray, thin platy & blocky, massive, non-calcareous, common sand-size nodules, no fossils	Littoral
XZ16-11	225.2	HYC LC	Siltstone	Dark gray, thick platy & blocky, massive, abundant burrows, common disseminated plant debris, sparse amorphous OM	Profundal
XZ16-10	223.3	HYC LC	Siltstone	Greenish gray, thick platy, massive, non-calcareous, common plant remains & fish scale, sparse burrows & mud clasts	Prodeltatic
XZ16-9	222.3	HYC LC	Siltstone	Gray, thick platy & blocky, massive, non-calcareous, common amorphous OM & trace plant remains	Prodeltatic
XZ16-8	216.7	HYC LC	Siltstone	Dark gray, blocky, weakly thick parallel bedding, sparse amorphous OM & trace plant remains	Sub-littoral
XZ16-7	214.7	HYC LC	Siltstone	Gray, thick platy & blocky, weakly laminated, cross bedding, wavy & lenticular ripples, common burrows & plant remains	Sub-littoral
XZ16-6	212.1	HYC LC	Siltstone	Black, thick platy & blocky, massive, no fossils	Sub-littoral
XZ16-5	208.4	HYC LC	Siltstone	Black, thick platy & blocky, massive, non-calcareous, trace plant remains,	Sub-littoral
XZ15-32	171.3	LCG LC	Limestone	Black, cobble size micritic nodules in shales, with dead oils	Littoral
XZ15-33	163.5	LCG LC	Dolomitic shale	Blackish gray, fissile-thin platy, sub-mm well parallel laminated, no fossils	Littoral
XZ15-34	155.4	LCG LC	Dolomitic shale	Blackish gray, platy, weakly parallel & wavy laminated, lenticular ripples, common mud pellets, dolomitic, no fossils	Sub-littoral
XZ15-8	151.2	LCG LC	Dolostone	Dark gray, thick blocky, massive & algal laminated, abundant amorphous OM & phytoclasts, diagenesis	Littoral
XZ15-7	150.9	LCG LC	Dolomitic shale	Black, thin platy, parallel & algal laminated, abundant amorphous OM, phytoclasts & ostracods, fossiliferous,	Littoral
XZ15-6	150.7	LCG LC	Limestone & shale	Black, thick blocky, mm-laminated, parallel & wavy laminae are rich in amorphous OM, trace plant remains	Sub-littoral
XZ15-5	150.3	LCG LC	Shale	Black, thin platy, sub-mm-laminated, parallel, planar, & continuous laminae, sparse plant remains & trace fossils	Profundal
XZ15-4	150.1	LCG LC	Dolomitic shale	Black, thin platy, sub-mm-laminated, parallel-planar laminae, tabular cross-bedding, sparse fish scale & plant remains	Littoral
XZ15-3	149.9	LCG LC	Limestone	Blackish gray, thick blocky, thick bedding, oolitic, common fossil fragments & plant remains	Sub-littoral
XZ15-2	149.7	LCG LC	Shale	Black, thin platy, sub-mm parallel laminated, abundant ostracods & common plant remains, imbricated mud clasts	Profundal

Table S1. Sedimentary characteristics of samples in north Tarlong (cont.)

Sample	Meters over base of LCG (m)	Low-Order Cycle	Lithology	Sedimentary Textures & Structures	Depositional Environments
XZ15-1	149.3	LCG LC	Siltstone & sandstone	Gray, interbedded lithic arenite, thick platy, weakly parallel laminated, calcareous, sparse plant remains along bedding	Lakeplain
XZ15-15	148.2	LCG LC	Dolomitic shale	Dark gray, platy, parallel & wavy laminated, abundant plant remains & debris, with sparse amorphous OM	Littoral
XZ15-14	147.9	LCG LC	Limestone	Dark gray, platy, parallel laminated, algal mounds, abundant pyrite & plant remains & debris along laminae	Su-littoral
XZ15-13	147.7	LCG LC	Shale	Black, fissile, sub-mm laminated, X-bedding, plant remains	Profundal
XZ15-12	147.4	LCG LC	Dolomitic shale	Black, fissile-thin platy, mm parallel & algal laminated, dehydration ripples, micro-faults, abundant plant remains	Littoral
XZ15-11	147.2	LCG LC	Limestone	Reddish gray, dense, blocky, micritic, stramatolitic, algal laminated, abundant amorphous OM & sparse plant remains	Sub-littoral
XZ15-10	146.8	LCG LC	Shale	Black, medium platy, sub-mm parallel planar, curved, & wavy laminated, erosional surface, plant remains & amorphous OM	Profundal
XZ15-9	146.2	LCG LC	Siltstone & sandstone	Mottled, interbedded lithic arenite, common burrows, sparse root mottles, abundant plant remains along bedding	Lake plain
XZ15-16	133.7	LCG LC	Dolomitic shale	Black, interlaminated thin platy, sub-mm parallel & wavy laminated, wavy, lenticular, & climbing ripples, no fossils	Littoral
XZ15-17	122.1	LCG LC	Dolomitic shale	Dark gray, platy, mm parallel, wavy, & algal laminated, cross bedding, wavy & dehydration ripples, dolomitic, no fossils	Littoral
XZ15-18	117.9	LCG LC	Dolomitic shale	Purplish gray, platy, sub-mm wavy & algal laminated, lenticular ripples, abundant amorphous OM & plant remains	Littoral
XZ15-19	111.3	LCG LC	Shale	Black, platy, parallel & wavy laminated, no fossils	Littoral
XZ15-20	108.4	LCG LC	Dolomitic shale	Black, fissile, sub-mm well parallel laminated, wavy ripples, dolomitic, common plant remains & amorphous OM	Littoral
XZ15-21	99.4	LCG LC	Dolomitic shale	Black, thin-medium platy, sub-mm parallel laminated & massive, lenticular ripples, dolomitic, no fossils	Profundal
XZ15-22	93.9	LCG LC	Dolomitic shale	Black, thick platy-fissile, sub-mm parallel & wavy laminated, dolomitic, abundant amorphous OM & plant remains	Sub-littoral
XZ15-23	86.2	LCG LC	Dolomitic shale	Black, thin-medium platy, mm- parallel and wavy laminated, large mud pellet, abundant amorphous OM & plant remains	Sub-littoral
XZ15-24	75.5	LCG LC	Dolomitic shale	Black, mm parallel laminated, medium-thick platy, lenticular & climbing ripples, common plant remains & amorphous OM	Sub-littoral
XZ15-25	67.1	LCG LC	Dolomitic shale	Black, mm- parallel and wavy laminated, thin platy-fissile, dolomitic, common plant remains & amorphous OM	Profundal
XZ15-26	64.1	LCG LC	Shale	Black, sub-mm laminated, fissile to blocky, non-calcareous, common plant remains & amorphous OM	Littoral
XZ15-27	42.0	LCG LC	Dolomitic shale	Black, sub-mm parallel laminated, medium-thick platy, dolomitic, sub-mm gray micrite, no fossils	Sub-littoral
XZ15-28	38.8	LCG LC	Calcareous shale	Black to dark gray, fissile-platy, algal laminated, slightly calcareous, abundant plant debris & amorphous OM	Profundal
XZ15-29	33.8	LCG LC	Calcareous shale	Black, sub-mm laminated, thin platy, whole fish fossils, common plant remains, varved deposits with dropstone	Profundal
XZ15-30	26.6	LCG LC	Shale	Black, thick wavy and contorted laminated, non-calcareous, common burrows and trace fossils, abundant plant remains	Prodeltaic
XZ15-31	23.2	LCG LC	Shale	Dark gray- black, thin, massive, interbedded well-laminated, fossiliferous molds, abundant ostracods & plant remains	Littoral
XZ15-35	13.8	LCG LC	Shale	Greenish gray, thick platy, well-laminated, non-calcareous, no fossils observed	Prodeltaic

Table S2. Sedimentary characteristics of samples in south Tarlong

Sample	Meters over base of LCG (m)	Low-Order Cycle	Lithology	Sedimentary Textures & Structures	Depositional Environments
XZ16-24	186.6	HYC LC	Siltstone	Brownish gray, fissile, mainly massive, weakly thin laminated, non-calcareous, common plant remains, bioturbated	Sub-littoral-profundal
XZ16-23	185.4	HYC LC	Siltstone	Purplish gray, thin platy, non-calcareous, mainly massive, weakly thin laminated, sparse dendritic pyrite & plant remains	Sub-littoral
XZ16-22	175.7	HYC LC	Siltstone	Yellowish & greenish gray, blocky, mainly massive, uniformly well thick laminated, common plant remains & burrows	Prodeltaic-profundal
XZ16-21	169.6	HYC LC	Siltstone	Black, thick platy, mainly massive, weakly laminated, bioturbated, trace fossils	Prodeltaic-profundal
XZ16-20	167.4	HYC LC	Siltstone	Black, thick platy, mainly massive, weakly laminated, sparse imbricated sand-size clasts, non-calcareous, no fossils	Prodeltaic-profundal
XZ16-19	165.7	HYC LC	Siltstone	Black, thin platy, mainly massive, weakly laminated, non-calcareous, possible fish scale, no other fossils	Prodeltaic-profundal
XZ16-18	163.8	HYC LC	Siltstone	Black, thin platy, mainly massive, sub-mm weakly laminated, parallel & wavy laminae, sparse plant remains	Prodeltaic-profundal
XZ16-17	163.2	HYC LC	Dolomitic shale	Black, thick platy, sub-mm to mm well parallel laminated, sparse plant remains, amorphous OM, & fossil debris	Prodeltaic-profundal
XZ15-46	108.3	LCG LC	Shale	Black, well parallel & algal laminated, massive, abundant fossil fragments, amorphous OM & plant remains, bituminous	Profundal
XZ15-45	103.7	LCG LC	Shale	Black, medium platy, blocky, massive & weakly laminated, dolomitic (?), abundant plant remains, sparse amorphous OM	Prodeltaic
XZ15-44	99.1	LCG LC	Shale	Black, papery, sub-mm laminated, abundant plant remains	Prodeltaic
XZ15-43	95.7	LCG LC	Shale	Dark gray, thin platy, parallel laminated, tuffaceous, no fossils	Prodeltaic
XZ15-42	89.0	LCG LC	Shale	Black, very well laminated, parallel & planar laminae, calcite cemented, tabular lenses, bituminous, sparse plant remains	Profundal
XZ15-41	79.7	LCG LC	Shale	Black, papery-thin platy, sub-mm parallel laminated, common plant remains, rip up clasts in sand size	Prodeltaic
XZ15-40	63.9	LCG LC	Shale	Black, sub-mm well laminated, large burrows in cm-size, common ostracods & amorphous OM, sparse plant remains	Sub-littoral
XZ15-39	47.7	LCG LC	Shale	Black, papery, mm- well parallel laminated, moderately calcareous, abundant plant remains on bedding plane	Prodeltaic
XZ15-38	40.6	LCG LC	Shale	Blackish gray, mm parallel & wavy laminated, algal laminated, X-bedding, common plant remains & amorphous OM	Sub-littoral
XZ15-37	36.8	LCG LC	Shale	Interlaminated black & greenish, thin platy, parallel laminated, common plant remains & amorphous OM on bedding plane	Sub-littoral
XZ15-36	9.5	LCG LC	Siltstone	Dark gray, thin platy, massive, weakly laminated, no fossils	Sub-littoral

Table S3. Sedimentary characteristics of samples in northwest Tarlong

Sample	Meters over base of LCG (m)	Low-Order Cycle	Lithology	Sedimentary Textures & Structures	Depositional Environments
XZ15-63	193.8	LCG LC	Shale	Black, weakly calcareous, platy, well parallel & wavy laminated, abundant plant & amorphous remains, fish scale	Profundal
XZ15-62	190.2	LCG LC	Shale	Dark gray, platy, sub-mm well parallel laminated, abundant plant remains & sparse amorphous OM on bedding plane	Prodeltaic
XZ15-61	179.8	LCG LC	Shale	Greenish gray, non to moderately calcareous, thin platy, sub-mm to mm laminated & massive, trace plant remains	Profundal
XZ15-60	168.7	LCG LC	Shale	Black, non-calcareous, fissile, sub-mm to mm parallel & wavy laminated, extremely abundant plant remains on bedding	Profundal
XZ15-59	159.5	LCG LC	Shale	Black, thick platy, parallel, wavy, & algal laminated, erosional surface, imbricated mud clasts, sparse algae & plant remains	Profundal
XZ15-58	149.6	LCG LC	Dolomitic shale	Black, variably dolomitic, thick platy, well laminated, no fossils	Profundal
XZ15-57	144.5	LCG LC	Shale	Black-blackish gray, non-calcareous, thin platy, very well parallel laminated & massive, no fossils	Profundal
XZ15-56	133.9	LCG LC	Shale	Black, non-calcareous, thin platy, sub-mm to mm parallel laminated, abundant plant remains & sparse amorphous OM	Profundal
XZ15-55	115.2	LCG LC	Calcareous shale	Black, variably silt, calcareous, thin platy, sub-mm to mm laminated, common mm-cm plant remains & fossil debris	Profundal
XZ15-54	109.8	LCG LC	Calcareous shale	Blackish gray, thick platy, sub-mm to mm parallel laminated,, calcareous, plant remains & ostracods on bedding, dead oil	Littoral
XZ15-53	100.5	LCG LC	Calcareous shale	Black, thick platy, thin well laminated, moderately calcareous, scattered fossil debris & plant remains on bedding plane	Profundal
XZ15-52	93.7	LCG LC	Shale	Black, thick platy, mm parallel laminated, sparse mud clasts, extremely abundant ostracods, plant remains on bedding	Profundal
XZ15-51	80.3	LCG LC	Shale	Black, thin platy, sub-mm to mm parallel & wavy laminated, algal laminae, common plant remains & sparse ostracods	Littoral
XZ15-50	73.2	LCG LC	Dolomitic shale	Dark gray, thin platy-fissile, mm parallel & wavy laminated, dolomitic, common plant remains, algae, & trace fish scale	Littoral
XZ15-49	54.4	LCG LC	Siltstone	Dark gray, papery to blocky, massive, weakly laminated, algal mounds, abundant plant debris & common amorphous OM	Prodeltaic
XZ15-48	16.6	LCG LC	Calcareous shale	Blackish gray, thin platy, sub-mm to mm parallel & wavy laminated, calcareous, abundant plant & amorphous remains	Sub-littoral
XZ15-47	13.6	LCG LC	Shale	Black, thin platy, sub-mm parallel laminated, non-calcareous, varved deposits with dropstone , common plant remains	Profundal

Table S4. Sedimentary characteristics of samples in southwest Tarlong

Sample	Meters over base of LCG (m)	Low-Order Cycle	Lithology	Sedimentary Textures & Structures	Depositional Environments
XZ16-4	100.7	HYC LC	Siltstone	Reddish gray, thick platy, mainly massive, weakly laminated, sub-mm laminae, non-calcareous, common plant remains	Profundal
XZ16-3	94.5	HYC LC	Calcareous shale	Dark gray, thin platy, sub-mm well parallel & wavy laminated, common ostracods, plant remains & amorphous OM	Profundal
XZ16-2	89.2	HYC LC	Dolomitic shale	Blackish gray, dolomitic, thin platy, sub-mm well parallel laminated, minor imbricated elongated grains, abundant plant remains & algae, minor conchostracons & fish scale	Profundal
XZ16-1	86.9	HYC LC	Lime mudstone	Dark gray organic-rich lime mudstone, thin platy, wavy laminated, climbing ripples, rare plant debris & fish scale	Profundal
XZ15-70	73.2	LCG LC	Siltstone	Yellowish gray, lithic arenite, well sorted, sub-rounded to rounded, thin well bedded, massive, X-bedded, no fossils	Littoral
XZ15-69	68.1	LCG LC	Siltstone	Yellowish green, blocky, sandy & silty, mainly massive, weakly laminated, slightly calcareous, rare ostracods	Profundal-prodeltaic
XZ15-68	63.8	LCG LC	Conglomerate	Reddish gray, poorly cemented, clast supported, pebble to cobble, sub-angular to sub-rounded clasts, plant remains	Delta front
XZ15-67	53.8	LCG LC	Siltstone-sandstone	Grayish purple, very fine lithic arenite, well sorted, thick platy & blocky, well bedded & laminated, X-bedding, no fossils	Littoral
XZ15-66	43.8	LCG LC	Siltstone	Purplish gray, very fine lithic subarenite, thick platy, mm well parallel laminated, sparse plant remains on bedding plane	Littoral
XZ15-65	34.3	LCG LC	Shale	Dark gray, thin platy, well laminated, abundant ostracods	Profundal
XZ15-64	21.3	LCG LC	Shale	Greenish gray, silty but dominantly pure, blocky, massive, weakly laminated, common limestone nodules, no fossils	Profundal

Table S5. Sedimentary characteristics of samples in Taodonggou

Sample	Meters over base of LCG (m)	Low-Order Cycle	Lithology	Sedimentary Textures & Structures	Depositional Environments
XZ16-27	127.7	HYC LC	Siltstone	Black to purplish gray, platy-papery, massive, wavy & lenticular laminated, ostracods, fish scale, & plant remains	Sub-littoral
XZ16-26	121.3	HYC LC	Shale siltstone	Yellowish to grayish green, thick platy, well parallel & wavy laminated, lenticular black laminae, common ostracods	Sub-littoral
XZ16-25	116.4	HYC LC	Siltstone	Greenish gray, weakly calcareous, thick platy, mainly massive, weakly mm parallel laminated, trace ostracods	Littoral
XZ15-98	72.2	LCG LC	Calcareous shale	Dark purplish gray, thin platy, intercalated with siltstone, moderately calcareous, well laminated, no fossils	Littoral
XZ15-97	55.8	LCG LC	Shale	Brownish-greenish gray, thin platy-fissile, weakly laminated, basal siltstone-sandstone contain superficial ooids	Littoral
XZ15-96	22.1	LCG LC	Shale	Reddish gray, variably silty, thin platy-fissile, intercalated medium-coarse arenite to sub-arenite, no fossils	Sub-littoral
XZ15-95	4.8	LCG LC	Shale	Purplish-greenish gray, micritic, platy-fissile, massive, sub-mm laminated, sparse burrow cast, rare ostracods & bivalves	Sub-littoral

Table S6. Sedimentary characteristics of samples in Zhaobishan

Sample	Meters over base of LCG (m)	Low-Order Cycle	Lithology	Sedimentary Textures & Structures	Depositional Environments
XZ16-40	164.4	HYC LC	Siltstone	Greenish gray, variably silt, uniform, thick platy & blocky, massive, abundant plant remains, rare trace fossils	Delta front
XZ16-39	161.7	HYC LC	Siltstone	Black, non-calcareous, pure, uniform, thick blocky, massive, & weakly laminated, common plant remains & ostracods	Prodelta
XZ16-38	158.2	HYC LC	Siltstone	Black, non-calcareous, pure, uniform, thick blocky, massive, & weakly laminated, abundant plant remains, trace fossils	Prodelta
XZ16-37	154.9	HYC LC	Siltstone	Black, non-calcareous, pure, thin platy, mainly massive, weakly parallel & wavy & algal laminated, sparse algal & common plant debris	Prodelta
XZ16-36	152.2	HYC LC	Siltstone	Black, non-calcareous, pure, uniform, thick platy, mainly massive, weakly algal laminated, abundant plant remains	Prodelta
XZ16-35	149.9	HYC LC	Siltstone	Black, non-calcareous, pure, uniform, thick blocky, massive, & weakly laminated, sparse micro fossils & plant remains	Profundal
XZ16-34	147.8	HYC LC	Siltstone	Black, non-calcareous, pure, uniform, thick platy, massive & weakly laminated, sparse ostracods & plant remains	Profundal
XZ16-32	134.6	HYC LC	Siltstone	Black, variably silty, thin platy, massive & weakly thin parallel laminated, scattered fossil debris & plant remains	Profundal
XZ16-31	133.2	HYC LC	Siltstone	Black, pure, silty, thick platy, massive & weakly laminated, scattered fossil debris & plant remains	Profundal
XZ16-30	121.9	HYC LC	Siltstone	Black, non-calcareous, thick platy & blocky, mainly massive, weakly wavy laminated, abundant ostracods with fish-hook-like terminations of a single valve, sparse plant remains & amorphous OM	Prodelta
XZ16-29	120.5	HYC LC	Siltstone	Black, thick platy, dense, pure, uniform, slightly calcareous, massive & weakly laminated, sparse plant remains	Profundal
XZ16-28	106.4	HYC LC	Siltstone	Dark gray, variably silty, well sorted, thick platy & blocky, massive, weakly laminated, common plant debris & remains	Prodelta
SZ14-68	105.4	HYC LC	Siltstone & sandstone	Greenish grey, variably silty to very fine sandy, well sorted, thick platy and blocky, massive, no fossils or plant remains	Prodelta
SZ14-67	101.3	HYC LC	Siltstone	Black, pure, silty, uniform, thick platy, massive, dolomitic	Profundal
SZ14-66	100.0	HYC LC	Siltstone	Black, pure, silty, uniform, thick platy, mainly massive, weakly laminated, a few scattered plant remains along laminae	Prodelta
SZ14-65	98.7	HYC LC	Siltstone	Black, pure, silty, uniform, thick platy, mainly massive, weakly sub-mm laminated, weakly dolomitic, scattered plant remains	Profundal
SZ14-64	97.2	HYC LC	Siltstone	Black, pure, silty, uniform, thin platy, mainly massive, weakly sub-mm laminated, weakly dolomitic, scattered plant remains	Profundal
SZ14-63	95.8	HYC LC	Siltstone	Greenish grey, silty, well sorted, massive, dolomitic, no fossils	Prodelta
XZ16-62	85.6	LCG LC	Siltstone	Greenish gray, thick blocky, massive, weakly laminated, scattered sand-size grains, rounded, abundant plant remains	Sublittoral
XZ16-61	69.9	LCG LC	Limestone	Gray wackestone, internally thrombolitic, forming stromatolite or algal mounds, abundant mm-size ooids & skeletal grains	Delta front
XZ16-60	69.7	LCG LC	Shale	Black, thin platy, weakly algal laminated, scattered fine to coarse sandy grains, well rounded, common amorphous OM	Delta front
XZ16-59	69.1	LCG LC	Limestone	Dark gray lime mudstone & wackestone, thick blocky, massive, weakly discontinuous laminated, reworked skeletal grains in 2 mm, common phytoclasts & mud clasts	Littoral
XZ16-58	68.9	LCG LC	Shale	Black, thick platy, sub-mm parallel & wavy laminated, tabular X-bedding, abundant phytoclasts & trace amorphous OM	Delta front
XZ16-57	68.8	LCG LC	Shale	Black, thick platy, thin to thick parallel & wavy laminated, massive, lenticular ripples, flaser beddings, trace phytoclasts	Delta front
XZ16-56	68.7	LCG LC	Limestone	Dark gray, blocky, thick algal laminated & massive, highly recrystallized dolomite, sparse skeletal fragments	Littoral
XZ16-55	48.4	LCG LC	Limestone	Black, thick blocky, algal mounds, intercalated with shale	Littoral
XZ16-54	48.0	LCG LC	Siltstone	Black, thin platy, massive & weakly laminated, no fossils	Sublittoral

Table S6. Sedimentary characteristics of samples in Zhaobishan (cont.)

Sample	Meters over base of LCG (m)	Low-Order Cycle	Lithology	Sedimentary Textures & Structures	Depositional Environments
XZ16-53	47.7	LCG LC	Limestone	Black, lime mudstone, thick platy & blocky, sub-mm well parallel laminated & massive, partially recrystallized	Littoral
XZ16-52	47.4	LCG LC	Siltstone	Gray coarse siltstone & very fine sandstone, well sorted, parallel & wavy laminated & massive, common plant remains	Delta front
XZ16-51	47.2	LCG LC	Siltstone	Gray coarse siltstone & very fine sandstone, well sorted, mm parallel & wavy laminated & massive, common plant remains	Delta front
XZ16-50	46.8	LCG LC	Siltstone	Yellowish brown lithic subarenite/arenite, very fine sandy, well sorted, weakly laminated & massive, common plant remains	Delta front
XZ16-49	34.7	LCG LC	Limestone	Dark gray wackestone & dolostone, cone-in-cone structure	Profundal
XZ16-48	33.5	LCG LC	Shale	Black, pure to silty, thin platy, massive, thick wavy laminated & massive, weakly calcareous, distinctive flaser beddings, common plant remains & amorphous OM	Delta front
XZ16-47	31.4	LCG LC	Shale	Black thick platy, sub-mm parallel & wavy laminated, non-calcareous, abundant plant & amorphous remains on bedding	Profundal
XZ16-46	28.3	LCG LC	Shale	Blackish gray, fissile & thick platy, massive & mm laminated, non-calcareous, scattered microfossils & plant remains	Profundal
XZ16-45D	23.4	LCG LC	Limestone	Black wackestone, internally thrombolitic, well algal laminated, sparse plant remain & trace skeletal grains	Delta front
XZ16-45C	23.3	LCG LC	Limestone	Black wackestone, internally thrombolitic, forming stromatolite or algal mounds, algal laminated, trace skeletal grains	Delta front
XZ16-45B	23.2	LCG LC	Limestone	Black lime mudstone & wackestone, thick platy, extremely abundant pisolitic, oncoids & skeletal grains in silt size	Delta front
XZ16-45A	23.1	LCG LC	Limestone	Black wackestone, internally thrombolitic, forming stromatolite or algal mounds, abundant mm-size ooids & skeletal grains	Delta front
XZ16-44	16.6	LCG LC	Limestone	Black well laminated large oolitic grainstone, 0-20 cm thick, mm well rounded & coated ooids, reworked skeletal grains	Delta front
XZ16-43B	12.4	LCG LC	Limestone	Black lime mudstone, thick blocky, interlaminated micritic & grainer laminae, abundant skeletal fragments & plant remains	Profundal
XZ16-43A	12.3	LCG LC	Limestone	Black lime mudstone & wackestones, thick algal laminated & massive, variably silty to sandy, common plant remains	Profundal
XZ16-42B	7.8	LCG LC	Limestone	black wackestone, algal mounds, sub-mm to mm algal laminated, lower part dolomitic shale, mm parallel laminated	Profundal
XZ16-42A	7.5	LCG LC	Limestone	Black wackestone, algal mounds, thick laminated & thin bedded, algal laminated, scattered plant debris & ooids	Profundal
XZ16-41	1.4	LCG LC	Siltstone	Dark gray, coarsening upward to very-fine lithic wacke, calcareous, massive, well laminated & bedded, no fossils	Prodeltaic

Table S7. Geochemical characteristics of samples in north Tarlong

Sample NO.	TOC (wt%)*	C/N†	$\delta^{13}\text{C}_{\text{org}}$ (‰)§	<i>n</i> -Alkanes (%)#			TAR **	CPI† †	OEP §§	Pr/Ph#	$\beta/n\text{-C}_{17}^{**}$ *	Regular Steranes (%)†††			Diast. Index§ §§	C_{27} Dia/ (Dia+Reg.)###	$\text{C}_{29} \beta\beta/(\beta\beta + \alpha\alpha)$ *****	Ga. Index† †††	Homo. Index‡ ‡‡‡	C_{30} Hop. / C_{29} Reg.****	Ts/(Ts +Tm) ††††
				S	M	L						C_{27}	C_{28}	C_{29}							
XZ16-16	0.47	19.56	-21.23	N/A	N/A	N/A	N/A	N/A	N/A	N/A	N/A	22	27	51	0.64	0.53	0.24	N/A	N/A	N/A	N/A
XZ16-15	4.61	30.98	-22.78	35	55	10	0.26	1.82	1.54	3.77	0.00	55	33	12	6.48	0.27	0.73	0.00	0.00	56.47	0.11
XZ16-14	3.88	31.57	-22.47	31	42	27	0.86	1.40	1.32	2.67	0.00	34	21	45	0.49	0.35	0.18	0.00	0.16	2.33	0.20
XZ16-13	4.55	31.97	-21.84	39	46	15	0.34	1.42	1.35	2.62	0.00	43	21	36	0.85	0.37	0.17	0.00	0.00	1.37	0.12
XZ16-12	3.46	31.06	-21.90	40	40	20	0.47	1.43	1.31	2.68	0.00	39	23	38	0.85	0.39	0.23	0.00	0.27	2.35	0.13
XZ16-11	2.87	31.77	-21.57	40	41	19	0.49	1.58	1.45	2.68	0.00	35	27	38	0.62	0.34	0.23	0.00	0.23	2.36	0.11
XZ16-10	0.26	17.90	-22.54	N/A	N/A	N/A	N/A	N/A	N/A	N/A	N/A	28	32	40	0.36	0.27	0.27	N/A	N/A	N/A	N/A
XZ16-9	1.71	29.43	-23.00	35	47	18	0.50	1.38	1.20	3.12	0.00	40	24	36	0.27	0.17	0.12	0.00	0.00	5.71	0.06
XZ16-8	1.21	31.14	-22.37	24	60	16	0.54	1.50	1.32	3.14	0.00	32	19	49	0.29	0.26	0.17	0.00	0.00	8.44	0.11
XZ16-7	1.49	32.66	-23.30	27	46	27	0.84	1.40	1.38	3.38	0.00	28	19	53	0.19	0.22	0.25	0.00	0.00	4.19	0.12
XZ16-6	4.67	35.93	-23.59	36	50	14	0.32	1.37	1.28	3.03	0.00	40	19	41	0.48	0.28	0.18	0.00	0.16	7.07	0.12
XZ16-5	3.60	31.84	-24.01	44	43	13	0.29	1.39	1.25	3.50	0.00	39	22	39	0.53	0.31	0.18	0.00	0.00	4.62	0.08
XZ15-32	7.86	50.92	-27.33	35	49	16	0.37	1.30	1.21	1.96	0.00	30	29	41	0.25	0.18	0.37	0.79	0.21	9.58	0.59
XZ15-33	5.12	47.10	-26.11	46	47	7	0.13	1.47	1.36	1.63	0.00	25	37	38	0.20	0.15	0.41	0.89	0.27	9.58	0.66
XZ15-34	4.23	53.44	-26.80	29	56	15	0.41	1.38	1.31	1.68	0.00	26	39	34	0.35	0.20	0.44	1.02	0.34	4.89	0.74
XZ15-8	6.49	36.38	-28.64	42	49	9	0.19	1.41	1.27	1.88	0.00	38	35	27	0.40	0.14	0.46	1.38	0.48	4.71	0.66
XZ15-7	1.31	42.53	-25.90	29	50	21	0.59	1.32	1.28	1.47	0.01	42	34	24	0.42	0.12	0.47	1.34	0.23	5.67	0.63
XZ15-6	3.12	46.26	-26.10	50	40	10	0.17	1.24	1.22	1.45	0.01	39	32	29	0.35	0.13	0.41	1.48	0.32	4.48	0.60

Table S7. Geochemical characteristics of samples in north Tarlong (cont.)

Sample NO.	TOC (wt%)*	C/N†	$\delta^{13}\text{C}_{\text{org}}$ (‰)§	<i>n</i> -Alkanes (%)#			TAR **	CPI†	OEP §§	Pr/Ph#	$\beta/n\text{-C}_{17}^{**}$ *	Regular Steranes (%)†††			Diast. Index§§	C_{27} Dia/ (Dia+Reg.)###	$\text{C}_{29} \beta\beta/(\beta\beta + \alpha\alpha)$ *****	Ga. Index†††	Homo. Index‡‡‡	C_{30} Hop. / C_{29} Reg. ****	Ts/(Ts +Tm) ††††
				S	M	L						C_{27}	C_{28}	C_{29}							
XZ15-5	2.92	43.33	-24.99	40	43	17	0.39	1.31	1.40	1.57	0.00	38	35	27	0.20	0.09	0.35	0.96	0.50	1.87	0.45
XZ15-4	6.11	49.90	-27.28	45	47	8	0.15	1.38	1.28	1.64	0.00	33	32	35	0.28	0.15	0.40	1.75	0.00	5.54	0.68
XZ15-3	0.74	39.49	-25.62	33	54	13	0.31	1.37	1.34	1.62	0.00	37	30	33	0.34	0.15	0.43	1.42	0.00	5.92	0.61
XZ15-2	3.45	46.52	-24.44	43	45	12	0.24	1.35	1.29	1.45	0.00	32	33	35	0.28	0.15	0.43	1.48	0.08	7.00	0.64
XZ15-1	0.34	25.87	-21.88	35	42	23	0.67	1.46	1.37	1.38	0.00	37	30	33	0.49	0.18	0.51	N/A	N/A	2.66	0.38
XZ15-15	3.01	48.71	-27.16	32	46	22	0.57	1.28	1.26	1.44	0.00	30	34	36	0.43	0.14	0.41	1.34	0.22	6.95	0.67
XZ15-14	0.89	42.17	-26.14	29	51	20	0.56	1.31	1.26	1.67	0.00	27	37	36	0.30	0.17	0.47	1.36	N/A	6.26	0.73
XZ15-13	4.77	39.95	-25.51	25	44	31	1.08	1.38	1.33	1.58	0.00	45	29	26	0.54	0.18	0.30	2.17	0.46	4.81	0.59
XZ15-12	5.85	46.55	-29.59	34	51	15	0.38	1.31	1.25	1.54	0.00	26	42	32	0.27	0.16	0.44	1.54	0.31	7.13	0.69
XZ15-11	1.49	42.67	-25.13	30	53	17	0.46	1.31	1.16	1.81	0.00	31	36	33	0.20	0.12	0.36	1.25	N/A	25.06	0.76
XZ15-10	2.81	47.84	-26.77	42	45	13	0.30	1.28	1.25	1.45	0.00	32	35	33	0.35	0.17	0.43	1.39	0.48	7.47	0.70
XZ15-9	0.25	26.39	-22.73	20	30	50	2.51	2.14	1.56	1.25	0.00	27	22	51	0.11	0.12	0.36	N/A	0.00	1.68	0.22
XZ15-16	1.35	38.61	-25.98	28	47	25	0.72	1.41	1.39	1.47	0.00	37	33	30	0.11	0.05	0.44	0.48	0.29	2.09	0.68
XZ15-17	8.27	44.56	-26.60	42	44	14	0.31	1.39	1.31	1.52	0.00	31	35	34	0.19	0.11	0.44	1.26	0.55	5.60	0.72
XZ15-18	0.86	40.77	-24.79	32	42	26	0.71	1.38	1.37	1.21	0.00	36	34	30	0.39	0.15	0.46	1.29	0.34	5.22	0.52
XZ15-19	5.05	43.86	-27.10	N/A	N/A	N/A	N/A	N/A	N/A	1.03	0.00	38	28	34	0.26	0.13	0.40	2.56	N/A	1.89	0.31
XZ15-20	4.24	48.49	-26.45	52	34	14	0.24	1.33	1.39	1.46	0.00	41	32	27	0.35	0.11	0.49	1.79	0.32	4.00	0.62
XZ15-21	5.49	47.24	-27.31	39	45	16	0.39	1.35	1.37	1.41	0.00	42	31	27	0.54	0.17	0.42	1.21	0.31	4.99	0.67
XZ15-22	3.63	45.93	-25.96	44	43	14	0.27	1.25	1.31	1.73	0.00	36	38	26	0.37	0.12	0.48	0.89	0.29	6.38	0.67

Table S7. Geochemical characteristics of samples in north Tarlong (cont.)

Sample NO.	TOC (wt%)*	C/N†	$\delta^{13}\text{C}_{\text{org}}$ (‰)§	<i>n</i> -Alkanes (%)#			TAR **	CPI†	OEP §§	Pr/Ph#	$\beta/n\text{-C}_{17}^{**}$	Regular Steranes (%)†††			Diast. Index§§	C ₂₇ Dia/(Dia+Reg.)###	C ₂₉ $\beta\beta/(\beta\beta+\alpha\alpha)$ ****	Ga. Index†††	Homo. Index‡‡‡	C ₃₀ Hop./C ₂₉ Reg.*****	Ts/(Ts+Tm)††††
				S	M	L						C ₂₇	C ₂₈	C ₂₉							
XZ15-23	4.47	49.45	-26.15	55	34	11	0.21	1.51	1.62	1.56	0.00	41	33	26	0.50	0.14	0.49	2.37	N/A	3.14	0.42
XZ15-24	4.67	52.73	-27.32	N/A	N/A	N/A	N/A	N/A	N/A	N/A	N/A	N/A	N/A	N/A	N/A	N/A	N/A	N/A	N/A	N/A	N/A
XZ15-25	3.53	46.91	-25.55	52	36	12	0.25	1.50	1.52	1.41	0.00	45	31	24	0.29	0.08	0.43	2.10	N/A	3.72	0.27
XZ15-26	3.26	35.77	-26.92	38	40	22	0.48	1.29	1.29	1.75	0.01	43	29	28	0.38	0.14	0.34	2.09	0.32	2.72	0.43
XZ15-27	6.33	41.50	-25.95	42	36	22	0.44	1.41	1.49	1.39	0.00	49	29	22	0.51	0.11	0.49	2.65	N/A	3.97	0.59
XZ15-28	2.61	40.06	-25.27	36	40	24	0.68	1.33	1.27	1.10	0.00	22	40	38	0.25	0.23	0.30	2.05	0.28	3.70	0.34
XZ15-29	2.15	39.21	-25.09	41	41	18	0.49	1.52	1.44	1.99	0.00	35	24	41	0.20	0.12	0.39	2.14	0.38	22.77	0.63
XZ15-30	0.11	N/A	-21.89	32	34	34	1.17	1.78	1.47	0.89	0.00	N/A	N/A	N/A	N/A	N/A	N/A	N/A	N/A	N/A	N/A
XZ15-31	0.26	N/A	-22.28	38	41	21	0.53	1.47	1.46	2.35	0.00	28	26	46	0.17	0.18	0.23	1.28	0.57	3.37	0.18
XZ15-35	0.04	N/A	N/A	40	49	11	0.32	1.84	2.14	1.79	0.00	36	31	33	0.41	0.18	0.41	N/A	0.21	4.72	0.67

* Total organic carbon content.

† Content of carbon over nitrogen (C/N) in kerogen

§ Organic carbon isotope ratio, determined based on delta notation (‰) relative to the Vienna Pee Dee Belemnite (V-PDB) standard.

Peak areas of *n*-alkanes in TIC traces chromatogram: S – short chain (C₁₂-C₁₉), M – mid-chain (C₂₀-C₂₅), L – long chain *n*-alkanes (C₂₆-C₃₄).** Peak areas of *n*-alkanes: TAR = (C₂₇ + C₂₉ + C₃₁)/(C₁₅ + C₁₇ + C₁₉).†† Peak areas of *n*-alkanes: CPI = [(C₂₅ + C₂₇ + C₂₉ + C₃₁)/(C₂₄ + C₂₆ + C₂₈ + C₃₀) + (C₂₅ + C₂₇ + C₂₉ + C₃₁)/(C₂₆ + C₂₈ + C₃₀ + C₃₂)]/2.§§ Peak areas of *n*-alkanes: OEP = (C₂₅ + 6 × C₂₇ + C₂₉)/[4 × (C₂₆ + C₂₈)].

Peak areas of isoprenoid in TIC traces from GC for acquiring ratio of pristane/phytane (Pr/Ph).

*** β -carotane in m/z 125 and 558 chromatogram for ratio of β -carotane/C₁₇ *n*-alkane ($\beta/n\text{-C}_{17}$).††† Peak areas of 5 α (H),14 α (H),17 α (H),(20R + 20S) and 5 α (H),14 β (H),17 β (H),(20R + 20S) of C₂₇ cholestanes, C₂₈ methylcholestanes, and C₂₉ ethylcholestanes calculated in m/z 217 chromatogram and normalized to a total of 100%.§§§ Diasteranes index (Diast. Index) was calculated by peak areas of C₂₇ 13 β (H),17 α (H),(20R + 20S)-diacholestanes over sum of C₂₉ 5 α (H),14 α (H),17 α (H),(20R + 20S)-24-ethylcholestanes in m/z 217 chromatogram.#### C₂₇ diasteranes/(C₂₇ diasteranes + C₂₇ regular steranes) was calculated by peak areas of C₂₇ 13 β (H),17 α (H),(20R + 20S)-diacholestanes over sum of C₂₇ 13 β (H),17 α (H),(20R + 20S)-diacholestanes, C₂₇ 5 α (H),14 α (H),17 α (H),(20R + 20S) cholestanes, and C₂₇ 5 α (H),14 β (H),17 β (H),(20R + 20S) cholestanes in m/z 217 chromatogram.**** Ratio of 5 α (H),14 β (H),17 β (H),(20R + 20S) C₂₉ ethylcholestanes over sum of 5 α (H),14 α (H),17 α (H),(20R + 20S) and 5 α (H),14 β (H),17 β (H),(20R + 20S) of C₂₉ ethylcholestanes in m/z 217 chromatogram.†††† Peak areas in m/z 191 chromatogram: gammacerane index (Ga. Index) = 10 × gammacerane/(gammacerane + C₃₀ 17 α (H),21 β (H)-hopane).§§§§ Homohopane index (Homo. Index) was calculated using peak areas of C₃₅ 17 α (H),21 β (H),(22R + 22S)-pentakishomohopanes over peak areas of C₃₃ counterparts in m/z 191 chromatogram.***** C₃₀ $\alpha\beta$ -hopane/C₂₉ regular steranes (C₃₀ Hop. /C₂₉ Reg.) was calculated as ratio of C₃₀ 17 α (H),21 β (H)-hopane over sum of 5 α (H),14 α (H),17 α (H),(20R + 20S) and 5 α (H),14 β (H),17 β (H),(20R + 20S) of C₂₉ ethylcholestanes.††††† Peak areas in m/z 191 chromatogram, Tm – 17 α -22,29,30-trisnorhopane-C₂₇; Ts – 8 α -22,29,30-trisnorhopane-C₂₇.††††† Ratio of C₃₀ 17 β (H),21 α (H)-moretane over sum of C₃₀ 17 β (H),21 α (H)-moretane and C₃₀ 17 α (H),21 β (H)-hopanes in m/z 191 chromatogram.

N/A = not applicable.

Table S8. Geochemical characteristics of samples in south Tarlong

Sample NO.	TOC (wt%)*	C/N†	$\delta^{13}\text{C}_{\text{org}}$ (‰)§	<i>n</i> -Alkanes (%)#			TAR **	CPI† †	OEP §§	Pr/Ph#	$\beta/n\text{-C}_{17}^{**}$ *	Regular Steranes (%)†††			Diast. Index§ §§	C_{27} Dia/ (Dia+Reg.)###	$\text{C}_{29} \beta\beta/(\beta\beta + \alpha\alpha)$ ****	Ga. Index† ††	Homo. Index‡ ###	C_{30} Hop. / C_{29} Reg. ****	Ts/(Ts +Tm) ††††
				S	M	L						C_{27}	C_{28}	C_{29}							
XZ16-24	0.07	N/A	-23.27	31	50	19	N/A	N/A	N/A	N/A	N/A	N/A	N/A	N/A	N/A	N/A	N/A	N/A	N/A	N/A	N/A
XZ16-23	0.09	N/A	-21.07	39	45	16	N/A	N/A	N/A	N/A	N/A	N/A	N/A	N/A	N/A	N/A	N/A	N/A	N/A	N/A	N/A
XZ16-22	0.34	21.09	-21.58	38	50	12	N/A	N/A	N/A	N/A	N/A	N/A	N/A	N/A	N/A	N/A	N/A	N/A	N/A	N/A	N/A
XZ16-21	1.42	30.85	-22.46	33	52	15	0.52	1.33	1.24	2.00	0.00	37	52	11	4.60	0.34	0.60	0.00	0.10	34.91	0.09
XZ16-20	3.35	30.95	-21.50	29	57	14	0.37	1.30	1.19	2.52	0.00	68	25	7	6.95	0.32	0.36	0.00	0.00	32.41	N/A
XZ16-19	5.23	36.38	-22.94	31	50	19	0.26	1.21	1.22	2.85	0.00	30	26	44	0.78	0.47	0.23	0.00	0.18	3.61	0.10
XZ16-18	3.34	35.86	-23.69	39	45	16	0.38	1.42	1.31	2.32	0.00	22	27	51	0.64	0.53	0.24	0.00	0.00	7.19	0.11
XZ16-17	1.93	25.07	-22.10	38	50	12	0.40	1.69	1.75	3.39	0.00	N/A	N/A	N/A	N/A	N/A	N/A	N/A	N/A	N/A	N/A
XZ15-46	3.29	44.15	-23.41	47	41	12	0.21	1.34	1.23	1.73	0.00	31	32	37	0.25	0.16	0.35	1.69	0.31	9.34	0.63
XZ15-45	2.99	44.78	-24.60	43	40	17	0.33	1.30	1.20	1.53	0.00	26	38	36	0.30	0.21	0.36	1.53	0.47	10.79	0.70
XZ15-44	2.15	44.20	-24.03	50	39	11	0.20	1.39	1.31	2.07	0.00	35	33	32	0.26	0.14	0.35	1.31	0.24	7.66	0.62
XZ15-43	4.22	38.59	-25.09	40	48	12	0.26	1.39	1.32	1.65	0.00	30	34	36	0.18	0.13	0.37	1.40	0.18	8.64	0.57
XZ15-42	4.11	43.26	-24.61	48	41	11	0.20	1.21	1.17	1.45	0.00	27	36	37	0.35	0.24	0.33	1.61	0.12	10.44	0.57
XZ15-41	3.44	42.47	-24.70	58	34	8	0.16	1.45	1.23	2.01	0.00	22	42	36	0.13	0.12	0.37	2.70	0.25	13.75	0.60
XZ15-40	3.35	44.19	-25.21	41	43	16	0.31	1.24	1.25	1.65	0.00	25	38	37	0.18	0.14	0.37	1.36	0.17	8.03	0.57
XZ15-39	2.36	44.59	-25.70	41	43	16	0.34	1.28	1.17	1.97	0.00	42	29	29	0.44	0.15	0.42	0.98	0.44	10.67	0.59

Table S8. Geochemical characteristics of samples in south Tarlong (cont.)

Sample NO.	TOC (wt%)*	C/N†	$\delta^{13}\text{C}_{\text{org}}$ (‰)§	<i>n</i> -Alkanes (%)#			TAR **	CPI†	OEP §§	Pr/Ph#	$\beta/n\text{-C}_{17}^{***}$	Regular Steranes (%)†††			Diast. Index§§	C_{27} Dia/(Dia+Reg.)###	$\text{C}_{29} \beta\beta/(\beta\beta + \alpha\alpha)$ *****	Ga. Index†	Homo. Index‡	C_{30} Hop./ C_{29} Reg.****	Ts/(Ts + Tm)††††
				S	M	L						C_{27}	C_{28}	C_{29}							
XZ15-38	0.40	N/A	-24.80	24	48	28	0.98	1.27	1.21	1.08	0.00	36	34	30	0.43	0.19	0.32	2.14	0.44	13.08	0.67
XZ15-37	2.44	43.20	-25.48	43	43	14	0.28	1.24	1.27	1.75	0.00	37	31	32	0.44	0.21	0.34	2.28	0.18	5.83	0.60
XZ15-36	0.04	N/A	-26.19	N/A	N/A	N/A	N/A	N/A	N/A	N/A	N/A	N/A	N/A	N/A	N/A	N/A	N/A	N/A	N/A	N/A	N/A

* Total organic carbon content.

† Content of carbon over nitrogen (C/N) in kerogen

§ Organic carbon isotope ratio, determined based on delta notation (‰) relative to the Vienna Pee Dee Belemnite (V-PDB) standard.

Peak areas of *n*-alkanes in TIC traces chromatogram: S – short chain ($\text{C}_{12}\text{-C}_{19}$), M – mid-chain ($\text{C}_{20}\text{-C}_{25}$), L – long chain *n*-alkanes ($\text{C}_{26}\text{-C}_{34}$).** Peak areas of *n*-alkanes: $\text{TAR} = (\text{C}_{27} + \text{C}_{29} + \text{C}_{31})/(\text{C}_{15} + \text{C}_{17} + \text{C}_{19})$.†† Peak areas of *n*-alkanes: $\text{CPI} = [(\text{C}_{25} + \text{C}_{27} + \text{C}_{29} + \text{C}_{31})/(\text{C}_{24} + \text{C}_{26} + \text{C}_{28} + \text{C}_{30}) + (\text{C}_{25} + \text{C}_{27} + \text{C}_{29} + \text{C}_{31})/(\text{C}_{26} + \text{C}_{28} + \text{C}_{30} + \text{C}_{32})]/2$.§§ Peak areas of *n*-alkanes: $\text{OEP} = (\text{C}_{25} + 6 \times \text{C}_{27} + \text{C}_{29})/[4 \times (\text{C}_{26} + \text{C}_{28})]$.

Peak areas of isoprenoid in TIC traces from GC for acquiring ratio of pristane/phytane (Pr/Ph).

*** β -carotane in m/z 125 and 558 chromatogram for ratio of β -carotane/ C_{17} *n*-alkane ($\beta/n\text{-C}_{17}$).††† Peak areas of $5\alpha(\text{H})$, $14\alpha(\text{H})$, $17\alpha(\text{H})$, (20R + 20S) and $5\alpha(\text{H})$, $14\beta(\text{H})$, $17\beta(\text{H})$, (20R + 20S) of C_{27} cholestanes, C_{28} methylcholestanes, and C_{29} ethylcholestanes calculated in m/z 217 chromatogram and normalized to a total of 100%.§§§ Diasteranes index (Diast. Index) was calculated by peak areas of C_{27} $13\beta(\text{H})$, $17\alpha(\text{H})$, (20R + 20S)-diacholestanes over sum of C_{29} $5\alpha(\text{H})$, $14\alpha(\text{H})$, $17\alpha(\text{H})$, (20R + 20S)-24-ethylcholestanes in m/z 217 chromatogram.### C_{27} diasteranes/(C_{27} diasteranes + C_{27} regular steranes) was calculated by peak areas of C_{27} $13\beta(\text{H})$, $17\alpha(\text{H})$, (20R + 20S)-diacholestanes over sum of C_{27} $13\beta(\text{H})$, $17\alpha(\text{H})$, (20R + 20S)-diacholestanes, C_{27} $5\alpha(\text{H})$, $14\alpha(\text{H})$, $17\alpha(\text{H})$, (20R + 20S) cholestanes, and C_{27} $5\alpha(\text{H})$, $14\beta(\text{H})$, $17\beta(\text{H})$, (20R + 20S) cholestanes in m/z 217 chromatogram.**** Ratio of $5\alpha(\text{H})$, $14\beta(\text{H})$, $17\beta(\text{H})$, (20R + 20S) C_{29} ethylcholestanes over sum of $5\alpha(\text{H})$, $14\alpha(\text{H})$, $17\alpha(\text{H})$, (20R + 20S) and $5\alpha(\text{H})$, $14\beta(\text{H})$, $17\beta(\text{H})$, (20R + 20S) of C_{29} ethylcholestanes in m/z 217 chromatogram.†††† Peak areas in m/z 191 chromatogram: gammacerane index (Ga. Index) = $10 \times \text{gammacerane}/(\text{gammacerane} + \text{C}_{30} \text{ } 17\alpha(\text{H}), 21\beta(\text{H})\text{-hopane})$.§§§§ Homohopane index (Homo. Index) was calculated using peak areas of C_{35} $17\alpha(\text{H}), 21\beta(\text{H})$, (22R + 22S)-pentakishomohopanes over peak areas of C_{33} counterparts in m/z 191 chromatogram.#### $\text{C}_{30} \alpha\beta\text{-hopane}/\text{C}_{29}$ regular steranes (C_{30} Hop. / C_{29} Reg.) was calculated as ratio of C_{30} $17\alpha(\text{H}), 21\beta(\text{H})\text{-hopane}$ over sum of $5\alpha(\text{H})$, $14\alpha(\text{H})$, $17\alpha(\text{H})$, (20R + 20S) and $5\alpha(\text{H})$, $14\beta(\text{H})$, $17\beta(\text{H})$, (20R + 20S) of C_{29} ethylcholestanes.***** Peak areas in m/z 191 chromatogram, Tm – $17\alpha\text{-}22,29,30\text{-trisnorhopane-C}_{27}$; Ts – $8\alpha\text{-}22,29,30\text{-trisnorhopane-C}_{27}$.††††† Ratio of C_{30} $17\beta(\text{H}), 21\alpha(\text{H})\text{-moretane}$ over sum of C_{30} $17\beta(\text{H}), 21\alpha(\text{H})\text{-moretane}$ and C_{30} $17\alpha(\text{H}), 21\beta(\text{H})\text{-hopanes}$ in m/z 191 chromatogram.

N/A = not applicable.

Table S9. Geochemical characteristics of samples in northwest Tarlong

Sample NO.	TOC (wt%)*	C/N†	$\delta^{13}\text{C}_{\text{org}}$ (‰)§	<i>n</i> -Alkanes (%)#			TAR **	CPI† †	OEP §§	Pr/Ph#	$\beta/n\text{-C}_{17}^{**}$ *	Regular Steranes (%)†††			Diast. Index§ §§	C_{27} Dia/ (Dia+Reg.)###	$\text{C}_{29} \beta\beta/(\beta\beta + \alpha\alpha)$ *****	Ga. Index† ††	Homo. Index‡ ‡‡‡	C_{30} Hop. / C_{29} Reg. ****	Ts/(Ts +Tm) ††††
				S	M	L						C_{27}	C_{28}	C_{29}							
XZ15-63	1.69	N/A	-23.43	20	57	23	0.75	1.10	1.04	1.87	0.00	29	37	34	0.19	0.13	0.32	N/A	N/A	2.91	0.55
XZ15-62	1.17	38.35	-24.52	36	44	20	0.49	1.62	1.58	2.05	0.00	31	39	30	0.16	0.10	0.32	1.01	0.24	2.81	0.44
XZ15-61	0.40	32.03	-26.20	32	52	16	0.44	1.39	1.35	1.72	0.00	34	31	35	0.21	0.13	0.32	1.55	N/A	4.42	0.26
XZ15-60	14.30	52.61	-28.92	35	58	7	0.16	1.45	1.30	2.04	0.00	25	39	36	0.18	0.15	0.31	2.12	N/A	11.86	0.59
XZ15-59	5.28	44.46	-25.34	45	47	8	0.16	1.40	1.32	1.93	0.00	25	34	41	0.18	0.17	0.32	1.64	0.17	8.19	0.70
XZ15-58	4.90	41.23	-25.65	39	48	13	0.26	1.41	1.39	1.50	0.00	24	36	40	0.17	0.16	0.29	1.51	0.28	3.55	0.53
XZ15-57	3.39	40.53	-25.42	41	47	12	0.23	1.39	1.28	1.60	0.00	24	39	37	0.17	0.15	0.30	1.95	0.19	6.28	0.52
XZ15-56	4.43	46.81	-26.73	41	42	17	0.38	1.49	1.35	1.28	0.00	20	43	37	0.18	0.19	0.29	2.54	0.24	12.37	0.60
XZ15-55	5.56	42.34	-26.96	34	46	20	0.47	1.45	1.35	1.26	0.01	21	46	33	0.14	0.14	0.28	1.99	0.18	9.69	0.59
XZ15-54	3.34	47.92	-26.98	23	50	27	0.99	1.40	1.38	1.68	0.01	23	43	34	0.19	0.16	0.34	1.52	0.12	8.08	0.69
XZ15-53	5.72	42.80	-26.18	51	38	11	0.23	1.43	1.30	2.16	0.00	29	36	35	0.26	0.17	0.34	1.46	0.19	8.77	0.62
XZ15-52	4.20	49.53	-27.38	39	45	16	0.33	1.25	1.13	1.49	0.00	39	36	25	0.36	0.13	0.33	1.65	0.26	5.36	0.54
XZ15-51	2.56	47.06	-26.78	35	45	20	0.53	1.36	1.36	1.61	0.00	40	30	30	0.57	0.21	0.40	1.86	N/A	4.07	0.49
XZ15-50	2.92	42.55	-26.37	49	39	12	0.22	1.37	1.32	1.82	0.00	39	27	34	0.35	0.17	0.34	2.06	0.27	5.30	0.67
XZ15-49	0.19	N/A	-22.16	32	45	23	0.73	1.64	1.54	2.01	0.00	33	29	38	0.30	0.20	0.29	2.02	0.25	13.81	0.57

Table S9. Geochemical characteristics of samples in northwest Tarlong (cont.)

Sample NO.	TOC (wt%)*	C/N†	$\delta^{13}\text{C}_{\text{org}}$ (‰)§	<i>n</i> -Alkanes (%)#			TAR **	CPI†	OEP §§	Pr/Ph#	$\beta/n\text{-C}_{17}^{**}$	Regular Steranes (%)†††			Diast. Index§§	C_{27} Dia/ (Dia+R eg.)###	$\text{C}_{29} \beta\beta/(\beta\beta + \alpha\alpha)$ *****	Ga. Index†	Homo. Index‡	C_{30} Hop. / C_{29} Reg. ****	Ts/(Ts +Tm) ††††
				S	M	L						C_{27}	C_{28}	C_{29}							
XZ15-48	0.71	39.26	-23.63	21	51	28	1.08	1.44	1.37	1.85	0.00	19	33	48	0.09	0.15	0.21	1.03	0.23	4.65	0.28
XZ15-47	3.24	45.23	-25.74	24	46	30	1.16	1.59	1.52	1.99	0.00	23	27	50	0.10	0.14	0.25	0.71	0.34	8.40	0.53

* Total organic carbon content.

† Content of carbon over nitrogen (C/N) in kerogen

§ Organic carbon isotope ratio, determined based on delta notation (‰) relative to the Vienna Pee Dee Belemnite (V-PDB) standard.

Peak areas of *n*-alkanes in TIC traces chromatogram: S – short chain ($\text{C}_{12}\text{-C}_{19}$), M – mid-chain ($\text{C}_{20}\text{-C}_{25}$), L – long chain *n*-alkanes ($\text{C}_{26}\text{-C}_{34}$).** Peak areas of *n*-alkanes: TAR = $(\text{C}_{27} + \text{C}_{29} + \text{C}_{31})/(\text{C}_{15} + \text{C}_{17} + \text{C}_{19})$.†† Peak areas of *n*-alkanes: CPI = $[(\text{C}_{25} + \text{C}_{27} + \text{C}_{29} + \text{C}_{31})/(\text{C}_{24} + \text{C}_{26} + \text{C}_{28} + \text{C}_{30}) + (\text{C}_{25} + \text{C}_{27} + \text{C}_{29} + \text{C}_{31})/(\text{C}_{26} + \text{C}_{28} + \text{C}_{30} + \text{C}_{32})]/2$.§§ Peak areas of *n*-alkanes: OEP = $(\text{C}_{25} + 6 \times \text{C}_{27} + \text{C}_{29})/[4 \times (\text{C}_{26} + \text{C}_{28})]$.

Peak areas of isoprenoid in TIC traces from GC for acquiring ratio of pristane/phytane (Pr/Ph).

*** β -carotane in m/z 125 and 558 chromatogram for ratio of β -carotane/ C_{17} *n*-alkane ($\beta/n\text{-C}_{17}$).††† Peak areas of 5 α (H), 14 α (H), 17 α (H), (20R + 20S) and 5 α (H), 14 β (H), 17 β (H), (20R + 20S) of C_{27} cholestanes, C_{28} methylcholestanes, and C_{29} ethylcholestanes calculated in m/z 217 chromatogram and normalized to a total of 100%.§§§ Diasteranes index (Diast. Index) was calculated by peak areas of C_{27} 13 β (H), 17 α (H), (20R + 20S)-diasteranes over sum of C_{29} 5 α (H), 14 α (H), 17 α (H), (20R + 20S)-24-ethylcholestanes in m/z 217 chromatogram.#### C_{27} diasteranes/(C_{27} diasteranes + C_{27} regular steranes) was calculated by peak areas of C_{27} 13 β (H), 17 α (H), (20R + 20S)-diasteranes over sum of C_{27} 13 β (H), 17 α (H), (20R + 20S)-diasteranes, C_{27} 5 α (H), 14 α (H), 17 α (H), (20R + 20S) cholestanes, and C_{27} 5 α (H), 14 β (H), 17 β (H), (20R + 20S) cholestanes in m/z 217 chromatogram.***** Ratio of 5 α (H), 14 β (H), 17 β (H), (20R + 20S) C_{29} ethylcholestanes over sum of 5 α (H), 14 α (H), 17 α (H), (20R + 20S) and 5 α (H), 14 β (H), 17 β (H), (20R + 20S) of C_{29} ethylcholestanes in m/z 217 chromatogram.†††† Peak areas in m/z 191 chromatogram: gammacerane index (Ga. Index) = $10 \times \text{gammacerane}/(\text{gammacerane} + \text{C}_{30} \text{ 17}\alpha(\text{H}), 21\beta(\text{H})\text{-hopane})$.§§§§ Homohopane index (Homo. Index) was calculated using peak areas of C_{35} 17 α (H), 21 β (H), (22R + 22S)-pentakishomohopanes over peak areas of C_{33} counterparts in m/z 191 chromatogram.##### C_{30} $\alpha\beta$ -hopane/ C_{29} regular steranes (C_{30} Hop. / C_{29} Reg.) was calculated as ratio of C_{30} 17 α (H), 21 β (H)-hopane over sum of 5 α (H), 14 α (H), 17 α (H), (20R + 20S) and 5 α (H), 14 β (H), 17 β (H), (20R + 20S) of C_{29} ethylcholestanes.***** Peak areas in m/z 191 chromatogram, Tm – 17 α -22,29,30-trisnorhopane- C_{27} ; Ts – 8 α -22,29,30-trisnorhopane- C_{27} .††††† Ratio of C_{30} 17 β (H), 21 α (H)-moretane over sum of C_{30} 17 β (H), 21 α (H)-moretane and C_{30} 17 α (H), 21 β (H)-hopanes in m/z 191 chromatogram.

N/A = not applicable.

Table S10. Geochemical characteristics of samples in southwest Tarlong

Sample NO.	TOC (wt%)*	C/N†	$\delta^{13}\text{C}_{\text{org}}$ (‰)§	<i>n</i> -Alkanes (%)#			TAR **	CPI†	OEP §§	Pr/Ph#	$\beta/n\text{-C}_{17}^{***}$	Regular Steranes (%)†††			Diast. Index§§	C_{27} Dia/ (Dia+Reg.)###	$\text{C}_{29} \beta\beta/(\beta\beta + \alpha\alpha)$ ****	Ga. Index†	Homo. Index‡	C_{30} Hop. / C_{29} Reg. ****	Ts/(Ts +Tm) ††††
				S	M	L						C_{27}	C_{28}	C_{29}							
XZ16-4	0.12	N/A	N/A	25	44	31	1.34	1.64	1.57	1.79	0.08	24	33	43	0.39	0.33	0.30	0.00	0.00	4.04	0.42
XZ16-3	5.98	40.92	-24.42	21	43	36	1.40	1.33	1.31	1.82	0.39	29	29	42	0.30	0.25	0.23	1.13	0.17	5.35	0.43
XZ16-2	4.13	42.55	-23.74	38	40	22	0.58	1.45	1.46	1.66	0.15	27	31	42	0.32	0.27	0.25	1.08	0.22	1.97	0.39
XZ16-1	1.96	36.10	-23.64	40	45	15	0.32	1.55	1.44	3.46	0.00	40	17	43	0.39	0.25	0.21	0.00	0.00	3.28	0.18
XZ15-70	0.03	N/A	N/A	29	51	20	0.37	0.85	0.80	1.29	0.00	30	36	34	0.26	0.17	0.30	1.32	0.46	23.98	0.58
XZ15-69	0.45	N/A	N/A	36	48	16	0.34	0.98	0.84	1.58	0.00	33	32	35	0.24	0.13	0.41	N/A	N/A	N/A	0.50
XZ15-68	0.01	N/A	N/A	34	46	20	0.52	1.24	1.04	1.53	0.00	N/A	N/A	N/A	N/A	N/A	N/A	N/A	N/A	N/A	0.63
XZ15-67	0.04	N/A	N/A	21	68	11	0.37	1.47	1.49	1.45	0.00	33	33	34	0.24	0.13	0.39	1.01	N/A	7.90	0.63
XZ15-66	0.01	N/A	N/A	N/A	N/A	N/A	N/A	N/A	N/A	N/A	N/A	N/A	N/A	N/A	N/A	N/A	N/A	N/A	N/A	N/A	N/A
XZ15-65	0.06	N/A	N/A	34	55	11	0.27	1.27	1.25	1.58	0.00	33	34	33	0.43	0.18	0.50	N/A	N/A	N/A	0.35
XZ15-64	0.04	N/A	-22.67	36	39	25	0.86	2.31	2.28	1.07	0.00	27	34	39	0.41	0.24	0.46	N/A	N/A	2.50	0.47

* Total organic carbon content. † Content of carbon over nitrogen (C/N) in kerogen

§ Organic carbon isotope ratio, determined based on delta notation (‰) relative to the Vienna Pee Dee Belemnite (V-PDB) standard.

Peak areas of *n*-alkanes in TIC traces chromatogram: S – short chain (C_{12} – C_{19}), M – mid-chain (C_{20} – C_{25}), L – long chain *n*-alkanes (C_{26} – C_{34}).** Peak areas of *n*-alkanes: TAR = $(\text{C}_{27} + \text{C}_{29} + \text{C}_{31})/(\text{C}_{15} + \text{C}_{17} + \text{C}_{19})$.†† Peak areas of *n*-alkanes: CPI = $[(\text{C}_{25} + \text{C}_{27} + \text{C}_{29} + \text{C}_{31})/(\text{C}_{24} + \text{C}_{26} + \text{C}_{28} + \text{C}_{30}) + (\text{C}_{25} + \text{C}_{27} + \text{C}_{29} + \text{C}_{31})/(\text{C}_{26} + \text{C}_{28} + \text{C}_{30} + \text{C}_{32})]/2$.§§ Peak areas of *n*-alkanes: OEP = $(\text{C}_{25} + 6 \times \text{C}_{27} + \text{C}_{29})/[4 \times (\text{C}_{26} + \text{C}_{28})]$.## Peak areas of isoprenoid in TIC traces from GC for acquiring ratio of pristane/phytane (Pr/Ph). *** β -carotane in m/z 125 and 558 chromatogram for ratio of β -carotane/ C_{17} *n*-alkane ($\beta/n\text{-C}_{17}$).††† Peak areas of 5 α ,14 α ,17 α , (20R + 20S) and 5 α ,14 β ,17 β , (20R + 20S) of C_{27} cholestanes, C_{28} methylcholestanes, and C_{29} ethylcholestanes calculated in m/z 217 chromatogram and normalized to 100%.§§§ Diasteranes index was calculated by peak areas of C_{27} 13 β (H),17 α (H), (20R + 20S)-diacholestanes over sum of C_{29} 5 α (H),14 α (H),17 α (H), (20R + 20S)-24-ethylcholestanes in m/z 217 chromatogram.### C_{27} diasteranes/ $(\text{C}_{27}$ diasteranes + C_{27} regular steranes) was calculated by peak areas of C_{27} 13 β (H),17 α (H), (20R + 20S)-diacholestanes over sum of C_{27} 13 β (H),17 α (H), (20R + 20S)-diacholestanes, C_{27} 5 α (H),14 α (H),17 α (H), (20R + 20S) cholestanes, and C_{27} 5 α (H),14 β (H),17 β (H), (20R + 20S) cholestanes in m/z 217 chromatogram.**** Ratio of 5 α (H),14 β (H),17 β (H), (20R + 20S) C_{29} ethylcholestanes over sum of 5 α (H),14 α (H),17 α (H), (20R + 20S) and 5 α (H),14 β (H),17 β (H), (20R + 20S) of C_{29} ethylcholestanes in m/z 217 chromatogram.†††† Peak areas in m/z 191 chromatogram: gammacerane index (Ga. Index) = $10 \times \text{gammacerane}/(\text{gammacerane} + \text{C}_{30} \text{ 17}\alpha(\text{H}),21\beta(\text{H})\text{-hopane})$.§§§§ Homohopane index (Homo. Index) was calculated using peak areas of C_{35} 17 α (H),21 β (H), (22R + 22S)-pentakishomohopanes over peak areas of C_{33} counterparts in m/z 191 chromatogram.#### C_{30} $\alpha\beta$ -hopane/ C_{29} regular steranes was calculated as C_{30} 17 α (H),21 β (H)-hopane over sum of 5 α (H),14 α (H),17 α (H), (20R + 20S) and 5 α (H),14 β (H),17 β (H), (20R + 20S) of C_{29} ethylcholestanes.***** Peak areas in m/z 191 chromatogram, Tm – 17 α -22,29,30-trisnorhopane- C_{27} ; Ts – 8 α -22,29,30-trisnorhopane- C_{27} .††††† Ratio of C_{30} 17 β (H),21 α (H)-moretane over sum of C_{30} 17 β (H),21 α (H)-moretane and C_{30} 17 α (H),21 β (H)-hopanes in m/z 191 chromatogram.

N/A = not applicable.

Table S11. Geochemical characteristics of samples in Taodonggou

Sample NO.	TOC (wt%)*	C/N†	$\delta^{13}\text{C}_{\text{org}}$ (‰)§	<i>n</i> -Alkanes (%)#			TAR **	CPI†	OEP §§	Pr/Ph#	$\beta/n\text{-C}_{17}^{**}$	Regular Steranes (%)†††			Diast. Index§§	C_{27} Dia/ (Dia+R eg.)###	$\text{C}_{29} \beta\beta/(\beta\beta + \alpha\alpha)$ *****	Ga. Index†	Homo. Index‡	C_{30} Hop. / C_{29} Reg. ****	Ts/(Ts +Tm) ††††
				S	M	L						C_{27}	C_{28}	C_{29}							
XZ16-27	0.10	N/A	N/A	N/A	N/A	N/A	N/A	N/A	N/A	N/A	N/A	N/A	N/A	N/A	N/A	N/A	N/A	N/A	N/A	N/A	N/A
XZ16-26	0.08	N/A	N/A	N/A	N/A	N/A	N/A	N/A	N/A	N/A	N/A	N/A	N/A	N/A	N/A	N/A	N/A	N/A	N/A	N/A	N/A
XZ16-25	0.08	N/A	N/A	N/A	N/A	N/A	N/A	N/A	N/A	N/A	N/A	N/A	N/A	N/A	N/A	N/A	N/A	N/A	N/A	N/A	N/A
XZ15-98	0.03	N/A	N/A	25	57	18	0.60	1.37	1.24	1.49	0.00	37	32	31	0.47	0.18	0.44	N/A	N/A	7.72	0.49
XZ15-97	0.03	N/A	N/A	41	40	19	0.42	1.34	1.47	1.61	0.01	45	33	22	0.42	0.10	0.47	1.68	0.24	3.49	0.47
XZ15-96	0.03	N/A	N/A	16	52	32	1.36	1.10	1.05	1.58	0.00	26	38	36	0.12	0.10	0.30	1.44	0.21	3.41	0.50
XZ15-95	0.07	N/A	N/A	33	56	11	0.25	1.37	1.18	1.15	0.00	29	37	34	0.34	0.19	0.42	N/A	N/A	N/A	0.49

* Total organic carbon content.

† Content of carbon over nitrogen (C/N) in kerogen

§ Organic carbon isotope ratio, determined based on delta notation (‰) relative to the Vienna Pee Dee Belemnite (V-PDB) standard.

Peak areas of *n*-alkanes in TIC traces chromatogram: S – short chain ($\text{C}_{12}\text{-C}_{19}$), M – mid-chain ($\text{C}_{20}\text{-C}_{25}$), L – long chain *n*-alkanes ($\text{C}_{26}\text{-C}_{34}$).** Peak areas of *n*-alkanes: $\text{TAR} = (\text{C}_{27} + \text{C}_{29} + \text{C}_{31})/(\text{C}_{15} + \text{C}_{17} + \text{C}_{19})$.†† Peak areas of *n*-alkanes: $\text{CPI} = [(\text{C}_{25} + \text{C}_{27} + \text{C}_{29} + \text{C}_{31})/(\text{C}_{24} + \text{C}_{26} + \text{C}_{28} + \text{C}_{30}) + (\text{C}_{25} + \text{C}_{27} + \text{C}_{29} + \text{C}_{31})/(\text{C}_{26} + \text{C}_{28} + \text{C}_{30} + \text{C}_{32})]/2$.§§ Peak areas of *n*-alkanes: $\text{OEP} = (\text{C}_{25} + 6 \times \text{C}_{27} + \text{C}_{29})/[4 \times (\text{C}_{26} + \text{C}_{28})]$.

Peak areas of isoprenoid in TIC traces from GC for acquiring ratio of pristane/phytane (Pr/Ph).

*** β -carotane in m/z 125 and 558 chromatogram for ratio of β -carotane/ C_{17} *n*-alkane ($\beta/n\text{-C}_{17}$).††† Peak areas of $5\alpha(\text{H})$, $14\alpha(\text{H})$, $17\alpha(\text{H})$, (20R + 20S) and $5\alpha(\text{H})$, $14\beta(\text{H})$, $17\beta(\text{H})$, (20R + 20S) of C_{27} cholestanes, C_{28} methylcholestanes, and C_{29} ethylcholestanes calculated in m/z 217 chromatogram and normalized to a total of 100%.§§§ Diasteranes index (Diast. Index) was calculated by peak areas of C_{27} $13\beta(\text{H})$, $17\alpha(\text{H})$, (20R + 20S)-diacholestanes over sum of C_{29} $5\alpha(\text{H})$, $14\alpha(\text{H})$, $17\alpha(\text{H})$, (20R + 20S)-24-ethylcholestanes in m/z 217 chromatogram.### C_{27} diasteranes/(C_{27} diasteranes + C_{27} regular steranes) was calculated by peak areas of C_{27} $13\beta(\text{H})$, $17\alpha(\text{H})$, (20R + 20S)-diacholestanes over sum of C_{27} $13\beta(\text{H})$, $17\alpha(\text{H})$, (20R + 20S)-diacholestanes, C_{27} $5\alpha(\text{H})$, $14\alpha(\text{H})$, $17\alpha(\text{H})$, (20R + 20S) cholestanes, and C_{27} $5\alpha(\text{H})$, $14\beta(\text{H})$, $17\beta(\text{H})$, (20R + 20S) cholestanes in m/z 217 chromatogram.**** Ratio of $5\alpha(\text{H})$, $14\beta(\text{H})$, $17\beta(\text{H})$, (20R + 20S) C_{29} ethylcholestanes over sum of $5\alpha(\text{H})$, $14\alpha(\text{H})$, $17\alpha(\text{H})$, (20R + 20S) and $5\alpha(\text{H})$, $14\beta(\text{H})$, $17\beta(\text{H})$, (20R + 20S) of C_{29} ethylcholestanes in m/z 217 chromatogram.†††† Peak areas in m/z 191 chromatogram: gammacerane index (Ga. Index) = $10 \times \text{gammacerane}/(\text{gammacerane} + \text{C}_{30} \text{ } 17\alpha(\text{H})$, $21\beta(\text{H})$ -hopane).§§§§ Homohopane index (Homo. Index) was calculated using peak areas of C_{35} $17\alpha(\text{H})$, $21\beta(\text{H})$, (22R + 22S)-pentakishomohopanes over peak areas of C_{33} counterparts in m/z 191 chromatogram.***** C_{30} $\alpha\beta$ -hopane/ C_{29} regular steranes (C_{30} Hop. / C_{29} Reg.) was calculated as ratio of C_{30} $17\alpha(\text{H})$, $21\beta(\text{H})$ -hopane over sum of $5\alpha(\text{H})$, $14\alpha(\text{H})$, $17\alpha(\text{H})$, (20R + 20S) and $5\alpha(\text{H})$, $14\beta(\text{H})$, $17\beta(\text{H})$, (20R + 20S) of C_{29} ethylcholestanes.***** Peak areas in m/z 191 chromatogram, Tm – 17α -22,29,30-trisnorhopane- C_{27} ; Ts – 8α -22,29,30-trisnorhopane- C_{27} .††††† Ratio of C_{30} $17\beta(\text{H})$, $21\alpha(\text{H})$ -moretane over sum of C_{30} $17\beta(\text{H})$, $21\alpha(\text{H})$ -moretane and C_{30} $17\alpha(\text{H})$, $21\beta(\text{H})$ -hopanes in m/z 191 chromatogram.

N/A = not applicable.

Table S12. Geochemical characteristics of samples in Zhaobishan

Sample NO.	TOC (wt%)*	C/N†	$\delta^{13}\text{C}_{\text{org}}$ (‰)§	<i>n</i> -Alkanes (%)#			TAR **	CPI† †	OEP §§	Pr/Ph#	$\beta/n\text{-C}_{17}^{**}$ *	Regular Steranes (%)†††			Diast. Index§ §§	C_{27} Dia/ (Dia+Reg.)###	$\text{C}_{29} \beta\beta/(\beta\beta + \alpha\alpha)$ ****	Ga. Index† †††	Homo. Index‡ ###	C_{30} Hop. / C_{29} Reg.****	Ts/(Ts +Tm) ††††
				S	M	L						C_{27}	C_{28}	C_{29}							
XZ16-40	2.52	N/A	-23.83	N/A	N/A	N/A	N/A	N/A	N/A	N/A	N/A	N/A	N/A	N/A	N/A	N/A	N/A	N/A	N/A	N/A	N/A
XZ16-39	2.52	44.66	-23.59	N/A	N/A	N/A	N/A	N/A	N/A	N/A	N/A	N/A	N/A	N/A	N/A	N/A	N/A	N/A	N/A	N/A	N/A
XZ16-38	1.37	47.12	-22.26	N/A	N/A	N/A	N/A	N/A	N/A	N/A	N/A	N/A	N/A	N/A	N/A	N/A	N/A	N/A	N/A	N/A	N/A
XZ16-37	2.01	51.17	-23.35	N/A	N/A	N/A	N/A	N/A	N/A	N/A	N/A	N/A	N/A	N/A	N/A	N/A	N/A	N/A	N/A	N/A	N/A
XZ16-36	2.70	53.37	-22.97	N/A	N/A	N/A	N/A	N/A	N/A	N/A	N/A	N/A	N/A	N/A	N/A	N/A	N/A	N/A	N/A	N/A	N/A
XZ16-35	4.83	53.26	-21.62	N/A	N/A	N/A	N/A	N/A	N/A	N/A	N/A	N/A	N/A	N/A	N/A	N/A	N/A	N/A	N/A	N/A	N/A
XZ16-34	3.38	51.87	-22.48	N/A	N/A	N/A	N/A	N/A	N/A	N/A	N/A	N/A	N/A	N/A	N/A	N/A	N/A	N/A	N/A	N/A	N/A
XZ16-32	1.39	47.11	-22.17	N/A	N/A	N/A	N/A	N/A	N/A	N/A	N/A	N/A	N/A	N/A	N/A	N/A	N/A	N/A	N/A	N/A	N/A
XZ16-31	3.18	49.14	-24.03	N/A	N/A	N/A	N/A	N/A	N/A	N/A	N/A	N/A	N/A	N/A	N/A	N/A	N/A	N/A	N/A	N/A	N/A
XZ16-30	0.83	44.42	-22.00	N/A	N/A	N/A	N/A	N/A	N/A	N/A	N/A	N/A	N/A	N/A	N/A	N/A	N/A	N/A	N/A	N/A	N/A
XZ16-29	4.08	51.12	-24.13	N/A	N/A	N/A	N/A	N/A	N/A	N/A	N/A	N/A	N/A	N/A	N/A	N/A	N/A	N/A	N/A	N/A	N/A
XZ16-28	2.24	46.73	-22.29	N/A	N/A	N/A	N/A	N/A	N/A	N/A	N/A	N/A	N/A	N/A	N/A	N/A	N/A	N/A	N/A	N/A	N/A
SZ14-68	N/A	N/A	N/A	N/A	N/A	N/A	N/A	N/A	N/A	N/A	N/A	N/A	N/A	N/A	N/A	N/A	N/A	N/A	N/A	N/A	N/A
SZ14-67	N/A	N/A	N/A	N/A	N/A	N/A	N/A	N/A	N/A	N/A	N/A	N/A	N/A	N/A	N/A	N/A	N/A	N/A	N/A	N/A	N/A
SZ14-66	N/A	N/A	N/A	N/A	N/A	N/A	N/A	N/A	N/A	N/A	N/A	N/A	N/A	N/A	N/A	N/A	N/A	N/A	N/A	N/A	N/A
SZ14-65	N/A	N/A	N/A	N/A	N/A	N/A	N/A	N/A	N/A	N/A	N/A	N/A	N/A	N/A	N/A	N/A	N/A	N/A	N/A	N/A	N/A
SZ14-64	N/A	N/A	N/A	N/A	N/A	N/A	N/A	N/A	N/A	N/A	N/A	N/A	N/A	N/A	N/A	N/A	N/A	N/A	N/A	N/A	N/A
SZ14-63	N/A	N/A	N/A	N/A	N/A	N/A	N/A	N/A	N/A	N/A	N/A	N/A	N/A	N/A	N/A	N/A	N/A	N/A	N/A	N/A	N/A
XZ16-62	3.24	54.56	-25.35	N/A	N/A	N/A	N/A	N/A	N/A	N/A	N/A	N/A	N/A	N/A	N/A	N/A	N/A	N/A	N/A	N/A	N/A
XZ16-61	0.12	N/A	N/A	N/A	N/A	N/A	N/A	N/A	N/A	N/A	N/A	N/A	N/A	N/A	N/A	N/A	N/A	N/A	N/A	N/A	N/A
XZ16-60	0.23	N/A	N/A	N/A	N/A	N/A	N/A	N/A	N/A	N/A	N/A	N/A	N/A	N/A	N/A	N/A	N/A	N/A	N/A	N/A	N/A

Table S12. Geochemical characteristics of samples in Zhaobishan (cont.)

Sample NO.	TOC (wt%)*	C/N†	$\delta^{13}\text{C}_{\text{org}}$ (‰)§	<i>n</i> -Alkanes (%)#			TAR **	CPI†	OEP §§	Pr/Ph#	$\beta/n\text{-C}_{17}^{**}$ *	Regular Steranes (%)†††			Diast. Index§§	C_{27} Dia/ (Dia+Reg.)###	$\text{C}_{29} \beta\beta/(\beta\beta + \alpha\alpha)$ ****	Ga. Index† †††	Homo. Index‡ ###	C_{30} Hop. / C_{29} Reg. ****	Ts/(Ts +Tm) ††††
				S	M	L						C_{27}	C_{28}	C_{29}							
XZ16-59	0.49	50.82	-24.18	N/A	N/A	N/A	N/A	N/A	N/A	N/A	N/A	N/A	N/A	N/A	N/A	N/A	N/A	N/A	N/A	N/A	N/A
XZ16-58	2.43	52.21	-24.40	N/A	N/A	N/A	N/A	N/A	N/A	N/A	N/A	N/A	N/A	N/A	N/A	N/A	N/A	N/A	N/A	N/A	N/A
XZ16-57	1.05	52.47	-24.67	N/A	N/A	N/A	N/A	N/A	N/A	N/A	N/A	N/A	N/A	N/A	N/A	N/A	N/A	N/A	N/A	N/A	N/A
XZ16-56	0.38	52.13	-24.25	N/A	N/A	N/A	N/A	N/A	N/A	N/A	N/A	N/A	N/A	N/A	N/A	N/A	N/A	N/A	N/A	N/A	N/A
XZ16-55	0.43	52.92	-23.50	N/A	N/A	N/A	N/A	N/A	N/A	N/A	N/A	N/A	N/A	N/A	N/A	N/A	N/A	N/A	N/A	N/A	N/A
XZ16-54	1.95	55.30	-25.15	N/A	N/A	N/A	N/A	N/A	N/A	N/A	N/A	N/A	N/A	N/A	N/A	N/A	N/A	N/A	N/A	N/A	N/A
XZ16-53	1.93	48.84	-24.38	N/A	N/A	N/A	N/A	N/A	N/A	N/A	N/A	N/A	N/A	N/A	N/A	N/A	N/A	N/A	N/A	N/A	N/A
XZ16-52	0.13	N/A	N/A	N/A	N/A	N/A	N/A	N/A	N/A	N/A	N/A	N/A	N/A	N/A	N/A	N/A	N/A	N/A	N/A	N/A	N/A
XZ16-51	1.21	48.88	-24.33	N/A	N/A	N/A	N/A	N/A	N/A	N/A	N/A	N/A	N/A	N/A	N/A	N/A	N/A	N/A	N/A	N/A	N/A
XZ16-50	1.03	61.18	-25.30	N/A	N/A	N/A	N/A	N/A	N/A	N/A	N/A	N/A	N/A	N/A	N/A	N/A	N/A	N/A	N/A	N/A	N/A
XZ16-49	0.78	55.98	-23.69	N/A	N/A	N/A	N/A	N/A	N/A	N/A	N/A	N/A	N/A	N/A	N/A	N/A	N/A	N/A	N/A	N/A	N/A
XZ16-48	0.51	50.55	-23.71	N/A	N/A	N/A	N/A	N/A	N/A	N/A	N/A	N/A	N/A	N/A	N/A	N/A	N/A	N/A	N/A	N/A	N/A
XZ16-47	0.17	N/A	N/A	N/A	N/A	N/A	N/A	N/A	N/A	N/A	N/A	N/A	N/A	N/A	N/A	N/A	N/A	N/A	N/A	N/A	N/A
XZ16-46	0.12	N/A	N/A	N/A	N/A	N/A	N/A	N/A	N/A	N/A	N/A	N/A	N/A	N/A	N/A	N/A	N/A	N/A	N/A	N/A	N/A
XZ16-45D	0.14	N/A	N/A	N/A	N/A	N/A	N/A	N/A	N/A	N/A	N/A	N/A	N/A	N/A	N/A	N/A	N/A	N/A	N/A	N/A	N/A
XZ16-45C	0.13	N/A	N/A	N/A	N/A	N/A	N/A	N/A	N/A	N/A	N/A	N/A	N/A	N/A	N/A	N/A	N/A	N/A	N/A	N/A	N/A
XZ16-45B	0.09	N/A	N/A	N/A	N/A	N/A	N/A	N/A	N/A	N/A	N/A	N/A	N/A	N/A	N/A	N/A	N/A	N/A	N/A	N/A	N/A
XZ16-45A	0.25	N/A	N/A	N/A	N/A	N/A	N/A	N/A	N/A	N/A	N/A	N/A	N/A	N/A	N/A	N/A	N/A	N/A	N/A	N/A	N/A
XZ16-44	0.12	N/A	N/A	N/A	N/A	N/A	N/A	N/A	N/A	N/A	N/A	N/A	N/A	N/A	N/A	N/A	N/A	N/A	N/A	N/A	N/A
XZ16-43B	0.20	36.68	N/A	N/A	N/A	N/A	N/A	N/A	N/A	N/A	N/A	N/A	N/A	N/A	N/A	N/A	N/A	N/A	N/A	N/A	N/A

Table S12. Geochemical characteristics of samples in Zhaobishan (cont.)

Sample NO.	TOC (wt%)*	C/N†	$\delta^{13}\text{C}_{\text{org}}$ (‰)§	<i>n</i> -Alkanes (%)#			TAR **	CPI†	OEP §§	Pr/Ph#	$\beta/n\text{-C}_{17}^{**}$	Regular Steranes (%)†††			Diast. Index§§	C_{27} Dia/ (Dia+R eg.)###	$\text{C}_{29} \beta\beta/(\beta\beta + \alpha\alpha)$ *****	Ga. Index†	Homo. Index‡	C_{30} Hop. / C_{29} Reg. ****	Ts/(Ts +Tm) ††††
				S	M	L						C_{27}	C_{28}	C_{29}							
XZ16-43A	0.09	N/A	-21.55	N/A	N/A	N/A	N/A	N/A	N/A	N/A	N/A	N/A	N/A	N/A	N/A	N/A	N/A	N/A	N/A	N/A	N/A
XZ16-42B	0.18	N/A	N/A	N/A	N/A	N/A	N/A	N/A	N/A	N/A	N/A	N/A	N/A	N/A	N/A	N/A	N/A	N/A	N/A	N/A	N/A
XZ16-42A	0.09	N/A	N/A	N/A	N/A	N/A	N/A	N/A	N/A	N/A	N/A	N/A	N/A	N/A	N/A	N/A	N/A	N/A	N/A	N/A	N/A
XZ16-41	3.24	N/A	N/A	N/A	N/A	N/A	N/A	N/A	N/A	N/A	N/A	N/A	N/A	N/A	N/A	N/A	N/A	N/A	N/A	N/A	N/A

* Total organic carbon content.
† Content of carbon over nitrogen (C/N) in kerogen
§ Organic carbon isotope ratio, determined based on delta notation (‰) relative to the Vienna Pee Dee Belemnite (V-PDB) standard.
Peak areas of *n*-alkanes in TIC traces chromatogram: S – short chain ($\text{C}_{12}\text{-C}_{19}$), M – mid-chain ($\text{C}_{20}\text{-C}_{25}$), L – long chain *n*-alkanes ($\text{C}_{26}\text{-C}_{34}$).
** Peak areas of *n*-alkanes: $\text{TAR} = (\text{C}_{27} + \text{C}_{29} + \text{C}_{31})/(\text{C}_{15} + \text{C}_{17} + \text{C}_{19})$.
†† Peak areas of *n*-alkanes: $\text{CPI} = [(\text{C}_{25} + \text{C}_{27} + \text{C}_{29} + \text{C}_{31})/(\text{C}_{24} + \text{C}_{26} + \text{C}_{28} + \text{C}_{30}) + (\text{C}_{25} + \text{C}_{27} + \text{C}_{29} + \text{C}_{31})/(\text{C}_{26} + \text{C}_{28} + \text{C}_{30} + \text{C}_{32})]/2$.
§§ Peak areas of *n*-alkanes: $\text{OEP} = (\text{C}_{25} + 6 \times \text{C}_{27} + \text{C}_{29})/[4 \times (\text{C}_{26} + \text{C}_{28})]$.
Peak areas of isoprenoid in TIC traces from GC for acquiring ratio of pristane/phytane (Pr/Ph).
*** β -carotane in m/z 125 and 558 chromatogram for ratio of β -carotane/ C_{17} *n*-alkane ($\beta/n\text{-C}_{17}$).
††† Peak areas of $5\alpha(\text{H}), 14\alpha(\text{H}), 17\alpha(\text{H}), (20\text{R} + 20\text{S})$ and $5\alpha(\text{H}), 14\beta(\text{H}), 17\beta(\text{H}), (20\text{R} + 20\text{S})$ of C_{27} cholestanes, C_{28} methylcholestanes, and C_{29} ethylcholestanes calculated in m/z 217 chromatogram and normalized to a total of 100%.
§§§ Diasteranes index (Diast. Index) was calculated by peak areas of $\text{C}_{27} 13\beta(\text{H}), 17\alpha(\text{H}), (20\text{R} + 20\text{S})$ -diacholestanes over sum of $\text{C}_{29} 5\alpha(\text{H}), 14\alpha(\text{H}), 17\alpha(\text{H}), (20\text{R} + 20\text{S})$ -24-ethylcholestanes in m/z 217 chromatogram.
C_{27} diasteranes/ C_{27} diasteranes + C_{27} regular steranes) was calculated by peak areas of $\text{C}_{27} 13\beta(\text{H}), 17\alpha(\text{H}), (20\text{R} + 20\text{S})$ -diacholestanes over sum of $\text{C}_{27} 13\beta(\text{H}), 17\alpha(\text{H}), (20\text{R} + 20\text{S})$ -diacholestanes, $\text{C}_{27} 5\alpha(\text{H}), 14\alpha(\text{H}), 17\alpha(\text{H}), (20\text{R} + 20\text{S})$ cholestanes, and $\text{C}_{27} 5\alpha(\text{H}), 14\beta(\text{H}), 17\beta(\text{H}), (20\text{R} + 20\text{S})$ cholestanes in m/z 217 chromatogram.
**** Ratio of $5\alpha(\text{H}), 14\beta(\text{H}), 17\beta(\text{H}), (20\text{R} + 20\text{S})$ C_{29} ethylcholestanes over sum of $5\alpha(\text{H}), 14\alpha(\text{H}), 17\alpha(\text{H}), (20\text{R} + 20\text{S})$ and $5\alpha(\text{H}), 14\beta(\text{H}), 17\beta(\text{H}), (20\text{R} + 20\text{S})$ of C_{29} ethylcholestanes in m/z 217 chromatogram.
†††† Peak areas in m/z 191 chromatogram: gammacerane index (Ga. Index) = $10 \times \text{gammacerane}/(\text{gammacerane} + \text{C}_{30} 17\alpha(\text{H}), 21\beta(\text{H})\text{-hopane})$.
§§§§ Homohopane index (Homo. Index) was calculated using peak areas of $\text{C}_{35} 17\alpha(\text{H}), 21\beta(\text{H}), (22\text{R} + 22\text{S})$ -pentakishomohopanes over peak areas of C_{33} counterparts in m/z 191 chromatogram.
$\text{C}_{30} \alpha\beta$ -hopane/ C_{29} regular steranes (C_{30} Hop. / C_{29} Reg.) was calculated as ratio of $\text{C}_{30} 17\alpha(\text{H}), 21\beta(\text{H})\text{-hopane}$ over sum of $5\alpha(\text{H}), 14\alpha(\text{H}), 17\alpha(\text{H}), (20\text{R} + 20\text{S})$ and $5\alpha(\text{H}), 14\beta(\text{H}), 17\beta(\text{H}), (20\text{R} + 20\text{S})$ of C_{29} ethylcholestanes.
***** Peak areas in m/z 191 chromatogram, Tm – $17\alpha\text{-}22,29,30\text{-trisnorhopane-C}_{27}$; Ts – $8\alpha\text{-}22,29,30\text{-trisnorhopane-C}_{27}$.
††††† Ratio of $\text{C}_{30} 17\beta(\text{H}), 21\alpha(\text{H})\text{-moretane}$ over sum of $\text{C}_{30} 17\beta(\text{H}), 21\alpha(\text{H})\text{-moretane}$ and $\text{C}_{30} 17\alpha(\text{H}), 21\beta(\text{H})\text{-hopanes}$ in m/z 191 chromatogram.
N/A = not applicable.

REFERENCES

- Allen, J.P., Fielding, C.R., Gibling, M.R., and Rygel, M.C., 2011. Fluvial response to paleo-equatorial climate fluctuations during the late Paleozoic ice age. *Geological Society of America Bulletin* 123, 1524–1538.
- Bennett, M.R., Doyle, P., and Mather, A.E., 1996. Dropstones: their origin and significance. *Palaeogeography, Palaeoclimatology, Palaeoecology* 121, 331–339.
- Birgenheier, L.P., Frank, T.D., Fielding, C.R., and Rygel, M.C., 2010. Coupled carbon isotopic and sedimentological records from the Permian system of eastern Australia reveal the response of atmospheric carbon dioxide to glacial growth and decay during the late Palaeozoic Ice Age. *Palaeogeography, Palaeoclimatology, Palaeoecology* 286, 178–93.
- Boucot, A.J., Xu, C., Scotese, C.R., and Morley, R.J., 2013. *Phanerozoic Paleoclimate: An Atlas of Lithologic Indicators of Climate*. SEPM Concepts in Sedimentology and Paleontology 11. Society for Sedimentary Geology, Tulsa, 478 p.
- Braakman, J.H., Martin, J.H., Potter, T.L., and van Vliet, A., 1982. Late Paleozoic Gondwana glaciation in Oman. *Nature* 299, 48–50.
- Buggisch, W., Wang, X., Alekseev, A.S., and Joachimski, M.M., 2011. Carboniferous-Permian carbon isotope stratigraphy of successions from China (Yangtze platform), USA (Kansas) and Russia (Moscow Basin and Urals). *Palaeogeography, Palaeoclimatology, Palaeoecology* 301, 18–38.
- Bush, R. and McInerney, F.A., 2013. Leaf wax n-alkane distributions in and across modern plants: Implications for paleoecology and chemotaxonomy. *Geochimica et Cosmochimica Acta* 117, 161–179.
- Carroll, A.R., Graham, S.A., and Hendrix, M.S., 1995. Late Paleozoic tectonic amalgamation of northwestern China: sedimentary record of the northern Tarim, northwestern Turpan, and southern Junggar basins. *Geological Society of America Bulletin* 107, 571–594.
- Cecil, C.B., 1990. Palaeoclimate controls on stratigraphic repetition of chemical and siliciclastic rocks. *Geology* 18, 533–536.
- Cecil, C.B., Dulong, F.T., West, R.R., Stamm, R., Wardlaw, B., and Edgar, N.T., 2003. Climate controls on the stratigraphy of a middle Pennsylvanian cyclothem in North America, in Cecil, C.B., Edgar, T.N., eds., *Climate Controls on Stratigraphy*. Society for Sedimentary Geology Special Publication 77, 151–180.

- Chen, Z., Wu, N., Zhang, D., Hu, J., Huang, H., Shen, G., Wu, G., Tang, H., and Hu, Y., 1985. Geologic map of Xinjiang Uygur Autonomous Region. Beijing, Geologic Publishing House, scale 1: 2,000,000, 1 sheet.
- Chumakov, N.M. and Zharkov, M.A., 2002. Climate during Permian–Triassic Biosphere Reorganizations, Article 1: Climate of the Early Permian. *Stratigraphy and Geological Correlation*, 10, 586–602.
- Clausing, A. and Boy, J.A., 2000. Lamination and primary production in fossil lakes: relationship to palaeoclimate in the Carboniferous–Permian transition. *Geological Society, London, Special Publications* 181, 5–16.
- Cohen, K.M., Finney, S.C., Gibbard, P.L., and Fan, J.X., 2018. The ICS International Chronostratigraphic Chart: Episodes 36, 199–204.
- Crowell, J.C., 1978. Gondwana glaciation, cyclothems, continental positioning, and climate change. *American Journal of Science* 278, 1345–1372.
- Craig, H., 1953. The geochemistry of the stable carbon isotopes. *Geochimica et Cosmochimica Acta* 3, 53–92.
- Craig, H., 1957. Isotopic standards for carbon and oxygen and correction factors for mass-spectrometric analysis of carbon dioxide. *Geochimica et Cosmochimica Acta*, 12, 133–149.
- Didyk, B.M., Simoneit, B.R.T., Brassell, S.C., and Eglinton, G., 1978. Organic geochemical indicators of palaeoenvironmental conditions of sedimentation. *Nature* 272, 216–222.
- Durand, B. and Nicaise, G., 1980. Procedures for kerogen isolation, in Durand, B., ed., *Kerogen-Insoluble Organic Matter from Sedimentary Rocks*: Editions Technip, Paris, p. 35–53.
- Eyles, C.H., Mory, A.J., and Eyles, N., 2003. Carboniferous–Permian facies and tectono-stratigraphic successions of the glacially influenced and rifted Carnarvon Basin, Western Australia. *Sedimentary Geology* 155, 63–86.
- Eyles, N., 1993. Earth's glacial record and its tectonic setting. *Earth-Science Reviews* 35, 1–248.
- Eyles, N., Mory, A.J., and Eyles, C.H., 2006. 50-million-year-long record of glacial to postglacial marine environments preserved in a Carboniferous–Lower Permian graben, Northern Perth Basin, Western Australia. *Journal of Sedimentary Research* 76, 618–632.
- Falkowski, P. et al., 2000. The global carbon cycle: A test of our knowledge of Earth as a system. *Sciences* 290, 291–296.

- Farquhar, G.D., Ehleringer, J.R., and Hubick, K.T., 1989. Carbon isotope discrimination and photosynthesis. *Annual Review of Plant Physiology and Plant Molecular Biology* 40, 503–537.
- Farquhar, G.D., O'Leary, M.H., and Berry, J.A., 1982. On the Relationship between carbon isotope discrimination and the intercellular carbon dioxide concentration in leaves. *Australian Journal of Plant Physiology* 9, 121–137.
- Ficken, K.J., Li, B., Swain, D.L., and Eglinton, G., 2000. An n-alkane proxy for the sedimentary input of submerged/floating freshwater aquatic macrophytes. *Organic Geochemistry* 31, 745–749.
- Fielding, C.R., Frank, T.D., Birgenheier, L.P., Rygel, M.C., Jones, A.T., and Roberts, J., 2008a. Stratigraphic imprint of the Late Paleozoic Ice Age in eastern Australia: a record of alternating glacial and nonglacial climate regime. *Journal of the Geological Society* 165, 129–140.
- Fielding, C.R., Frank, T.D., Birgenheier, L.P., Rygel, M.C., Jones, A.T., and Roberts, J., 2008b. Stratigraphic record and facies associations of the Late Paleozoic Ice Age in Eastern Australia (New South Wales and Queensland), in Fielding, C.R., Frank, T.D., Isbell, J.L., eds., *Resolving the Late Paleozoic Ice Age in Time and Space*. Geological Society of America Special Paper 441, 41–57.
- Fielding, C.R., Frank, T.D., and Isbell, J.L., 2008c. The late Paleozoic ice age – a review of current understanding and synthesis of global climate patterns, in Fielding, C.R., Frank, T.D., Isbell, J.L., eds., *Resolving the Late Paleozoic Ice Age in Time and Space*. Geological Society of America Special Paper 441, 343–354.
- Frakes, L.A. and Crowell, J.C., 1967. Facies and paleogeography of late Paleozoic Lafonian diamictite, Falkland Islands. *Geological Society of America Bulletin* 78, 37–58.
- Frank, T.D., Shultis, A.I., and Fielding, C.R., 2015. Acme and demise of the late Palaeozoic ice age: A view from the southeastern margin of Gondwana. *Palaeogeography, Palaeoclimatology, Palaeoecology* 418, 176–192.
- Fredericks, J.G., 2016. Provenance and depositional environments of fluvial-lacustrine deposits in a non-marine rift basin, Lower-Triassic Jiucayuan and Shaofanggou low order cycles Bogda Shan, NW China [Master thesis]. Missouri University of Science and Technology, 289 p.
- Freeman, K.H. and Hayes, J.M., 1992. Fractionation of carbon isotopes by phytoplankton and estimates of ancient CO₂ levels. *Global Biogeochemical Cycles* 6, 185–198.
- Ganeshram, R.S., Pedersen, T.F., Calvert, S.E., and François, R., 2002. Reduced nitrogen fixation in the glacial ocean inferred from changes in marine nitrogen and phosphorus inventories. *Nature* 415, 156–159.

- Gulbranson, E.L., Montañez, I.P., Schmitz, M.D., Limarino, C.O., Isbell, J.L., Marensi, S.A., and Crowley, L.J., 2010. High-precision U-Pb calibration of Carboniferous glaciation and climate history, NW Argentina. *Geological Society of America Bulletin* 122, 1480–98.
- Hayes, J.M., Popp, B.N., Takigiku, R., and Johnson, M.W., 1989. An isotopic study of biogeochemical relationships between carbonates and organic carbon in the Greenhorn Formation. *Geochimica et Cosmochimica Acta* 53, 2961–2972.
- Hayes, J.M., Strauss, H., and Kaufman A.J., 1999. The abundance of ^{13}C in marine organic matter and isotopic fractionation in the global biogeochemical cycle of carbon during the past 800 Ma. *Chemical Geology* 161, 103–125.
- Heckel, P.H., 1986. Sea-level curve for Pennsylvanian eustatic marine transgressive-regressive cycles along midcontinent outcrop belt, North America. *Geology* 14, 330–334.
- Heckel, P.H., 2008. Pennsylvanian cyclothems in Midcontinent North America as far-field effects of waxing and waning of Gondwana ice sheets, in Fielding, C.R., Frank, T.D., Isbell, J.L., eds., *Resolving the Late Paleozoic Ice Age in Time and Space*. Geological Society of America Special Paper 441, 275–289.
- Isbell, J.L., Biakov, A.S., Vedernikov, L.L., Davydov, V.I., Gulbranson, E.L., and Fedorchuk, N.D., 2016. Permian diamictites in northeastern Asia: Their significance concerning the bipolarity of the late Paleozoic ice age. *Earth-Science Reviews* 154, 279–300.
- Isbell, J.L., Henry, L.C., Gulbranson, E.L., Limarino, C.O., Fraiser, M.L., Koch, Z.J., Ciccio, P.L., and Dineen, A.A., 2012. Glacial paradoxes during the late Paleozoic ice age: evaluating the equilibrium line altitude as a control on glaciation. *Gondwana Research* 22, 1–19.
- Isbell, J.L., Koch, Z.J., Szablewski, G.M., and Lenaker, P.A., 2008. Permian glacial deposits in the Transantarctic Mountains, Antarctica, in Fielding, C.R., Frank, T.D., Isbell, J.L., eds., *Resolving the Late Paleozoic Ice Age in Time and Space*. Geological Society of America Special Paper 441, 59–70.
- Isbell, J.L., Lenaker, P.A., Askin, R.A., Miller, M.F., and Babcock, L.E., 2003a. Reevaluation of the timing and extent of late Paleozoic glaciation in Gondwana: role of the Transantarctic Mountains. *Geology* 31, 977–980.
- Isbell, J.L., Miller, M.F., Wolfe, K.L., and Lenaker, P.A., 2003b. Timing of late Paleozoic glaciation in Gondwana: was glaciation responsible for the development of northern hemisphere cyclothems? in Chan, M.A., Archer, A.W., eds., *Extreme Depositional Environments: Mega end Members in Geologic Time*. Geological Society of America Special Paper 370, 5–24.

- Kossovaya, O., Vachard, D., and Izart, A., 2013. Climatic impact on the reef biota in the Cisuralian and Guadalupian (Permian), East European Platform. Geological Society, London, Special Publications 376, 343–366.
- Lazar, R., Bohacs, K.M, Schieber, J., Macquaker, J., and Demko, T., eds., 2015. Mudstone Primer: Lithofacies variations, diagnostic criteria, and sedimentologic/stratigraphic implications at lamina to bedset scale. SEPM Concepts in Sedimentology and Paleontology 12, 205 pp.
- Le Heron, D.P., Tofaif, S., Vandyk, T., and Ali, D.O., 2017. A diamictite dichotomy: Glacial conveyor belts and olistostromes in the Neoproterozoic of Death Valley, California, USA. *Geology* 45, 31–34.
- Lopez-Gamundi, O.R. and Buatois, L.A., eds., 2010. Late Paleozoic Glacial Events and Postglacial Transgressions in Gondwana: Geological Society of America Special Publication 468, 207 p.
- Mazzullo, S.J., Boardman, D.R., Grossman, E.L., and Dimmick-Wells, K., 2007. Oxygen-carbon isotope stratigraphy of Upper Carboniferous to lower Permian marine deposits in Midcontinent U.S.A. (Kansas and ne Oklahoma): Implications for sea water chemistry and depositional cyclicity. *Carbonates and Evaporites* 22, 55–72.
- Meyers, P.A. and Ishiwatari, R., 1993. Lacustrine organic geochemistry-an overview of indicators of organic matter sources and diagenesis in lake sediments. *Organic Geochemistry* 20, 867–900.
- Meyers, P.A., 1997. Organic geochemical proxies of paleoceanographic, paleolimnologic, and paleoclimatic processes. *Organic Geochemistry* 27, 213–250.
- Michel, L.A., Tabor, N.J., Montañez, I.P., Schmitz, M.D., and Davydov, V.I., 2015. Chronostratigraphy and Paleoclimatology of the Lodève Basin, France: Evidence for a pan-tropical aridification event across the Carboniferous–Permian boundary. *Palaeogeography, Palaeoclimatology, Palaeoecology* 430, 118–131.
- Miller, K.B., McCahon, T.J., and West, R.R., 1996. Lower Permian (Wolfcampian) palaeosol bearing cycles of the U.S. Midcontinent: evidence of climatic cyclicity. *Journal of Sedimentary Research* 66, 71–84.
- Miller, K.B. and West, R.R., 1998. Identification of Sequence Boundaries within Cyclic Strata of the Lower Permian of Kansas, USA: Problems and Alternatives. *The Journal of Geology* 106, 119–132.
- Moldowan, J.M., Sundararaman, P., and Schoell, M., 1986. Sensitivity of biomarker properties to depositional environment and/or source input in the Lower Toarcian of SW-Germany. *Organic Geochemistry* 10, 915–26.

- Montañez, I.P., McElwain, J.C., Poulsen, C.J., White, J.D., DiMichele, W.A., Wilson, J.P., Griggs, G., and Hren, M.T., 2016. Climate, pCO₂ and terrestrial carbon cycle linkages during late Palaeozoic glacial–interglacial cycles. *Nature Geoscience* 9, 824–831.
- Montañez, I.P. and Poulsen, C.J., 2013. The late Paleozoic ice age: an evolving paradigm. *Annual Review of Earth & Planetary Sciences* 41, 1–28.
- Montañez, I.P., Tabor, N.J., Niemeier, D., DiMichele, W.A., Frank, T.D., Fielding, C.R., Isbell, J.L., Birgenheier, L.P., and Rygel, M.C., 2007. CO₂-forced climate instability and linkages to tropical vegetation during late Paleozoic deglaciation. *Science* 315, 87–91.
- Mory, A.J., Redfern, J., and Martin, J.R., 2008. A review of Permian-Carboniferous glacial deposits in Western Australia, in Fielding, C.R., Frank, T.D., Isbell, J.L., eds., *Resolving the Late Paleozoic Ice Age in Time and Space*. Geological Society of America Special Paper 441, 29–40.
- Obrist-Farner, J. and Yang, W., 2016. Implications of loess and fluvial deposits on paleoclimatic conditions during an icehouse–hothouse transition, Capitanian upper Quanzijie low-order cycle, Bogda Mountains, NW China. *Palaeogeography, Palaeoclimatology, Palaeoecology* 441, 959–981.
- O'Leary, M.H., 1981. Carbon isotope fractionation in plants. *Phytochemistry* 20, 553–567.
- O'Leary, M.H., 1988. Carbon isotopes in photosynthesis. *Bioscience* 38, 328–336.
- Ourisson, G. and Albrecht, P., 1992. Hopanoids. 1. Geohopanoids: The Most Abundant Natural Products on Earth. *Accounts of Chemical Research* 25, 398–402.
- Parrish, J.T., 1993. Climate of the supercontinent Pangaea. *Journal of Geology* 101, 215–233.
- Peters, K.E. and Moldowan, J.M., 1991. Effects of source, thermal maturity, and biodegradation on the distribution and isomerization of homohopanes in petroleum: *Organic Geochemistry* 17, 47–61.
- Peters, K.E., Walter, M.M., and Moldowan, J.M., 2005. *The Biomarker Guide, Volume 2, Biomarkers and Isotopes in Petroleum Exploration and Earth History*: Cambridge University Press, UK, 489 p.
- Peterson, L.C., Haug, G.H., Hughen, K.A., Röhl, U., 2000. Rapid changes in the hydrologic cycle of the tropical Atlantic during the Last Glacial. *Science* 290, 1947–1951.

- Peyser, C.E., and Poulsen, C.J., 2008. Controls on Permo-Carboniferous precipitation over tropical Pangaea: A GCM sensitivity study. *Palaeogeography, Palaeoclimatology, Palaeoecology* 268, 181–192.
- Poulsen, C.J., Pollard, D., Montañez, I.P., and Rowley, D., 2007. Late Paleozoic tropical climate response to Gondwanan deglaciation. *Geology* 35, 771–774.
- Prahl, F.G., Bennett, J.T., and Carpenter, R., 1980. The early diagenesis of aliphatic hydrocarbons and organic matter in sedimentary particulates from Dabob Bay, Washington. *Geochimica et Cosmochimica Acta* 44, 1967–1976.
- Rieley, G., Collier, R.J., Jones, D.M., and Eglinton, G., 1991. The biogeochemistry of Ellesmere Lake, U.K. – I: Source correlation of leaf wax inputs to the sedimentary record. *Organic Chemistry* 17, 901–912.
- Rohmer, M., Bouvier-Nave, P., and Ourisson, G. 1984. Distribution of hopanoid triterpenes in prokaryotes. *Journal of General Microbiology* 130, 1137–1150.
- Roscher, M. and Schneider, J.W., 2006. Permo-Carboniferous climate: Early Pennsylvanian to Late Permian climate development of central Europe in a regional and global context. *Geological Society, London, Special Publications* 265, 95–136.
- Rullkötter, J. and Marzi, R., 1988. Natural and artificial maturation of biological markers in a Toarcian shale from northern Germany: *Advances in Organic Geochemistry* 13, 639–645.
- Rygel, M.C., Fielding, C.R., Frank, T.D., and Birgenheier, L.P., 2008. The magnitude of late Paleozoic glacioeustatic fluctuations: a synthesis. *Journal of Sedimentary Research* 78, 500–511.
- Saltzman, M.R. and Thomas, E., 2012. Carbon Isotope Stratigraphy, in Gradstein, F.M., Ogg, J.G., Schmitz, M.D., Ogg, G.M., eds., *The Geological Time Scale 2012*: Oxford Press, UK, 1139 p.
- Schneider, J.W., Körner, F., Roscher, M., Kroner, U., 2006. Permian climate development in the northern peri-Tethys area – The Lodève basin, French Massif Central, compared in a European and global context. *Palaeogeography, Palaeoclimatology, Palaeoecology* 240, 161–183.
- Scotese, C.R., 2014. *Atlas of Permo-Carboniferous Paleogeographic Maps (Mollweide Projection)*, Maps 53–64: PALEOMAP PaleoAtlas for ArcGIS The Late Paleozoic, v. 4. PALEOMAP Project, Evanston, IL.
- Seifert, W.K. and Moldowan, J.M., 1978. Applications of steranes, terpanes and monoaromatics to the maturation, migration and source of crude oils. *Geochimica et Cosmochimica Acta* 42, 77–95.

- Seifert, W.K. and Moldowan, J.M., 1986. Use of biological markers in petroleum exploration, in Johns, R.B. ed., *Methods in Geochemistry and Geophysics* 24, 261–290.
- Sepúlveda, J., Wendler, J., Leiderb, A., Kuss, H.J., Summons, R.E., and Hinrichs, K.U., 2009. Molecular isotopic evidence of environmental and ecological changes across the Cenomanian–Turonian boundary in the Levant Platform of central Jordan. *Organic Geochemistry* 40, 553–56.
- Siegenthaler, U. and Sarmiento J.L., 1993. Atmospheric carbon dioxide and the ocean. *Nature* 365, 119–125.
- Sinninghe Damsté, J.S., Kenig, F., Koopmans, M.P., Köster, J., Schouten, S., Hayes, J.M., and de Leeuw, J.W., 1995. Evidence for gammacerane as an indicator of water-column stratification. *Geochimica et Cosmochimica Acta* 59, 1895–900.
- Smith, B.N. and Epstein, S., 1971. Two Categories of $^{13}\text{C}/^{12}\text{C}$ Ratios for Higher Plants. *Plant Physiology* 47, 380–384.
- Stemmerick, L., 2008. Influence of late Paleozoic Gondwana glaciations on the depositional evolution of the northern Pangean shelf, North Greenland, Svalbard, and the Barents Sea, in Fielding, C.R., Frank, T.D., Isbell, J.L., eds., *Resolving the Late Paleozoic Ice Age in Time and Space*. Geological Society of America Special Paper 441, 59–70.
- Stollhofen, H., Werner, M., Stanistreet, I.G., and Armstrong, R.A., 2008. Single-zircon U-Pb dating of Carboniferous-Permian tuffs, Namibia, and the intercontinental deglaciation cycle framework, in Fielding, C.R., Frank, T.D., Isbell, J.L., eds., *Resolving the Late Paleozoic Ice Age in Time and Space*. Geological Society of America Special Paper 441, 83–96.
- Tabor, N.J. and Montañez, I.P., 2002. Shifts in late Palaeozoic atmospheric circulation over western equatorial Pangaea: insights from pedogenic mineral $\delta^{18}\text{O}$ compositions. *Geology* 30, 1127–1130.
- Tabor, N.J., Montañez, I.P., Scotese, C.R., Poulsen, C.J., and Mack, G.H., 2008. Paleosol archives of environmental and climatic history in paleotropical western Pangea during the latest Pennsylvanian through Early Permian, in Fielding, C.R., Frank, T.D., Isbell, J.L., eds., *Resolving the Late Paleozoic Ice Age in Time and Space*. Geological Society of America Special Paper 441, 291–303.
- Tyson, R.V., 1995. *Sedimentary Organic Matter*, first ed. Chapman and Hall, London, 462 p.
- Vesely, F.F., Rodrigues, M.C.N.L., da Rosa, E.L.M., Amato, J.A., Trzaskos, B., Isbell, J.L., and Fedorchuk, N.D., 2018. Recurrent emplacement of non-glacial diamictite during the late Paleozoic ice age. *Geology* 46, 615–618.

- Volkman, J.K., 1986. A review of sterol markers for marine and terrigenous organic matter. *Organic Geochemistry* 9, 83–99.
- Volkman, J.K., 2003. Sterols in microorganisms. *Applied Microbiology and Biotechnology* 60, 495–506.
- Waiser, M.J. and Robarts, R., 2009. Saline inland waters: Lakes - formation, diversity, distribution, in Likens, G.E., ed., *Encyclopaedia of inland waters II*, Elsevier, p. 634–644.
- Waterhouse, J.B. and Shi, G.R., 2010. Evolution of a cold climate. *Palaeogeography, Palaeoclimatology, Palaeoecology* 298, 17–30.
- Yang, J.H., Cawood, P.A., Du, Y.S., Feng, B., and Yan, J.X., 2014. Global continental weathering trends across the Early Permian glacial to postglacial transition: Correlating high- and low-paleolatitude sedimentary records. *Geology* 42, 835–838.
- Yang, W., 2008. Depositional Systems Analysis within a Seismic Sequence Stratigraphic Framework, Turpan-Hami Basin, NW China. Tu-Ha Oil Company Internal Report, PetroChina, 49 p.
- Yang, W., Feng, Q., Liu, Y.Q., Lin, J.Y., and Guan, W., 2009. Wither Nonmarine Sequence Stratigraphy? Sequence Stratigraphic Correlation of Lower Permian Fluvial-Lacustrine Deposits in a Half Graben, Bogda Mountains, NW China. AAPG Annual Convention and Exhibition, Abstract Volume, Denver, p. 352.
- Yang, W., Feng, Q., Liu, Y., Tabor, N., Miggins, D., Crowley, J.L., Lin, J., and Thomas, S., 2010. Depositional environments and cyclo- and chronostratigraphy of uppermost Carboniferous-Lower Triassic fluvial-lacustrine deposits, southern Bogda Mountains, NW China - a terrestrial paleoclimatic record of mid-latitude NE Pangea. *Global and Planetary Change* 73, 15–113.
- Yang, W., Liu, Y., Feng, Q., Lin, J., Zhou, D., and Wang, D., 2007. Sedimentary evidence of Early-Late Permian mid-latitude continental climate variability, southern Bogda Mountains, NW China. *Palaeogeography, Palaeoclimatology, Palaeoecology* 252, 239–258.
- Zolitschka, B., Francus, P., Ojala, A.E.K., and Schimmelmann, A., 2015. Varves in lake sediments – a review. *Quaternary Science Reviews* 117, 1–41.

SECTION

2. CONCLUSIONS

The results of this study show that physical and chemical conditions of fluvial-lacustrine deposits in southern Bogda Mountains, NE Pangea responses of Earth Systems to environmental and climatic perturbations in cm-m-scale high-order cycles (HCs: kys), low-order cycles (LCs: 1–10 Myr), and critical events of late Paleozoic ice age (LPIA: 320–260 Myr ago).

A centimeter-scale investigation of mixed carbonate and siliciclastic lacustrine deposits in LCG HCs shows that litho- and organo-facies are one-to-one correlated. The correlation between the four litho- and organo-facies in the meter-scale HCs suggests litho- and organo-facies are genetically linked and may have been controlled by lake shoreline transgression and regression during relatively short period of time, which were likely caused by lake level rise and fall, respectively. The results demonstrate that a holistic approach using lithologic and organic geochemical data is useful in delineating cyclic changes of depositional environments at a cm-m scale and highly variable depositional sequence of a lake depositional system, and therefore can be used to understand short-term sedimentary processes in other lacustrine systems.

Climatic changes of southeastern Kazakhstan mid-latitude northeast Pangea may have been under control of migration of the ITCZ, constrained by dynamic glacial cyclicity in Southern Hemisphere during the late Paleozoic. Humidity and seasonality in southern Bogda corresponded to late Paleozoic retreat of glacial P1 over most of Gondwana in early Sakmarian. Enhanced aridity and seasonality in southern Bogda were

confined to interglacial stage between P1 and P2 during mid-late Sakmarian. Increased humidity and reduced seasonality in southern Bogda coincided with glacial stage of P2 in Artinskian–early Kungurian. The coincidence of climatic changes in mid-latitude northeast Pangea and Gondwanan glacial–interglacial in mid Sakmarian–early Kungurian provides clues that glaciation may have exerted a substantial control on climatic changes in mid-latitude Northern Hemisphere. Humid and stable climate of southeastern Kazakhstan may have been caused by a low pressure zone of rainfalls over mid-latitude northeast Pangea and a stable ITCZ over equatorial Pangea during glacial. Arid and seasonal climate over southeastern Kazakhstan may have been induced by a dominance of high pressure zone without rainfalls and seasonal migration of the ITCZ between mid-latitude of North and South Hemisphere during interglacial. Notably, this study also shows that common lithotypes and biomarkers, including laminated shales, varves, dropstones, gammacerane index, and $T_s/(T_s+T_m)$ ratios can be used to interpret climatic changes over southeastern Kazakhstan mid-latitude northeast Pangea, and thus can be used as climate-sensitive proxies for reconstruction of paleoclimates in other continental stratigraphic successions. This will contribute to better understanding of the linkage between glacial–interglacial dynamics in South Hemisphere and climatic responses in paleo-tropics and North Hemisphere.

BIBLIOGRAPHY

- Allen, J.P., Fielding, C.R., Gibling, M.R., and Rygel, M.C., 2011. Fluvial response to paleo-equatorial climate fluctuations during the late Paleozoic ice age. *Geological Society of America Bulletin* 123, 1524–1538.
- Bohacs, K.M., Carroll, A.R., Neal, J.E., and Mankiewicz, P.J., 2000. Lake basin type, source potential, and hydrocarbon character: An integrated sequence-stratigraphic-geochemical framework. In: Gierlowski-Kordesch, E.H. and Kelts, K.R. (Eds.), *Lake Basins through Space and Time*. American Association of Petroleum Geologists *Studies in Geology* 46, 3–34.
- Carroll, A.R. and Bohacs, K.M., 1999. Stratigraphic classification of ancient lakes: balancing tectonic and climatic controls. *Geology* 27, 99–102.
- Carroll, A.R., 1998. Upper Permian lacustrine organic facies evolution, southern Junggar Basin, NW China. *Organic Geochemistry* 28, 649–667.
- Cecil, C.B., 1990. Palaeoclimate controls on stratigraphic repetition of chemical and siliciclastic rocks. *Geology* 18, 533–536.
- Curiale, J.A., Cole, R.D., and Witmer, R.J., 1992. Application of organic geochemistry to sequence stratigraphic analysis: Four Corners Platform Area, New Mexico, U.S.A. *Advances in Organic Geochemistry* 19, 53–75.
- Fielding, C.R., Frank, T.D., Birgenheier, L.P., Rygel, M.C., Jones, A.T., and Roberts, J., 2008. Stratigraphic record and facies associations of the Late Paleozoic Ice Age in Eastern Australia (New South Wales and Queensland), in Fielding, C.R., Frank, T.D., Isbell, J.L., eds., *Resolving the Late Paleozoic Ice Age in Time and Space*. Geological Society of America Special Paper 441, 41–57.
- Horsfield, B., Curry, D.J., Bohacs, K., Littke, R., Rullkötter, J., Schenk, H.J., Radke, M., Schaefer, R.G., Carroll, A.R., Isaksen, G., and Witte, E.G., 1994. Organic geochemistry of freshwater and alkaline lacustrine sediments in the Green River Formation of the Washakie Basin, Wyoming, USA. *Organic Geochemistry* 22, 415–440.
- Isbell, J.L., Miller, M.F., Wolfe, K.L., and Lenaker, P.A., 2003. Timing of late Paleozoic glaciation in Gondwana: was glaciation responsible for the development of northern hemisphere cyclothems? in Chan, M.A., Archer, A.W., eds., *Extreme Depositional Environments: Mega end Members in Geologic Time*. Geological Society of America Special Paper 370, 5–24.
- Miller, K.B., McCahon, T.J., and West, R.R., 1996. Lower Permian (Wolfcampian) palaeosol bearing cycles of the U.S. Midcontinent: evidence of climatic cyclicity. *Journal of Sedimentary Research* 66, 71–84.

- Montañez, I.P., McElwain, J.C., Poulsen, C.J., White, J.D., DiMichele, W.A., Wilson, J.P., Griggs, G., and Hren, M.T., 2016. Climate, pCO₂ and terrestrial carbon cycle linkages during late Palaeozoic glacial–interglacial cycles. *Nature Geoscience* 9, 824–831.
- Montañez, I.P. and Poulsen, C.J., 2013. The late Paleozoic ice age: an evolving paradigm. *Annual Review of Earth & Planetary Sciences* 41, 1–28.
- Montañez, I.P., Tabor, N.J., Niemeier, D., DiMichele, W.A., Frank, T.D., Fielding, C.R., Isbell, J.L., Birgenheier, L.P., and Rygel, M.C., 2007. CO₂-forced climate instability and linkages to tropical vegetation during late Paleozoic deglaciation. *Science* 315, 87–91.
- Parrish, J.T., 1993. Climate of the supercontinent Pangaea. *Journal of Geology* 101, 215–233.
- Poulsen, C.J., Pollard, D., Montañez, I.P., and Rowley, D., 2007. Late Paleozoic tropical climate response to Gondwanan deglaciation. *Geology* 35, 771–774.
- Slatt, R.M. and Rodriguez, N.D., 2012. Comparative sequence stratigraphy and organic geochemistry of gas shale: Commonality or coincidence? *Journal of Natural Gas Science and Engineering* 8, 68–84.
- Tabor, N.J. and Poulsen, C.J., 2008. Palaeoclimate across the Late Pennsylvanian–Early Permian tropical palaeolatitudes: A review of climate indicators, their distribution, and relation to palaeophysiographic climate factors. *Palaeogeography, Palaeoclimatology, Palaeoecology* 268, 293–310.
- Tyson, R.V., 1995. *Sedimentary Organic Matter*, first ed. Chapman and Hall, London.

VITA

Xin Zhan received his Bachelor degree of Engineering in Resources Exploration in China University of Geosciences, Wuhan, China in July of 2014. Then he joined Dr. Wan Yang's research group in August of 2014 as a Master student in Geology and Geophysics program at Missouri University of Science and Technology, Rolla, Missouri. He then transfer to a Ph.D. student in August of 2016 and worked as a teaching assistant in Geology and Geophysics program at Missouri University of Science and Technology. In December of 2019, he received his Doctor of Philosophy degree in Geology and Geophysics from Missouri University of Science and Technology.